INSIDE-PIPE HEAT TRANSFER COEFFICIENT CHARACTERISATION OF A ONE THIRD HEIGHT SCALE MODEL OF A NATURAL CIRCULATION LOOP SUITABLE FOR A REACTOR CAVITY COOLING SYSTEM OF THE PEBBLE BED MODULAR REACTOR

by
Ilse Sittmann

Thesis presented in partial fulfilment of the requirements for the degree Master of Science in Engineering at the University of Stellenbosch

Supervisor: Mr Robert Dobson
Faculty of Engineering
Department of Mechanical and Mechatronic Engineering

March 2011

DECLARATION

By submitting this thesis electronically, I declare that the entirety of the work contained therein is my own, original work, that I am the owner of the copyright thereof (unless to the extent explicitly otherwise stated) and that I have not previously in its entirety or in part submitted it for obtaining any qualification.

Signature:  Date: .....03-02-2011.....

ABSTRACT

The feasibility of a closed loop thermosyphon for the Reactor Cavity Cooling System of the Pebble Bed Modular Reactor has been the subject of many research projects. Difficulties identified by previous studies include the hypothetical inaccuracies of heat transfer coefficient correlations available in literature. The aim of the research presented here is to develop inside-pipe heat transfer correlations that are specific to the current design of the RCCS.

In order to achieve this, a literature review is performed which identifies reactors which employ closed loop thermosyphons and natural circulation. The literature review also explains the general one-dimensional two-fluid conservation equations that form the basis for numerical modelling of natural circulation loops. The literature review lastly discusses available heat transfer coefficient correlations with the aim of identifying over which ranges and under which circumstances these correlations are considered accurate. The review includes correlations commonly used in natural circulation modelling in the nuclear industry in aims of identifying correlations applicable to the modelling of the proposed RCCS.

One of the objectives of this project is to design and build a one-third-height-scale model of the RCCS. Shortcomings of previous experimental models were assessed and, as far as possible, compensated for in the design of the model. Copper piping is used, eliminating material and surface property uncertainties. Several sight glasses are incorporated in the model, allowing for the visual identification of two-phase flow regimes. An orifice plate is used allowing for bi-directional flow measurement. The orifice plate, thermocouples and pipe-in-pipe heat exchangers are calibrated in-situ to minimize experimental error and aid repeatability.

Twelve experiments are performed with data logging occurring every ten seconds. The results presented here are limited to selected single and two-phase flow operating mode results. Error analyses and repeatability of experimental measurements for single and two-phase operating modes as well as cooling water mass flow rates are performed, to show repeatability of experimental results. These results are used to mathematically determine the experimental inside-pipe heat transfer coefficients for both the evaporator and condenser sections. Trends in the heat transfer coefficient profiles are identified and the general behaviour of the profiles is thoroughly explained.

The RCCS is modelled as a one-dimensional system. Correlations for the friction factor, heat transfer coefficient, void fraction and two-phase frictional multiplier are identified. The theoretical heat transfer coefficients are calculated using the mathematical model and correlations identified in the literature review. Fluid parameters are evaluated using experimentally determined temperatures and mass flow rates. The resulting heat transfer coefficient profiles are compared to

experimentally determined profiles, to confirm the hypothesis that existing correlations do not accurately predict the inside-pipe heat transfer coefficients.

The experimentally determined coefficients are correlated to 99% confidence intervals. These generated correlations, along with identified and established two-phase heat transfer coefficient correlations, are used in a mathematical model to generate theoretical coefficient profiles. These are compared to the experimentally determined coefficients to show prediction accuracy.

OPSOMMING

Die haalbaarheid van ‘n natuurlike sirkulasie geslote lus vir die Reaktor Holte Verkoeling Stelsel (RHVS) van die Korrelbed Modulêre Kern-Reaktor (KMKR) is die onderwerp van talle navorsings projekte. Probleme geïdentifiseer in vorige studies sluit in die hipotetiese onakkuraatheid van hitte-oordrag koëffisiënt korrelasies beskikbaar in literatuur. Die doel van die navorsing aangebied is om binne-pyp hitte-oordrag koëffisiënt korrelasies te ontwikkel spesifiek vir die huidige ontwerp van die RHVS.

Ten einde dit te bereik, word ‘n literatuurstudie uitgevoer wat kern-reaktors identifiseer wat gebruik maak van natuurlike sirkulasie lusse. Die literatuurstudie verduidelik ook die algemene een-dimensionele twee-vloeistof behoud vergelykings wat die basis vorm vir numeriese modellering van natuurlike sirkulasie lusse. Die literatuurstudie bespreek laastens beskikbare hitte-oordrag koëffisiënt korrelasies met die doel om te identifiseer vir welke massavloei tempo waardes en onder watter omstandighede hierdie korrelasies as korrek beskou is. Die ontleding sluit korrelasies in wat algemeen gebruik word in die modellering van natuurlike sirkulasie in die kern industrie met die hoop om korrelasies vir gebruik in die modellering van die voorgestelde RHVS te identifiseer.

Een van die doelwitte van die projek is om ‘n een-derde-hoogte-skaal model van die RHVS te ontwerp en te bou. Tekortkominge van vorige eksperimentele modelle is geidentifiseer en, so ver as moonlik, voor vergoed in die ontwerp van die model. Koper pype word gebruik wat die onsekerhede van materiaal en opperkvlak eindomme voorkom. Verkseie deursigtige polikarbonaat segmente is ingesluit wat visuele identifikasie van twee-fase vloei regimes toelaat. ‘n Opening plaat word gebruik om voorwaartse en terugwaartse vloeimeting toe te laat. Die opening plaat, termokoppels en hitte uitruilers is gekalibreer in plek om eksperimentele foute te verminder en om herhaalbaarheid te verseker.

Twaalf eksperimente word uitgevoer en data word elke tien sekondes aangeteken. Die resultate wat hier aangebied word, is beperk tot geselekteerde enkel- en twee-fase vloei meganismes van werking. Fout ontleding en herhaalbaarheid van eksperimentele metings, om die herhaalbaarheid van eksperimentele resultate te toon. Hierdie is gebruik om wiskundig te bepaal wat die eksperimentele binne-pyp hitte-oordrag koëffisiënte is vir beide die verdamper en kondenseerder afdelings. Tendense in die hitte-oordrag koëffisiënt profiele word geïdentifiseer en die algemene gedrag van die profiles is deeglik verduidelik.

Die RHVS is gemodelleer as 'n een-dimensionele stelsel. Korrelasies vir die wrywing faktor, hitte-oordrag koëffisiënte, leegte-breuk en twee-fase wrywings vermenigvuldiger word geïdentifiseer. Die teoretiese hitte-oordrag koëffisiënte word bereken deur middle van die wiskundige model en korrelasies wat in literatuur geidentifiseer is. Vloeistof parameters is geëvalueer met eksperimenteel bepaalde temperature en massa-vloei tempos. Die gevolglike hitte-oordrag

koëffisiënt profiles is vergelyk met eksperimentele profiele om die hipotese dat die bestaande korrelasies nie die binne-pyp hitte-oordrag koëffisiënte akkuraat voorspel nie, te bevestig.

Die eksperimenteel bepaalde koëffisiënte is gekorreleer en die gegenereerde korrelasies, saam met geïdentifiseerde twee-fase hitte-oordrag koëffisiënt korrelasies, word gebruik in 'n wiskundige model om teoretiese koëffisiënt profiele te genereer. Dit word dan vergelyk met die eksperimenteel bepaalde hitte-oordrag koëffisiënte om die akkuraatheid van voorspelling te toon.

Tekortkominge in die teoretiese en eksperimentele model word geïdentifiseer en aanbevelings gemaak om hulle aan te spreek in die toekoms

ACKNOWLEDGEMENTS

The author would like to thank the following people:

Mr Cobus Zietsman, for his advice and technical expertise during the design and experimental phase of this research.

Mr Ferdi Zietsman, for his advice and assistance on manufacturing the experimental model.

The employees of the Mechanical Engineering Department workshop, for the manufacture of all the components. Specific thanks go to Mr Julian Stanfliet and Mr Calvin Harmse for their assistance in assembly, manufacture and experimentation.

Mr Eric Ward, for the manufacture and constant repair of the glass pipes for the condenser section.

Mr Ockert Kritzinger, for his advice and assistance in the design of the support frame and of the experimental loop as well as the cooling water supply line and being available for incessant questions about manufacture, suppliers, experimentation and theoretical modelling techniques.

Miss Leanne Haworth, for her assistance and advice during experimentation and constant support.

PBMR(Pty) Ltd and Necsa, for financing this research.

Mr Robert Dobson, the supervisor of this thesis, for his advice, expertise, support and incredible patience during the course of this research.

DEDICATION

This thesis is dedicated to my family for their unconditional support and understanding.

CONTENTS

LIST OF FIGURES

LIST OF TABLES

NOMENCLATURE

A	area, m^2
c	specific heat, J/kg K
D	pipe diameter, m
F	force, N
F	two phase heat transfer coefficient multiplier
f	Darcy friction factor
G	mass flux, kg/m^2 s
g	gravitational constant, m/s^2
Gr	Grashof number
h	heat transfer coefficient, W/m^2 K
h	enthalpy, J/kg
h	spatial step size, m
j	volumetric flux density, m/s
k	thermal conductivity, W/m K
k	loss coefficient
k	time step size, s
k_s	equivalent sand-grain roughness, m
K	minor loss coefficient
L	length, m
M	molecular weight, kg/kmol
M	control volume mass, kg
$\dot{m}$	mass flow rate, kg/s
Nu	Nusselt number
$\vec{n}$	outward normal vector
$\wp$	perimeter, m
P	Pressure, Pa
Pr	Prandtl number
q	thermal energy, J
$q"$	heat flux, W/m^2
Q	interfacial heat transfer rate, W
R	thermal resistance, K/W
Ra	Rayleigh number
Re	Reynolds number
S	suppression factor
S	slip ratio
$\dot{S}$	heat transfer rate, W
T	temperature, K or °C
t	time, s
U	total internal energy, J
U	overall heat transfer coefficient, W/m^2 K
u	specific internal energy, J/kg
u	phase stagnation energy, J/kg
v	phase velocity, m/s
V	volume m^3

X Martinelli parameter
x thermodynamic quality
Z height, m

Greek letters
α vapour void fraction
β thermal expansion coefficient, K^{-1}
Γ mass generation rate per unit volume, $kg/m^3/s$
θ angle, rad
λ thermal conductivity
μ dynamic viscosity, kg/m s
ξ truncation error
ρ density, kg/m^3
σ surface tension, N/m
τ shear stress, N/m^2
φ fluid phase parameter
φ^2 two phase multiplier
υ kinematic viscosity, kg/ms
$\{\psi\}$ fluid phase parameter

Superscript
$^\circ$ stagnation

Subscript
a air
b bulk
C cold
c convection
cw cooling water
D diameter
e evaporator
et expansion tank
f saturated liquid
F frictional
FC forced convection
fg latent
g generated, gas
G gravitational
H hot
i inside
k denotes phase
k conduction
l liquid phase
l laminar
lm logarithmic mean
lo liquid only

m	mixture, minor flow losses
M	momentum changes
NB	nucleate boiling
o	outside
p	constant pressure
pool	pool boiling
r	reduced
r	relative
s	surface
sat	saturated
sk	interfacial
t	turbulent
tank	expansion tank
tt	turbulent-turbulent
v	constant volume
v	gaseous phase
vj	drift
w	water, wall
x	cross-sectional

Overscore

$\vec{\ }$	vector
$\bar{\ }$	average

1 INTRODUCTION

1.1 Passive Safety

The International Atomic Energy Agency (IAEA) defines a passive system as "*Either a system which is composed entirely of passive components and structures or a system which uses active components in a very limited way to initiate subsequent passive operation*" (International Atomic Energy Agency, 1991). This has allowed for passive safety systems to be divided into three broad categories.

Category A is characterised by no "intelligence" input. In other words, no signal inputs, parametric changes or operator decision inputs are necessary to initiate action. In addition, a Category A passive safety system cannot incorporate external power sources or forces, moving mechanical parts or moving working fluids. Category B differs as it allows for moving working fluids. The motion of the fluid can only be caused by a change in thermal-hydraulic conditions due to activation of the safety system (as with natural circulation). Category C passive safety systems may contain moving mechanical parts, regardless of whether a working fluid is also present. This category includes all safety systems that require check or relief valves, trip mechanisms, rupture disks or any other mechanical parts required to activate the safety system (International Atomic Energy Agency, 1991).

Passive safety systems and components are incorporated into nuclear reactors to improve reliability and simplify safety systems. The IAEA notes that passive safety systems should be used wherever possible (International Atomic Energy Agency, 1996), keeping in mind that passivity should: reduce the number of components (reducing safety actions); eliminate short-term operator input during an accident; minimise dependence on external power sources, moving mechanical parts and control systems, and, finally reduce lifetime-associated costs of the reactor (International Atomic Energy Agency, 2000).

1.2 Background

A closed loop thermosyphon is a reliable method of transferring thermal energy from a heat source to a heat sink, via thermally induced density gradients, resulting in natural circulation. This allows for energy transfer over relatively long distances without the use of any mechanical parts (Dube et. al., 2004). Flow is driven by hydrostatic pressure difference as a result of thermally generated density gradients. One side of the loop is heated and the other cooled, thus the average density of the fluid in the heated section is less than that of the cooled section. Such thermosyphon loops find applications in the nuclear industry as cooling systems for the reactor core and surrounding structures (Greif, 1988).

The Pebble Bed Modular Reactor (PBMR) concept evolved from a German high temperature, helium-cooled reactor design with ceramic spherical fuel elements

know as INTERATOM HTR-MODUL. The main advantage of this design is that the reactor can be continuously refuelled during operation. The most noted safety feature of this design is that the silicon carbide coating of the fuel particle within the pebbles provides the first level of containment, as it keeps the fission products within itself. These design features facilitate the removal of parasitic heat through the Reactor Cavity Cooling System (RCCS).

The RCCS's primary function is to maintain the cavity temperature within a required range. This provides protection to the concrete structures surrounding the reactor and also, during loss of coolant accident operating conditions, transports parasitic heat from the reactor to the environment. (van Staden, 2001)

The current RCCS for the PBMR, as proposed by Dobson (2006), is given in Figure 1-1. The RCCS, in this concept, is represented by a number of axially symmetrical elements: the reactor core, reactor pressure vessel, air in the cavity between the reactor vessel and the concrete structure, the concrete structure, a heat sink situated outside the concrete structure, and a number of closed loop thermosyphons with the one vertical leg in the hot air cavity and the other leg in the heat sink. These loops are spaced around the periphery of the reactor cavity at a pitch angle θ. Vertical fins are attached to the length of the pipe in the cavity in order to shield the concrete structure from radiation and convection (from the reactor vessel through the gap between the pipes) and to conduct the heat to the pipes (Dobson & Ruppersburg, 2006).

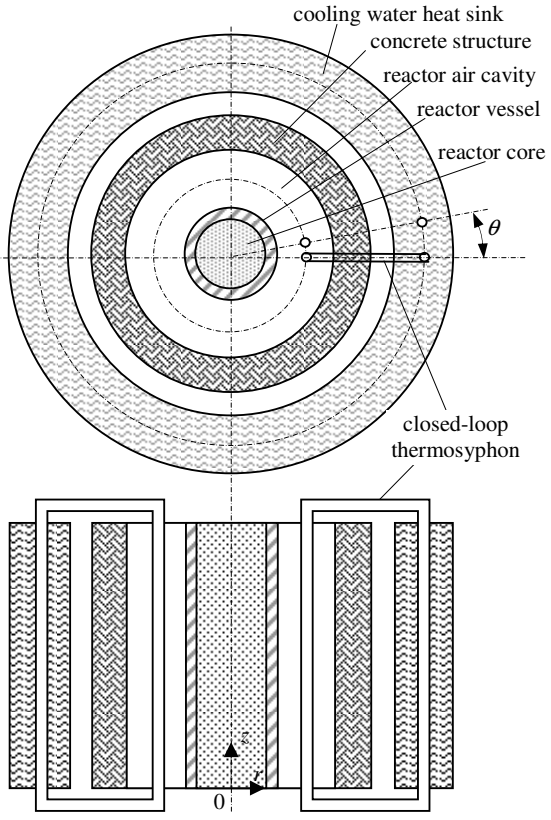

Figure 1-1: RCCS concept (Dobson, 2006)

1.3 Objectives

The following objectives were identified at the outset of this project:

1) Perform a literature survey
    a) Research natural circulation simulation theory with specific reference to the nuclear industry. Identify applicable numerical solution techniques used to model thermosyphon loops
    b) Research heat transfer coefficient correlations employed in natural circulation simulation.
    c) Identify and research comparative nuclear technology with specific reference to passive safety systems for core decay heat removal and containment cooling of generation IV reactor designs.
2) Design and build a one-third-height-scale model of the RCCS. Make use of copper piping for its high thermal conductivity and the thorough understanding of its heat transfer characteristics. Also ensure several sight glasses are placed at critical positions in the loop so that flow regime patterns can be visually identified.
3) Design and conduct experiments on the physical model while operating in single phase, single and two-phase, and heat pipe operating modes. These experiments must allow for the heat input into the system to simulate normal as well as loss of coolant accident operating conditions of a PBMR.
4) Write a computer program, incorporating methods and correlations identified in the literature survey, which will simulate the working of the thermosyphon as well as heat sources and sinks.
5) Compare the experimental and numerical results. Critically evaluate the data and draw conclusions to its validity with the aid of published results as well as a thorough understanding of the underlying physics. Also address the suitability of the theoretical model as a simulation of the full scale RCCS.

2 LITERATURE STUDY

This study will familiarise the reader with certain "innovative" Generation IV nuclear reactor designs which employ passive safety systems for core decay heat removal and containment cooling systems. This will place into context the RCCS of the PBMR design and show the importance of the development of an accurate theoretical model that describes two-phase natural circulation in nuclear applications. The focus will then shift to simulation methods for natural circulation currently employed in industry, with specific reference to the heat transfer coefficient correlations available.

2.1 Reactor Designs

The Generation III+ and Generation IV nuclear reactor concepts currently under development all incorporate passive safety systems, whether it be as a primary coolant, decay heat removal, containment cooling, loss of coolant accident or emergency core cooling system. Extensive literature is available on each of the reactors mentioned in this study therefore their design and operating characteristics will not be discussed in detail.

2.1.1 AP 1000

The Westinghouse AP1000 is a two-loop pressurised light water reactor (PWR) designed to yield 1154 MWe. The AP1000 is the first Generation III+ reactor to receive *Design Certification* from the United States Nuclear Regulatory Commission (USNRC) (Westinghouse Electrical Company, 2008).

The reactor core is designed for both uranium oxide (UO_2) and mixed oxide (MOX) fuel assemblies and utilises 69 control rods in order to control reactivity. The basic functioning of the AP1000 (and all PWRs in general) is as follows. Nuclear fission in the reactor fuel generates heat which is transferred to the primary coolant through forced convection. The hot primary fluid is then passed through a heat exchanger inside the steam generator and heat is transferred to the secondary coolant fluid by means of forced convection, conduction through the heat exchanger tube walls, and boiling on the outer surfaces of the tubes. No mixture of the primary and secondary coolant fluids occurs, which reduces the risk of radioactive particle transmittance. The pressurised steam generated in the secondary coolant passes through a steam turbine which generates electricity. The secondary coolant is then cooled and condensed prior to being pumped back into the steam generator. The cooled primary coolant is then pumped back into the reactor vessel, where the process is repeated (Schultz, 2006).

2.1.2 AHWR

The Advanced Heavy Water Reactor (AHWR) is a 300MWe (500 m^3/day of desalinated water) boiling, light water cooled, heavy water moderated, vertical

pressure tube type reactor currently being designed at the Bhabha Atomic Research Centre (BARC) in India. The reactor core is fuelled with clusters consisting of concentric rings of (Th–^{233}U)O_2 pins and (Th–Pu)O_2 pins. The core is submerged in borated heavy water which acts as both moderator and reflector and aids the twelve control rods in controlling reactor reactivity.

The basic functioning of the AHWR is as follows. Heat from nuclear fission in the fuel assemblies is transferred to the primary coolant fluid through natural convection. The coolant fluid boils and steam is separated in the steam drum and fed to the turbine. Excess steam is utilised by the desalination plant, fed through a condenser and then ultimately pumped back to the steam tank and gravity fed into the core (Sinha and Kakodkar, 2005).

2.1.3 SMART

The Small Modular Advanced Reactor Technology (SMART) is a PWR being studied by the Korea Atomic Energy Research Institute (KAERI) in Daejeon, South Korea, for the dual purpose applications of seawater desalination (40,000m^3/day) and small scale power generation (90 MWe). The SMART uses water as moderator and primary coolant, has a rated thermal power of 330 MWt and has a construction period of less than 36 months (International Atomic Energy Agency, 2006). The core of the SMART is designed to be fuelled with either low-enrichment uranium or a uranium and thorium mixture and can run for a maximum of 15 years before refuelling is required. Reactivity in the reactor is controlled by means of an external control drum (as opposed to internal control rods) surrounding the core, made of either cadmium or a boron carbide, and a beryllium reflector (Khatib-Rahbar, 2003).

2.1.4 APWR+

The Advanced Pressurized Water Reactor (APWR+) is a four-loop, 1500 MWe PWR currently under development in a joint venture between five Japanese utility companies (Hokkaido, Kansai, Shikoku, Kyushu, and Japan Atomic Power), Mitsubishi Heavy Industries Ltd, and Westinghouse Electric Corporation (Tujikura, 2000). The core of the APWR+ consists of 257 fuel assemblies designed to contain 121 tonnes of UO_2 or MOX fuel. Reactivity is controlled through 69 control rod clusters inserted axially into the core and a unique radial reflector design (Mitstemubishi Heavy Industries LTD, 2010).

2.1.5 KERENA

KERENA is a 1250 MWe Boiling Water Reactor (BWR) design (previously known as SWR-1000) developed by the French nuclear power conglomerate AREVA. The design is based on the Gundremmingen nuclear power plant but utilises extensive German input, yielding a reactor design with a 60 year operating life, that only needs refuelling every second year and can be built in less than 48

months (Stosic, 2008). The KERENA core consists of 664 fuel assemblies containing 136.3×10^3 kg of 3.54% enriched ^{235}U. Reactivity is controlled by means of 157 fine-motion control rod drives, as has been successfully used in German BWR designs since 1968.The basic design of the reactor is identical to established BWR designs except for dimensional changes and the incorporation of passive safety systems (Framatome ANP GmbH, 2002).

The basic function of the KERENA reactor (and all BWRs in general) is as follows. Heat from nuclear fission in the fuel assemblies is transferred to the primary coolant fluid through natural convection. Steam is formed in the reactor core and fed to steam turbines through the main steam lines at the top of the reactor, by natural circulation. The steam and condensate mixture exiting the turbine is fed through a condenser and ultimately pumped back into the reactor core through feedwater lines and then the cycle is repeated (Stosic, 2008).

2.1.6 ESBWR

The Economic Simplified Boiling Water Reactor (ESBWR) is a 1560 MWe modular reactor developed by General Electric Hitachi, based on their previous successes with advanced BWRs. The preliminary design was approved by the NRC and is currently awaiting Referred Combined *Construction and Operating License* (COL) approval (General Electric Hitachi Nuclear Energy, 2008).

The ESBWR is a light water moderated and cooled reactor with a core which consists of 1132 fuel assemblies containing 4.2% enriched UO_2 and supports a fuel cycle of 1-2 years (General Electric Hitachi Nuclear Energy, 2008). 269 control rod blades, utilising fine motion control rod drives, control the reactivity within the core and reportedly has the best-in-class core damage probability of 3×10^{-8} core damage events per reactor-year (Fennern, 2006).

2.1.7 PBMR

The Pebble Bed Modular Reactor (PBMR) is a 110 MWe gas cooled, high temperature reactor currently under development by Pebble Bed Modular Reactor (Pty) Limited in conjunction with several South African universities. What differentiates this design is its intrinsic safety as the reactivity diminishes as the fuel temperature rises. This has been demonstrated with the Arbeitsgemeinschaft Versuchsreaktor (AVR) built in Germany in 1960 (PBMR (Pty) Ltd, 2009).

The reactor employs enriched UO_2 particles coated in silicon carbide and pyrolitic carbon (TRISO particles). Approximately 15 000 of these particles are encased in a graphite sphere which forms the fuel pebble of 60 cm in diameter. When fully loaded, the reactor core will contain approximately 360 000 of these pebbles (Eskom, 2008).

The basic functioning of the PBMR is as follows. Helium gas (primary coolant) is fed into the top of the reactor core through a blower. Heat from nuclear fission in the fuel pebbles is transferred to the primary coolant fluid by natural convection. The hot primary fluid is then used to heat a secondary coolant fluid (light water) through a steam generator heat exchanger to ensure no radioactive particle transmittance. The pressurised steam generated in the secondary coolant passes through a steam turbine which generates electricity. This secondary coolant loop can also be coupled to a process plant to generate process heat, as well as for cogeneration (PBMR (Pty) Ltd, 2009). The secondary coolant is then cooled and condensed prior to being pumped back into the steam generator. The primary coolant is circulated through a recuperator, pre-intercooler, intercooler and compressors before re-entering the reactor core (Eskom, 2008).

2.1.8 IHTR-H

The Indian High Temperature Reactor (IHTR-H) is an 80 000 m^3/h hydrogen producing reactor concept currently being developed by the BARC, capable of producing process heat of around 1273 K. The design is based on the Compact HTR, which is essentially a 100 kWe technology demonstration module using the same base fuel particles as the PBMR, yielding a negative reactivity (Dulera & Sinha, 2008).

The IHTR-H core is made up of 19 prismatic Beryllium Oxide (BeO) moderator blocks containing TRISO particles, imbedded in a graphite fuel tube. The moderator blocks are surrounded by 18 BeO reflectors, which in turn are surrounded by graphite reflectors. The primary coolant is a Lead-Bismuth (Pb-Bi) eutectic alloy and seven tungsten shut-off rods are incorporated to shut down the reactor (Dulera & Sinha, 2008).

The basic functioning of the IHTR-H is as follows. The cold primary coolant is gravity fed into the reactor core where heat from nuclear fission in the fuel assemblies is transferred to the fluid by natural convection. A heated fluid then rises through the top of the core and passes through a turbine which generates electricity. The fluid is then fed through a recuperator, pre-cooler, compressor, inter-cooler, another compressor and then through the recuperator before re-entering the core and establishing natural circulation (Handra, 2008).

2.1.9 MASLWR

The Multi-Application Small Light Water Reactor (MASLWR) is a modular, 35 – 50 MWe, PWR developed by the Idaho National Engineering and Environmental Laboratory (INEEL), Nexant Inc. and the Oregon State University (OSU). The reactor was designed as a low cost, early implementation electricity generation unit with the flexibility of process heat applications (Modro, et al., 2002). The reactor core is designed for 24 fuel assemblies containing 8% enriched UO_2 fuel

pellets. At the current developmental stage, it is assumed that core and fuel design is similar to that of established PWRs.

The basic functioning of the MASLWR is as follows. The primary coolant enters the reactor core where heat from nuclear fission in the fuel assemblies is transferred to the fluid by natural convection, causing the fluid to rise. The hot primary coolant transfers heat through convection to the helical coil steam generator surrounding the core annulus, causing the secondary coolant fluid to boil. The cooled primary fluid returns to the bottom of the reactor pressure vessel establishing natural circulation. The secondary coolant leaves the pressure vessel as superheated steam and is fed to the turbine which generates electricity. The cooled fluid is then fed through a condenser and then pumped back into the steam generator, completing the circuit (Modro, et al., 2002).

2.2 Passive Safety Systems

This section describes passive safety systems employed in several generation IV reactor designs for core decay heat removal and reactor containment cooling only, as these are the major functions of the RCCS of the PBMR.

2.2.1 Core Decay Heat Removal Systems

This section described passive safety systems that focus on removing decay heat from the core after reactor shut down. All core decay heat removal systems are category C passive safety systems due to their reliance on mechanical components for activation.

2.2.1.1 Accumulators

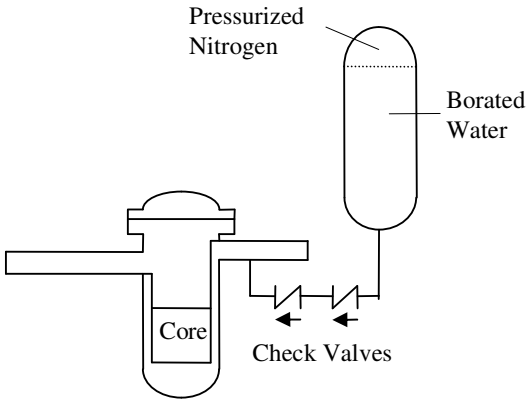

Figure 2-1: Schematic layout of an accumulator (International Atomic Energy Agency, 2006)

Pre-pressurized core flooding tanks, or accumulators, are designed to cool the core when system pressure drops rapidly, such as postulated loss of coolant

accident (LOCA) conditions. An accumulator consists of a large tank, 75% of which is filled with cold borated water, the rest with pressurized nitrogen, to ensure tank pressure equals normal operating system pressure (Tujikura, 2000). As can be seen in Figure 2-1, the accumulator is isolated from the reactor core by a series of check valves. During LOCA conditions, system pressure will drop below accumulator pressure, opening the valves and flooding the core with borated water. In doing so, accumulators aid core decay heat removal during plant shut down, as well as injecting boron, which acts as a neutron poison, ensuring cessation of the fission reaction (International Atomic Energy Agency, 2005).

2.2.1.2 Core Water Make-up Tanks

Elevated tank natural circulation loops, or core make-up tanks, are designed to supplement the primary coolant system during accident conditions when system pressure remains relatively high (United States Nuclear Regulatory Commission, 2008). As can be seen from Figure 2-2, the core make-up tank is isolated from the reactor core by a combination of a normally closed valve and a series of check valves. A normally open valve before the tank inlet ensures the tank contents are at system pressure. During accident conditions the valves open, allowing the cold borated water to be gravity fed into the core and forcing the hot primary coolant into the top of the tank, establishing natural circulation.

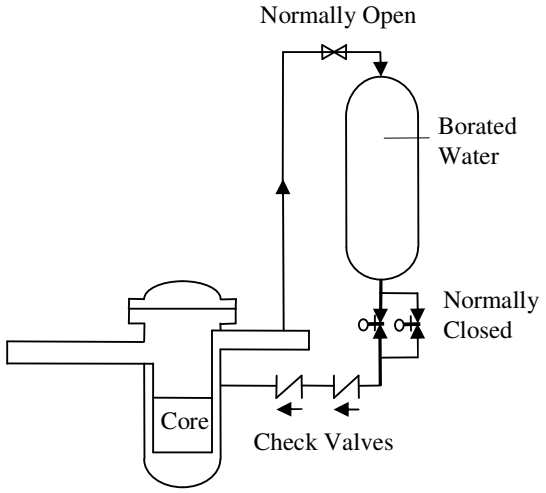

Figure 2-2: Schematic layout of a core make-up tank (International Atomic Energy Agency, 2006)

2.2.1.3 Gravity Drain Tanks

Gravity drain tanks are designed to flood the core during LOCA or forced shutdown accident conditions in low pressure reactors. This ensures that fuel integrity is maintained and that core decay heat is removed to maintain structural integrity for a specified period of time (Sinha and Kakodkar, 2005). As can be seen in Figure 2-3, the tank is isolated from the reactor core by a normally closed

valve or rupture disk and a series of check valves. During accident conditions, the valves are opened and the cold borated water is gravity driven into the core.

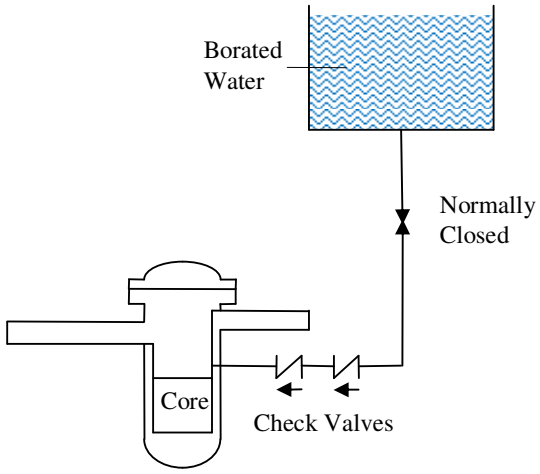

Figure 2-3: Schematic layout of a gravity drain tank (International Atomic Energy Agency, 2006)

2.2.1.4 Passive Residual Heat Removal Heat Exchangers

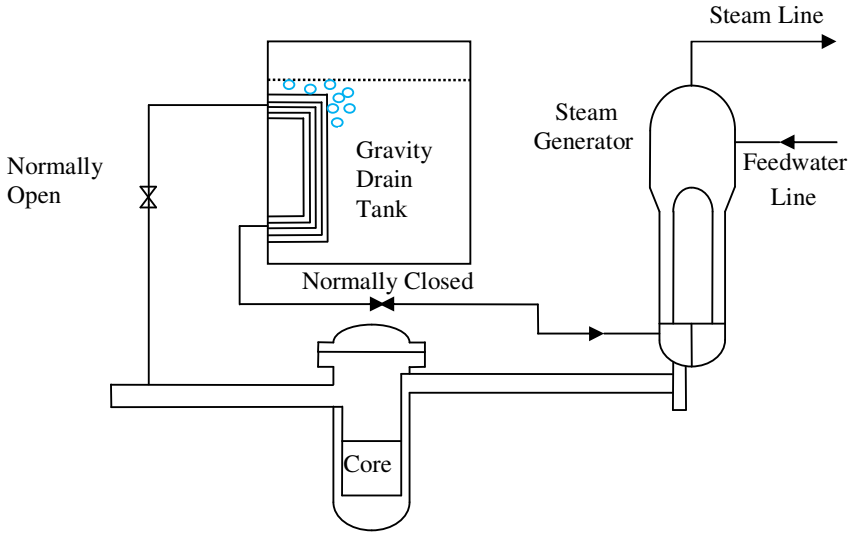

Figure 2-4: Schematic layout of a passive residual heat exchanger (International Atomic Energy Agency, 2006)

The passive residual heat removal heat exchanger is a single phase natural circulation loop that removes residual heat from the reactor core. As can be seen from Figure 2-4, a C-tube type heat exchanger is immersed in the gravity drain tank (as detailed in section 2.2.1.3). During LOCA conditions, the normally closed isolation valve is opened; hot water rises through the line attached to the

hot leg of the reactor and enters the heat exchanger at full system pressure and temperature. Heat is removed through boiling on the outside surface of the heat exchanger tubes. The cold coolant is gravity fed to the primary loop through the outline line attached to the steam generator, establishing natural circulation (International Atomic Energy Agency, 2005).

2.2.1.5 Passively Cooled Core Isolation Condensers

The passively cooled core isolation condenser serves the same purpose as the passive residual heat exchanger (as detailed in section 2.2.1.4) and is a two phase natural circulation loop. As can be seen in Figure 2-5, an isolation condenser is immersed in the gravity drain tank (as detailed in section 2.2.1.3). The condenser is isolated from the core through normally closed isolation valves. During LOCA conditions, the isolation valves are opened and steam from the core in BWRs (Framatome ANP GmbH, 2002), or the steam generator in PWRs (Sinha and Kakodkar, 2005), enters the condenser at full system pressure and temperature. Heat is removed by boiling on the outside surface of the heat exchanger tubes and the steam is condensed. The cold coolant is gravity fed to the core or steam generator establishing natural circulation.

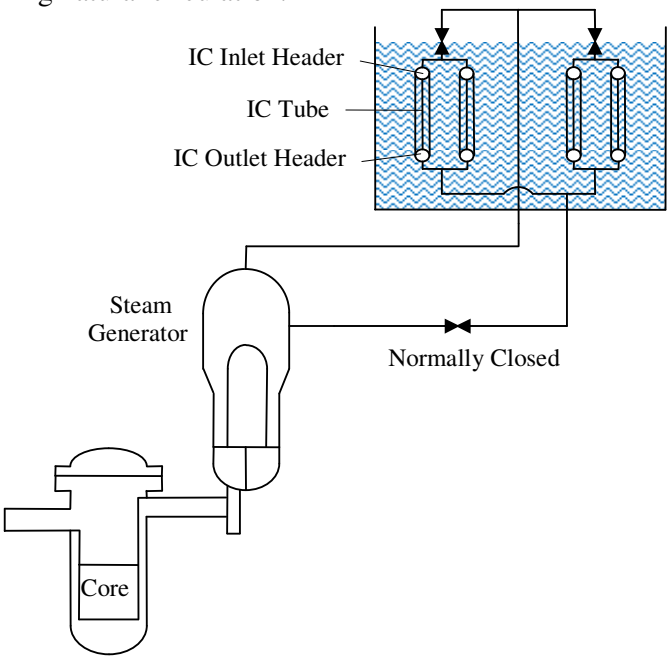

Figure 2-5: Schematic layout of a passively cooled core isolation condenser (International Atomic Energy Agency, 2006)

2.2.1.6 Sump Natural Circulation

In the event of LOCA conditions or ex-vessel severe accidents, the operator can act to flood the reactor cavity with the gravity drain tank. Once the reactor vessel is submerged, the sump valves are opened to establish a natural circulation path.

Decay heat is removed by natural convection, resulting in boiling and the generated steam is vented into the containment. Cooler water is then drawn in through the sump screens completing the loop. Sump natural circulation is designed to ensure vessel structural integrity (Westinghouse Electrical Company LLC, 2007). Figure 2-6 shows a schematic layout of sump natural circulation.

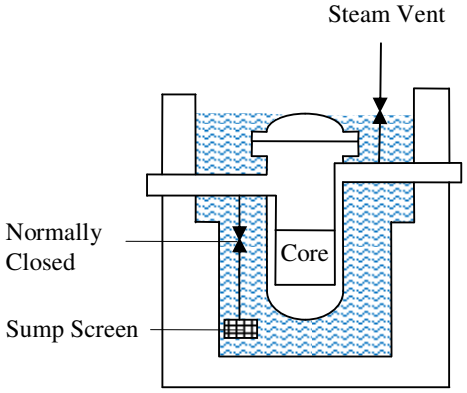

Figure 2-6: Schematic layout of sump natural circulation (International Atomic Energy Agency, 2006)

2.2.2 Containment Cooling Systems

This section described passive safety systems that focus on removing heat from the reactor containment.

2.2.2.1 Containment Passive Heat Removal Systems

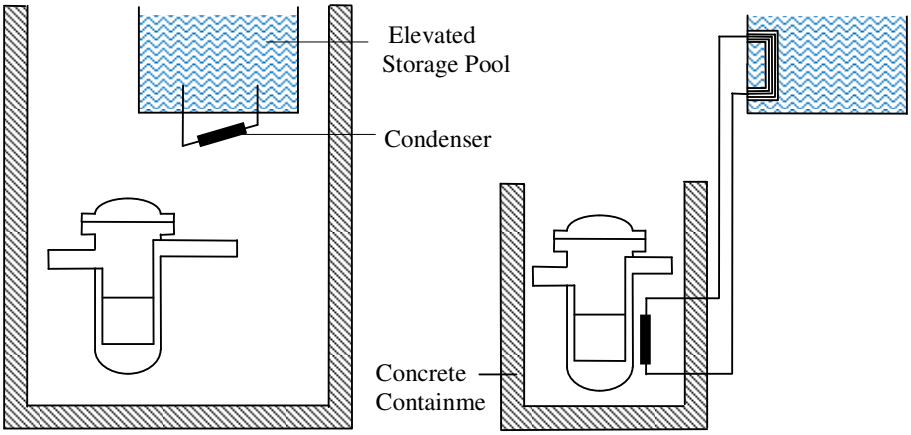

Figure 2-7: Schematic layout of containment passive heat removal systems (International Atomic Energy Agency, 2006)

Passive containment cooling systems are designed to protect the concrete structure of the reactor (Sinha and Kakodkar, 2005). As can be seen in Figure 2-7 the system consists of an elevated storage pool (usually the gravity drain tank) which

acts as a heat sink. Connecting the pool to the containment is a natural circulation loop, which ends in containment cooling condensers situated between the concrete structure and the RPV. If steam is released into the drywell atmosphere, the resulting heat is removed through steam condensation on the condenser pipes, heating the coolant and establishing natural circulation (Framatome ANP GmbH, 2002). As they require a moving working fluid, containment passive heat removal systems are a category B passive safety system.

2.2.2.2 Passive Containment Spray Systems

Passive containment spray systems require the reactor and all of the passive safety injection systems to be housed in a large steel vessel, which in turn resides inside a concrete *confinement* structure. This concrete structure has ducts that allow cool outside air to come into contact with the outside surface of the containment vessel. When steam is vented into the containment vessel, it rises until it comes into contact with the containment dome where it is cooled by liquid spray and condensed into liquid. The energy of the steam is transferred to the air on the outside of the containment by natural convection. As the air is heated, it rises and creates a natural circulation flow path that draws cool air in from the inlet duct and vents hot air out of the top of the concrete structure (International Atomic Energy Agency, 2005). Figure 2-8 shows a schematic layout of a passive containment spray system. Due to its reliance on spray mechanisms, this is a category C passive safety system.

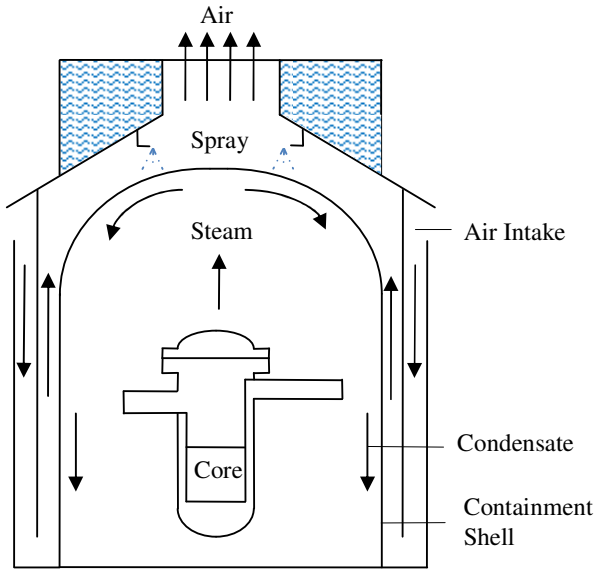

Figure 2-8: Schematic layout of passive containment spray system (International Atomic Energy Agency, 2006)

2.2.3 Comparison

Table 2-1: Reactor technology comparison

	Type	Thermal Power	Thermal Efficiency	Fuel	Coolant	Passive Safety Systems
AP1000	PWR	3400 MW	35.1%	< 4.95% UO_2	Light water	Accumulators Core Make-Up Tanks Gravity Drain Tanks Passive Residual Heat Exchangers Sump Natural Circulation Passive Containment Spray System
AHWR	HWR	920 MW	unknown	Th-Pu)O_2 :20 pins (Th-U^{233})O_2 : 32 pins	Light water	Accumulators Gravity Drain Tanks Passively Cooled Core Isolation Condensers Containment Passive Heat Removal System
SMART	BWR	330 MW	± 30%	U^{235} or a mixture (35% UO_2 – 65% ThO_2)	Light water	Accumulators Gravity Drain Tanks Passively Cooled Core Isolation Condensers Sump Natural Circulation Containment Passive Heat Removal System
APWR+	PWR	4451 MW	39%	UO_2	Light water	Accumulators Gravity Drain Tanks Passive Containment Spray System
KERENA	BWR	3370 MW	37.2%	3.54% U^{235}	Light water	Gravity Drain Tanks Passively Cooled Core Isolation Condensers Sump Natural Circulation Containment Passive Heat Removal System
ESBWR	BWR	4500 MW	34.7%	4.2% UO_2	Light water	Gravity Drain Tanks Passively Cooled Core Isolation Condensers Containment Passive Heat Removal System
PBMR	HTR	400 MW	41%	U^{235} or a mixture (35% UO_2 – 65% ThO_2) TRISO coated particles in graphite spheres	Helium	Containment Passive Heat Removal System
IHTR-H	HTR	600 MW	40-57%	$^{233}UO_2$ and ThO_2 based TRISO coated particles in graphite spheres	Pb/Molten Salt	Containment Passive Heat Removal System
MASLWR	PWR	150 MW	unknown	8% UO_2 pellets	Light water	Sump Natural Circulation Containment Passive Heat Removal System

Table 2-1 gives a summarised comparison between the current generation IV reactor designs discussed in section 2.1. Included are: the type of nuclear power reactor, rated or expected thermal power and efficiency, type of fuel used, coolant used and the passive safety systems incorporated (as discussed in section 2.2). The table shows that nuclear reactors dependent on conventional fuel pins and assemblies, though capable of much higher thermal power output, are less efficient and require the implementation of more passive safety systems than PBMR, IHTR-H and MASLWR reactors. The TRISO fuel particles enhance the

safety of the reactors while the differences in thermal power output are due to the modular design of the smaller reactors.

When looking at the passive safety systems incorporated in the designs, it is important to note that all the reactors implement a passive containment heat removal system. It is also interesting to note that the reactor designs using conventional fuel all make use of gravity drain tanks as well as isolation condensers to maintain core and fuel integrity during LOCA conditions. The nature of the TRISO particle allows very high temperature operation without loss in fuel integrity and the passive containment heat removal system aids in the removal of core decay heat from the cavity between the reactor pressure vessel and the reactor containment. This eliminates the need for the gravity drain tanks and associated passive safety systems.

2.3 Natural Circulation Simulation Theory

2.3.1 General Conservation Equations

This section presents and explains the general one-dimensional two-fluid conservation equations that serve as the basis for the numerical modelling of natural circulation loops (Reyes, 2007). It is assumed that the density of each phase and the cross-sectional area is constant.

The first transport equation considered is the conservation of mass for each phase, k, as given by (Reyes, 2007):

$$\frac{\partial}{\partial t}\{\rho_k \alpha_k\} + \frac{\partial}{\partial z}\{\rho_k v_k \alpha_k\} = \Gamma_k \qquad (2\text{-}1)$$

In equation 2-1:

$\frac{\partial}{\partial t}\{\rho_k \alpha_k\}$ = Time rate of change of area averaged mass (kg/s/m^3)

$\frac{\partial}{\partial z}\{\rho_k v_k \alpha_k\}$ = Change in area averaged mass along the flow axis (kg/s/m^3)

Fluid phase parameters, $\{\psi_k\}$, have been averaged over the cross-sectional area as follows:

$$\{\psi_k\} \equiv \frac{1}{A}\iint_A \psi_k dA \qquad (2\text{-}2)$$

The conservation of momentum for each phase is given by (Reyes, 2007):

$$\frac{\partial}{\partial t}\{\rho_k v_k \alpha_k\} + \frac{\partial}{\partial z}\{\rho_k v_k^2 \alpha_k\} = \{\Gamma_k \vec{v}_{ks} \cdot \vec{n}_z\} + \sum_{i=1}^{N}\{\vec{F}_{wk} \cdot \vec{n}_z\}_i - \frac{\partial}{\partial z}\{P_k \alpha_k\} + \{\vec{F}_{sk} \cdot \vec{n}_z\} + \{\rho_k \alpha_k\}\vec{g} \cdot \vec{n}_z \qquad (2\text{-}3)$$

Where:

$\frac{\partial}{\partial t}\{\rho_k v_k \alpha_k\}$ = Time rate of change of area averaged momentum (kg/m^2/s^2)

$\frac{\partial}{\partial z}\{\rho_k v_k^2 \alpha_k\}$ = Change in momentum along flow axis

$\{\Gamma_k \vec{v}_{ks} \cdot \vec{n}_z\}$ = Rate of momentum transfer due to phase change

$\vec{v}_{ks} \cdot \vec{n}_z$ = Interface velocity of phase along z-co-ordinate (scalar +/-)
$\sum_{i=1}^{N}\{\vec{F}_{wk} \cdot \vec{n}_z\}_i$ = Sum of fluid phase drag forces on structures in flow
$\frac{\partial}{\partial z}\{P_k \alpha_k\}$ = Pressure gradient along axis of flow
$\{\vec{F}_{sk} \cdot \vec{n}_z\}$ = Drag forces acting on fluid phase interface
$\{\rho_k \alpha_k\}\vec{g} \cdot \vec{n}_z$ = Gravity forces acting in direction of flow

The conservation of energy for each phase (neglecting axial heat conduction and axial shear) is given by (Reyes, 2007):

$$\frac{\partial}{\partial t}\{\rho_k u_k^{\circ} \alpha_k\} + \frac{\partial}{\partial z}\{\rho_k h_k^{\circ} v_k \alpha_k\} = \Gamma_k h_{ks}^{\circ} - \left\{P_k \frac{\partial \alpha_k}{\partial t}\right\} + \sum_{i=1}^{N}\left\{q_k^{"} \alpha_k \frac{P}{A}\right\}_i - \{\rho_k g v_k \alpha_k\} + \{Q_{sk}\} \quad (2\text{-}4)$$

In equation 2-4:
$\frac{\partial}{\partial t}\{\rho_k u_k^{\circ} \alpha_k\}$ = Time rate of change of area averaged energy for given phase
$\frac{\partial}{\partial z}\{\rho_k h_k^{\circ} v_k \alpha_k\}$= Change in energy along the flow axis
$\Gamma_k h_{ks}^{\circ}$ = Rate of energy transfer due to phase change
$\left\{P_k \frac{\partial \alpha_k}{\partial t}\right\}$ = Pressure work due to changes in void fraction
$\sum_{i=1}^{N}\left\{q_k^{"} \alpha_k \frac{P}{A}\right\}_i$ = Sum of heat transfer between fluid phase and structures in flow
$\{\rho_k g v_k \alpha_k\}$ = Work due to gravity
$\{Q_{sk}\}$ = Interfacial heat transfer

Equation 2-4 is expressed in terms of the stagnation energy, u_k°, and stagnation enthalpy, h_k°, which are defined as follows (Mills, 1999):

$$u_k^{\circ} = u_k + \frac{v_k^2}{2} \quad (2\text{-}5)$$

$$h_k^{\circ} = u_k^{\circ} + \frac{P_k}{\rho_k} \quad (2\text{-}6)$$

2.3.2 Two-Phase Flow Simulation Models

The *exact* approach to modelling two-phase flow (with equal phase pressures) is to use the two-fluid, non-equilibrium, conservation equations as described in section 2.3.1. This results in a mass, momentum and energy conservation equation for each phase and is referred to as the 6-equation model. The difficulty in working with this model lies in the constitutive laws required:

- Correlations describing friction between the conduit wall and each phase
- Correlations describing heat transferred between the conduit wall and each phase
- A correlation describing interfacial mass transport, i.e. mass transferred between the two phases
- A correlation describing interfacial momentum transport
- A correlation describing interfacial energy transport

Because of this difficulty, several simplified models have been derived by making use of mixture equations or mixture equations in conjunction with individual phase equations, to reduce the number of constitutive correlations. The following sections will look at the resulting 5-equation, 4-equation and 3-equation models for two-phase flow. Reyes (2007) gives a concise summary of the different models available. This can been seen in Table 2-2 which gives the conservation equations required for each model, restrictions placed on the model in order to limit the constitutive laws required, the constitutive laws required to solve the equations and the parameters calculated upon solving.

In the 5-equation models, only one restriction is placed on the fluid phases, eliminating one constitutive law in the 6-equation model. The four variations of the 5-equation model are shown in Table 2-2. The two-fluid partial non-equilibrium model assumes partial thermal equilibrium. This means that one of the two phases is at the saturation temperature corresponding to the local pressure, $T_v = T_{sat@P}$ or $T_l = T_{sat@P}$, eliminating one of the conservation equations (either mass or energy depending on how the restriction is applied). The slip or drift non-equilibrium model describes the relative velocity between the two phases by the use of either a slip factor (S), or a flow pattern dependent drift velocity correlation (V_{vj}). This eliminates one of the momentum conservation equations. The last of the 5-equation models, the homogenous non-equilibrium model, assumes equal velocity, i.e. $v_v = v_l = v_m$. This eliminates one of the momentum conservation equations.

Although each one of the 5-equation models eliminate one of the constitutive laws required, the difficulties of describing interfacial mass, momentum and energy transport still arise. The 4-equation models introduce another restriction, eliminating another conservation equation. The four different models can be seen in Table 2-2. The two-fluid equilibrium model assumes full thermal equilibrium. In other words, both phases are at saturation temperature corresponding to local pressure, $T_l = T_v = T_{sat@P}$. This assumption eliminates a mass and energy conservation equation. The drift or slip partial non-equilibrium model assumes partial thermal equilibrium as well as a relative velocity between the two phases described by either the slip ratio or a drift velocity correlation. The homogenous partial non-equilibrium model assumes partial thermal equilibrium as well as equal velocity.

The 3-equation models eliminate the interfacial constitutive laws required, simplifying the simulation drastically. Most two-phase natural circulation simulations in the nuclear field make use of these models though development of more encompassing constitutive correlations is under way to facilitate the use of the less restrictive models (International Atomic Energy Agency, 2005). The development of the 3-equation models is discussed in more detail in the next section.

Table 2-2: Two-phase flow models with equal phase pressures (Reyes, 2007)

Conservation Equations	Restrictions	Constitutive Laws	Parameter
6-Equation Model			
Two-Fluid Non-Equilibrium (2) Mass Phase Balance (2) Momentum Phase Balance (2) Energy Phase Balance	None	(2) Phase wall friction (2) Phase heat flux (1) Interfacial mass (1) Interfacial momentum (1) Interfacial energy	α, P, v_l, v_v T_l, T_v
5-Equation Models			
Two-Fluid Partial Non-Equilibrium (2) Mass Phase Balance (2) Momentum Phase Balance (1) Mixture Energy Balance	$T_l = T_{sat@P}$ or $T_v = T_{sat@P}$	(2) Phase wall friction (1) Mixture wall heat flux (1) Interfacial mass (1) Interfacial momentum	α, P, v_l, v_v $T_l \; or \; T_v$
Two-Fluid Partial Non-Equilibrium (1) Mixture Mass Balance (2) Momentum Phase Balance (2) Energy Phase Balance	$T_l = T_{sat@P}$ or $T_v = T_{sat@P}$	(2) Phase wall friction (2) Phase heat flux (1) Interfacial mass (1) Interfacial momentum (1) Interfacial energy	α, P, v_l, v_v $T_l \; or \; T_v$
Slip or Drift Non-Equilibrium (2) Mass Phase Balance (1) Mixture Momentum Balance (2) Energy Phase Balance	Slip or Drift Velocity	(1) Mixture wall friction (2) Phase heat flux (1) Interfacial mass (1) Interfacial energy (1) Slip velocity or Drift flux	α, P, T_l, T_v v_m
Homogenous Non-Equilibrium (2) Mass Phase Balance (1) Mixture Momentum Balance (2) Energy Phase Balance	$v_v = v_l = v_m$	(1) Mixture wall friction (2) Phase heat flux (1) Interfacial mass (1) Interfacial energy	α, P, T_l, T_v v_m
4-Equation Models			
Two-Fluid Equilibrium (1) Mixture Mass Balance (2) Momentum Phase Balance (1) Mixture Energy Balance	$T_l = T_v$ $= T_{sat@P}$	(2) Phase wall friction (1) Mixture heat flux (1) Interfacial mass (1) Interfacial momentum	α, P, v_l, v_v
Drift or Slip Partial Non-Equilibrium (1) Mixture Mass Balance (1) Mixture Momentum Balance (2) Phase Energy Balance	Slip or Drift Velocity $T_l = T_{sat@P}$ or $T_v = T_{sat@P}$	(1) Mixture wall friction (1) Mixture wall heat flux (1) Interfacial mass (1) Drift flux correlation	α, P, v_m $T_l \; or \; T_v$
Homogeneous Partial Non-Equilibrium (1) Mixture Mass Balance (1) Mixture Momentum Balance (2) Phase Energy Balance	$v_v = v_l = v_m$ $T_l = T_{sat@P}$ or $T_v = T_{sat@P}$	(1) Mixture wall friction (2) Phase wall heat flux (1) Interfacial mass (1) Interfacial energy	α, P, v_m $T_l \; or \; T_v$
3-Equation Models			
Homogeneous Equilibrium (HEM): (1) Mixture Mass Balance (1) Mixture Momentum Balance (1) Mixture Energy Balance	$v_v = v_l = v_m$ $T_l = T_v$ $= T_{sat@P}$	(1) Mixture wall friction (1) Mixture wall heat flux	α, P, v_m
Slip or Drift Equilibrium: (1) Mixture Mass Balance (1) Mixture Momentum Balance (1) Mixture Energy Balance	Slip or Drift Velocity $T_l = T_v$ $= T_{sat@P}$	(1) Mixture wall friction (1) Mixture wall heat flux (1) Slip velocity or Drift flux	α, P, v_m

2.3.2.1 Homogenous Equilibrium Model (HEM)

In order to generate the homogenous equilibrium model, the individual fluid phases are assumed to behave as a flowing mixture. The mixture equations can then be generated from the general governing equations (equations 2-1, 2-3 and 2-4). This is done by first defining the interfacial jump conditions.

Mass: $\sum_{k=1}^{2} \Gamma_k = 0$ (2-7)
This condition states that the sum of the mass generated is zero.

Momentum: $\sum_{k=1}^{2} \left(\Gamma_k \vec{v}_{ks} \cdot \vec{n}_z + \vec{F}_{sk} \cdot \vec{n}_z\right) = 0$ (2-8)
This condition states that the sum of the drag forces acting on fluid phase interface is zero.

Energy: $\sum_{k=1}^{2} \left(\Gamma_k h_{ks}^{\circ} + Q_{sk}\right) = 0$ (2-9)
This condition states that the sum of the rate of energy transfer due to phase change and interfacial heat transfer for the two phases is zero. In other words, the net heat transfer between the phases is zero.

The mixture properties are defined as follows (Reyes, 2007):

Mixture Density: $\rho_m = \{\rho_v \alpha + \rho_l (1-\alpha)\}$ (2-10)

Area Averaged Density: $\langle \rho_m \rangle = \frac{\dot{m}_m^2}{\{\rho_v v_v^2 \alpha + \rho_l v_l^2\}(1-\alpha)}$ (2-11)

Mixture Mass Flux: $\dot{m}_m = \{\rho_v v_v \alpha + \rho_l v_l (1-\alpha)\}$ (2-12)

Density Averaged Mixture Enthalpy: $\langle h_m \rangle = \frac{\{\rho_v h_v \alpha + \rho_l h_l (1-\alpha)\}}{\rho_m}$ (2-13)

Area Mixture Enthalpy: $\langle h_m \rangle = \frac{\{\rho_v h_v v_v \alpha + \rho_l h_l v_l (1-\alpha)\}}{\dot{m}_m}$ (2-14)

Mixture Pressure: $P_m = \{P_v \alpha + P_l (1-\alpha)\}$ (2-15)

Mixture Velocity: $v_m = \frac{\{\rho_v v_v \alpha + \rho_l v_l (1-\alpha)\}}{\rho_m}$ (2-16)

Density Averaged Mixture Internal Energy: $u_m = \frac{\{\rho_v u_v \alpha + \rho_l u_l (1-\alpha)\}}{\rho_m}$ (2-17)

The first step in generating the mixture mass conservation equation is to add the mass conservation equation (equation 2-1) for each phase together:

$$\frac{\partial}{\partial t}\{\rho_l \alpha_l\} + \frac{\partial}{\partial z}\{\rho_l v_l \alpha_l\} + \frac{\partial}{\partial t}\{\rho_v \alpha_v\} + \frac{\partial}{\partial z}\{\rho_v v_v \alpha_v\} = \Gamma_l + \Gamma_v \quad (2\text{-}18)$$

Applying the interfacial jump condition for mass (equation 2-7) to equation 2-18:

$$\frac{\partial}{\partial t}\{\rho_l \alpha_l\} + \frac{\partial}{\partial z}\{\rho_l v_l \alpha_l\} + \frac{\partial}{\partial t}\{\rho_v \alpha_v\} + \frac{\partial}{\partial z}\{\rho_v v_v \alpha_v\} = 0$$

$$\therefore \frac{\partial}{\partial t}\{\rho_l \alpha_l + \rho_v \alpha_v\} + \frac{\partial}{\partial z}\{\rho_l v_l \alpha_l + \rho_v v_v \alpha_v\} = 0$$

But $\alpha_l = 1 - \alpha_v$

$$\therefore \frac{\partial}{\partial t}\{\rho_l (1-\alpha_v) + \rho_v \alpha_v\} + \frac{\partial}{\partial z}\{\rho_l v_l (1-\alpha_v) + \rho_v v_v \alpha_v\} = 0 \quad (2\text{-}19)$$

Applying equations 2-10 and 2-12 to equation 2-19 yields the mixture mass conservation equation:

$$\frac{\partial \rho_m}{\partial t} + \frac{\partial \dot{m}_m}{\partial z} = 0 \qquad (2\text{-}20)$$

To generate the mixture momentum conservation equation, the first step is to add the momentum conservation equation (equation 2-3) for each phase together:

$$\frac{\partial}{\partial t}\{\rho_l v_l \alpha_l\} + \frac{\partial}{\partial z}\{\rho_l v_l^2 \alpha_l\} + \frac{\partial}{\partial t}\{\rho_v v_v \alpha_v\} + \frac{\partial}{\partial z}\{\rho_v v_v^2 \alpha_v\} = \{\Gamma_l \vec{v}_{ls} \cdot \vec{n}_z\}$$
$$+ \sum_{i=1}^{N}\{\vec{F}_{wl} \cdot \vec{n}_z\}_i - \frac{\partial}{\partial z}\{P_l \alpha_l\} + \{\vec{F}_{sl} \cdot \vec{n}_z\} + \{\rho_l \alpha_l\}\vec{g} \cdot \vec{n}_z + \{\Gamma_v \vec{v}_{vs} \cdot \vec{n}_z\}$$
$$+ \sum_{i=1}^{N}\{\vec{F}_{wv} \cdot \vec{n}_z\}_i - \frac{\partial}{\partial z}\{P_v \alpha_v\} + \{\vec{F}_{sv} \cdot \vec{n}_z\} + \{\rho_v \alpha_v\}\vec{g} \cdot \vec{n}_z$$

But $\alpha_l = 1 - \alpha_v$

$$\therefore \frac{\partial}{\partial t}\{\rho_l v_l (1-\alpha_v)\} + \frac{\partial}{\partial z}\{\rho_l v_l^2 (1-\alpha_v)\} + \frac{\partial}{\partial t}\{\rho_v v_v \alpha_v\} + \frac{\partial}{\partial z}\{\rho_v v_v^2 \alpha_v\} = \{\Gamma_l \vec{v}_{ls} \cdot \vec{n}_z\}$$
$$+ \sum_{i=1}^{N}\{\vec{F}_{wl} \cdot \vec{n}_z\}_i - \frac{\partial}{\partial z}\{P_l (1-\alpha_v)\} + \{\vec{F}_{sl} \cdot \vec{n}_z\} + \{\rho_l (1-\alpha_v)\}\vec{g} \cdot \vec{n}_z$$
$$+\{\Gamma_v \vec{v}_{vs} \cdot \vec{n}_z\} \; + \sum_{i=1}^{N}\{\vec{F}_{wv} \cdot \vec{n}_z\}_i - \frac{\partial}{\partial z}\{P_v \alpha_v\} + \{\vec{F}_{sv} \cdot \vec{n}_z\} + \{\rho_v \alpha_v\}\vec{g} \cdot \vec{n}_z$$

Applying the interfacial jump condition for momentum (equation 2-8) yields:

$$\frac{\partial}{\partial t}\{\rho_l v_l (1-\alpha_v) + \rho_v v_v \alpha_v\} + \frac{\partial}{\partial z}\{\rho_l v_l^2 (1-\alpha_v) + \rho_v v_v^2 \alpha_v\} =$$
$$-\frac{\partial}{\partial z}\{P_l (1-\alpha_v) + P_v \alpha_v\} + \{\rho_l (1-\alpha_v) + \rho_v \alpha_v\}\vec{g} \cdot \vec{n}_z$$
$$+ \sum_{i=1}^{N}\{\vec{F}_{wl} \cdot \vec{n}_z + \vec{F}_{wv} \cdot \vec{n}_z\}_i \qquad (2\text{-}21)$$

The definition of the dot product states (Zill & Cullen, 2000):

$$\vec{a} \cdot \vec{b} = \|a\|\|b\| cos\theta \qquad (2\text{-}22)$$

Where θ refers to the acute angle between vectors *a* and *b*.

Applying equation 2-22 reduces equation 2-21 to:

$$\frac{\partial}{\partial t}\{\rho_l v_l (1-\alpha_v) + \rho_v v_v \alpha_v\} + \frac{\partial}{\partial z}\{\rho_l v_l^2 (1-\alpha_v) + \rho_v v_v^2 \alpha_v\} =$$
$$-\frac{\partial}{\partial z}\{P_l (1-\alpha_v) + P_v \alpha_v\} - \{\rho_l (1-\alpha_v) + \rho_v \alpha_v\} g cos\theta - \sum_{i=i}^{N} F_{wi} \qquad (2\text{-}23)$$

Because the drag force acts parallel but in opposite direction to the normal force, $\vec{F}_{sk} \cdot \vec{n}_s = -F_{sk}$ and $\vec{g} \cdot \vec{n}_z = -g cos\theta$.

Where θ refers to the angle between the horizontal and the normal vector.

Applying equations 2-10, 2-11 and 2-12 to equation 2-23, yields the mixture momentum conservation equation:

$$\frac{\partial \dot{m}_m}{\partial t} + \frac{\partial}{\partial z}\left\{\frac{\dot{m}_m^2}{\langle \rho_m \rangle}\right\} = -\frac{\partial P_m}{\partial z} - \rho_m g cos\theta - \sum_{i=i}^{N} F_{wi} \qquad (2\text{-}24)$$

To generate the mixture energy conservation equation, the first step is to add the energy conservation equation (equation 2-4) for each phase together:

$$\frac{\partial}{\partial t}\left\{\rho_l u_l^{\circ} \alpha_l\right\} + \frac{\partial}{\partial z}\left\{\rho_l h_l^{\circ} v_l \alpha_l\right\} + \frac{\partial}{\partial t}\left\{\rho_v u_v^{\circ} \alpha_v\right\} + \frac{\partial}{\partial z}\left\{\rho_v h_v^{\circ} v_v \alpha_v\right\} = \Gamma_l h_{ls}^{\circ} - \left\{P_l \frac{\partial \alpha_l}{\partial t}\right\}$$
$$+ \sum_{i=1}^{N}\left\{q_l^{"} \alpha_l \frac{P}{A}\right\}_i - \{\rho_l g v_l \alpha_l\} + \{Q_{sl}\} + \Gamma_v h_{vs}^{\circ} - \left\{P_v \frac{\partial \alpha_v}{\partial t}\right\} + \sum_{i=1}^{N}\left\{q_v^{"} \alpha_v \frac{P}{A}\right\}_i$$
$$-\{\rho_v g v_v \alpha_v\} + \{Q_{sv}\}$$

But $\alpha_l = 1 - \alpha_v$

$$\therefore \frac{\partial}{\partial t}\{\rho_l u_l^{\circ}(1-\alpha_v)+\rho_v u_v^{\circ}\alpha_v\}+\frac{\partial}{\partial z}\{\rho_l h_l^{\circ} v_l(1-\alpha_v)+\rho_v h_v^{\circ} v_v\alpha_v\}=\Gamma_l h_{ls}^{\circ}+\Gamma_v h_{vs}^{\circ}$$
$$-\left\{P_l\frac{\partial(1-\alpha_v)}{\partial t}+P_v\frac{\partial\alpha_v}{\partial t}\right\}+\sum_{i=1}^{N}\left\{q_l^{''}(1-\alpha_v)\frac{P}{A}+q_v^{''}\alpha_v\frac{P}{A}\right\}_i$$
$$-\{\rho_l g v_l(1-\alpha_v)+\rho_v g v_v\alpha_v\}+\{Q_{sl}\}+\{Q_{sv}\}$$

Applying the interfacial jump condition for energy (equation 2-8) yields:

$$\frac{\partial}{\partial t}\{\rho_l u_l^{\circ}(1-\alpha_v)+\rho_v u_v^{\circ}\alpha_v\}+\frac{\partial}{\partial z}\{\rho_l h_l^{\circ} v_l(1-\alpha_v)+\rho_v h_v^{\circ} v_v\alpha_v\}=-\left\{P_l\frac{\partial(1-\alpha_v)}{\partial t}+P_v\frac{\partial\alpha_v}{\partial t}\right\}$$
$$+\sum_{i=1}^{N}\left\{q_l^{''}(1-\alpha_v)\frac{P}{A}+q_v^{''}\alpha_v\frac{P}{A}\right\}_i-\{\rho_l g v_l(1-\alpha_v)+\rho_v g v_v\alpha_v\} \quad (2\text{-}25)$$

In order to simplify the above equation, it is assumed that the liquid and vapour pressures are equal (i.e. $P_v = P_l$) and that the heat flux between fluid phases and structures are equal (i.e. $q_v^{''} = q_l^{''}$). With these assumptions and applying equations 2-12, 2-13 and 2-17, equation 2-25 reduces to:

$$\frac{\partial}{\partial t}\{u_m\rho_m\}+\frac{\partial}{\partial z}\{\dot{m}_m\langle h_m\rangle\}=\sum_{i=1}^{N}\left\{\frac{q_i^{''}P_i}{A_i}\right\}-\{\dot{m}_m g\} \quad (2\text{-}26)$$

From the definition of specific enthalpy (Mills, 1999):

$$h_m = u_m+\frac{P_m}{\rho_m} \qquad \therefore u_m\rho_m = h_m\rho_m - P_m \quad (2\text{-}27)$$

Replacing the first term in equation 2-26 with the above equation yields:

$$\frac{\partial}{\partial t}\{h_m\rho_m - P_m\}+\frac{\partial}{\partial z}\{\dot{m}_m\langle h_m\rangle\}=\sum_{i=1}^{N}\left\{\frac{q_i^{''}P_i}{A_i}\right\}-\{\dot{m}_m g\} \quad (2\text{-}28)$$

In order to evaluate the last term in equation 2-28, the mixture momentum equation is reconsidered assuming steady state flow (i.e. mass flux does not vary with time) and that mixture density does not vary with position. Equation 2-24 can then be rewritten as follows:

$$\frac{\partial\dot{m}_m}{\partial t}+\frac{\partial}{\partial z}\left\{\frac{\dot{m}_m^2}{\langle\rho_m\rangle}\right\}=-\frac{\partial P_m}{\partial z}-\rho_m g\cos\theta-\sum_{i=i}^{N}F_{wi}=0$$
$$\therefore g=-\frac{1}{\rho_m\cos\theta}\left(\frac{\partial P_m}{\partial z}+\sum_{i=i}^{N}F_{wi}\right) \quad (2\text{-}29)$$

Applying equation 2-29 to equation 2-28 yields the mixture energy equation:

$$\frac{\partial}{\partial t}\{h_m\rho_m - P_m\}+\frac{\partial}{\partial z}\{\dot{m}_m\langle h_m\rangle\}=\sum_{i=1}^{N}\left\{\frac{q_i^{''}P_i}{A_i}\right\}+\frac{\dot{m}_m}{\rho_m\cos\theta}\left(\frac{\partial P_m}{\partial z}+\sum_{i=i}^{N}F_{wi}\right) \quad (2\text{-}30)$$

2.3.2.2 Drift Flux Model

Zuber and Findlay (1965) developed the drift flux model in order to introduce the relative velocity between the fluid phases into the mixture equations. The result is a flow regime dependent two-phase flow model.

The drift flux model introduces a relative velocity between the phases defined as:

$$v_r = (v_v - v_l) \quad (2\text{-}31)$$

The drift velocities of the two phases are related to the relative velocity as:

$$V_{vj} = v_r(1-\alpha) \quad (2\text{-}32)$$
$$V_{lj} = -v_r\alpha \quad (2\text{-}33)$$

Zuber and Findlay (1965) also developed flow pattern dependent correlations for the drift velocity:

Churn-Turbulent Flow: $$V_{vj} = 1.41\left(\frac{\sigma g(\rho_l-\rho_v)}{\rho_l^2}\right)^{1/4} \quad (2\text{-}34)$$

Slug Flow: $$V_{vj} = 0.35\left(\frac{g(\rho_l-\rho_v)D}{\rho_l}\right)^{1/2} \quad (2\text{-}35)$$

Annular Flow: $$V_{vj} = 23\frac{\Delta\rho}{\rho_l}\left(\frac{\mu_l(1-\{\alpha\})v_l}{\rho_v D}\right)^{1/2} \quad (2\text{-}36)$$

Equations 2-31 and 2-32 are incorporated into the mixture conservation equations (equations 2-20, 2-24 and 2-30) and yield the drift flux conservation equations:

Mass:
$$\frac{\partial\rho_m}{\partial t} + \frac{\partial}{\partial z}(\rho_m v_m) = 0 \quad (2\text{-}37)$$

Momentum:
$$\rho_m\frac{\partial v_m}{\partial t} + \rho_m v_m\frac{\partial v_m}{\partial z} + \frac{\partial}{\partial z}\left[\frac{\rho_v\rho_l\alpha V_{vj}^2}{\rho_m(1-\alpha)}\right] = -\sum_{i=1}^{N}F_{wi} - \frac{\partial P_m}{\partial z} - \rho_m g\cos\theta \quad (2\text{-}38)$$

Energy:
$$\frac{\partial}{\partial t}\{\rho_m u_m\} + \frac{\partial}{\partial z}\{\rho_m u_m v_m\} + \frac{\partial}{\partial z}\left[\frac{\alpha\rho_l\rho_v(u_v-u_l)V_{vj}}{\rho_m}\right] + P_m\frac{\partial v_m}{\partial z}$$
$$+P_m\frac{\partial}{\partial z}\left[\frac{\alpha(\rho_l-\rho_v)V_{vj}}{\rho_m}\right] = \sum_{i=1}^{N}q_i''\frac{P_i}{A_i} + v_m\sum_{i=1}^{N}F_{wi} \quad (2\text{-}39)$$

2.4 Heat Transfer Correlations

In order to solve the equations generated in section 2.3.2.1, it is necessary to describe the heat transferred to the working fluid in each control volume. The difficulty lies in the dependence of heat transfer on the fluid velocity and whether single or two-phase flow exists. Literature shows that several heat transfer correlations have been developed. The correlations discussed in this section are divided into single phase and two-phase correlations. Unless otherwise stated, the heat transfer coefficient is determined from the Nusselt number as follows:

$$h = \frac{Nu_D k}{D} \quad (2\text{-}40)$$

For the single phase, laminar flow heat transfer coefficient, the correlation of Collier (1994) for the Nusselt number is:

$$Nu_D = 0.17Re_D^{0.33}Pr^{0.43}\left(\frac{Pr}{Pr_w}\right)^{0.25}Gr^{0.1} \qquad Re_D \le 2000 \quad (2\text{-}41)$$

In equation 2-41, fluid properties are evaluated at bulk fluid temperatures, excepting Pr_w, which is evaluated at the wall temperature. The equation is only valid in vertical flow where the length from tube inlet exceeds 50 diameters

(Collier and Thome, 1994). Collier and Thome (1994), in their text, do not specify the experimental ranges from which this correlation was derived.

For the single phase, turbulent flow heat transfer coefficient, the correlation of Gnielinski for the Nusselt number (Mills, 1999) is:

$$Nu_D = \frac{(f/8)\cdot(Re_D - 1000)\cdot Pr}{1+12.7\cdot(f/8)^{0.5}\cdot(Pr^{2/3}-1)} \qquad 3000 \leq Re_D \leq 10^6 \qquad (2\text{-}42)$$

In equation 2-42, fluid properties are initially evaluated at bulk fluid temperature. The Nusselt number is then adapted using the viscosity ratio because, in liquids, viscosity varies more than any other property with temperature (Mills, 1999). Equation 2-42 agrees with most available experimental data to within 20%, given that Re > 10 000. At lower values, turbulence is intermittent and the reliability of the correlation decreases dramatically (Mills, 1999).

Gnielinski's correlation was developed for forced flow conditions. In order to take into account the secondary flow effects present in natural circulation, a Rayleigh number correction factor, as proposed by Yang et al. (2006), was introduced:

$$Nu_D = Nu_D \cdot Ra^{-0.011} \qquad (2\text{-}43)$$

Two types of boiling are prevalent: nucleate boiling and convective boiling. These are usually treated separately, although they can coexist. As the quality increases, the contribution of the nucleate boiling decreases until eventually convective boiling is the dominant form. The first correlation that incorporates both forms was developed by Chen (as given by Whalley (1987)):

$$h = h_{NB} + h_{FC} = Sh_{FZ} + Fh_l \qquad (2\text{-}44)$$

The forced convection term (h_{FC} in equation 2-44) consists of a two phase heat transfer coefficient multiplier F that is always greater than 1, and a single phase liquid convective heat transfer coefficient (h_l) based on the liquid mass flow rate. The nucleate boiling term consists of the suppression factor S that decreases from 1 to 0 as the quality increases. The nucleate pool boiling heat transfer coefficient is calculated from the Forster-Zuber equation (Whalley, 1987):

$$h_{FZ} = \frac{0.00122\cdot\Delta T_{sat}^{0.24}\cdot\Delta P_{sat}^{0.75}\cdot c_{pl}^{0.45}\cdot\rho_l^{0.49}\cdot k_l^{0.79}}{\sigma^{0.5}\cdot\lambda^{0.24}\cdot\mu_l^{0.29}\cdot\rho_g^{0.24}} \qquad (2\text{-}45)$$

Although it is not clearly stated, it is assumed (from the worked examples contained in the text) that fluid properties in equation 2-45 are evaluated at the bulk fluid temperature (Whalley, 1987).

Collier (Carey, 1992) proposed the following relations to fit Chen's original curves (Whalley, 1987) for the suppression factor S and two phase multiplier F:

$$F = 1 \qquad \text{for} \quad X_{tt} \leq 0.1 \qquad (2\text{-}46)$$

$$F = 2.35\cdot\left(0.213 + \frac{1}{X_{tt}}\right)^{0.736} \qquad \text{for} \quad X_{tt} \geq 0.1 \qquad (2\text{-}47)$$

$$S = (1 + 2.56\times10^{-6}\cdot[Re_l\cdot F^{1.25}]^{1.17})^{-1} \qquad (2\text{-}48)$$

The single phase liquid convective heat transfer coefficient is calculated using the Dittus-Boelter equation (Mills, 1999):

$$Nu_l = 0.023 \cdot Re_l^{0.8} \cdot Pr_l^{0.4} \quad (2\text{-}49)$$

In equation 2-49: $$Re_l = \frac{G \cdot (1-x) \cdot D}{\mu_l} \quad (2\text{-}50)$$

Chen's correlation yields an average deviation from experimental data of 11%. The experimental data used to develop this correlation has a liquid inlet velocity range of 0.06 to 4.5 m/s, a pressure range of 0.55 to 34.8 bar, a quality range of 1 to 50 % by weight and a heat flux range of 44 to 2400 kW/m^2 (Collier and Thome, 1994). The correlation tends to over-predict the heat transfer coefficient in the high quality region and under-predicts it in the low quality region.

An improvement proposed by Kutateladze (Liu and Winterton, 1991), was the addition of the square of the two boiling heat transfer coefficients:

$$h^2 = (Sh_{pool})^2 + (Fh_l)^2 \quad (2\text{-}51)$$

In equation 2-51 h_{pool} is calculated from the Cooper pool boiling equation (Liu and Winterton, 1991):

$$h_{pool} = 55 \cdot p_r^{0.12} \cdot q^{2/3} \cdot (-log_{10} \cdot p_r)^{-0.55} \cdot M^{-0.5} \quad (2\text{-}52)$$

The liquid heat transfer coefficient (in equation 2-51) is given by the Dittus-Boelter equation:

$$h_l = 0.023 \cdot (k_l/D) \cdot Re_l^{0.8} \cdot Pr_l^{0.4} \quad (2\text{-}53)$$

Lui and Winterton used equation 2-51 as the departure point and made the assumption that S was a function of F and Re_l (Liu and Winterton, 1991). Using this assumption, Kutateladze's equation and experimental data:

$$F = \left(1 + x \cdot Pr_l \cdot \left[\frac{\rho_l}{\rho_v} - 1\right]\right)^{0.35} \quad (2\text{-}54)$$

$$S = (1 + 0.055 \cdot F^{0.1} \cdot Re_l^{0.16})^{-1} \quad (2\text{-}55)$$

Multiplying equation 2-51 by the square of the saturation temperature difference yields:

$$(h \cdot \Delta T_s)^2 = (Sh_{pool} \cdot \Delta T_s)^2 + (Fh_l \cdot \Delta T_s)^2 \quad (2\text{-}56)$$

Substituting equation 2-52 into equation 2-56 gives:

$$(h \cdot \Delta T_s)^2 = \left(S \cdot 55 \cdot p_r^{0.12} \cdot q^{\frac{2}{3}} \cdot (-log_{10} \cdot p_r)^{-0.55} \cdot M^{-0.5} \cdot \Delta T_s\right)^2 + (Fh_l \cdot \Delta T_s)^2$$

$$(h \cdot \Delta T_s)^2 = q^2 \quad \therefore q^2 = (Fh_l \cdot \Delta T_s)^2 + (A_p \cdot S \cdot \Delta T_s)^2 \cdot q^{4/3} \quad (2\text{-}57)$$

Where:

$$A_p = 55 \cdot p_r^{0.12} \cdot (-log_{10} \cdot p_r)^{-0.55} \cdot M^{-0.5} \quad (2\text{-}58)$$

Defining:

$$q_*^3 = \left(\frac{q}{Fh_l \cdot \Delta T_s}\right)^2 \quad (2\text{-}59)$$

and $C = \left(A_p \cdot S/Fh_l\right)^2 \cdot (Fh_l \cdot \Delta T_s)^{4/3}$ (2-60)

and incorporating equations 2-59 and 2-60 into equation 2-57:

$q_*^3 - Cq_*^2 - 1 = 0$ (2-61)

This is a standard cubic equation with one real root always greater than 1. The heat transfer coefficient can then be calculated by:

$h = Fh_l q_*^{3/2}$ (2-62)

In equation 2-62, F is the two-phase heat transfer coefficient multiplier and is always greater than 1, h_l is the single phase liquid convective heat transfer coefficient based on the liquid phase mass flow rate and q_* is function of F, S, q, p_r and ΔT_s.

Liu and Winterton's correlation yields an average deviation from experimental data of 18%. The experimental data used to develop this correlation has a liquid inlet velocity range of 12.4 to 8179.3 kg/m^{2}s, a Reynolds number range of 568.9 to 8.75 x 10^5, a quality range of 1 to 94.8 % by weight and a heat flux range of 348.9 to 2.62 x10^6 W/m^2. The correlation is valid for both horizontal and vertical two-phase flow (Liu and Winterton, 1991).

Steiner and Taborek (1992) also followed the power type addition route (see equation 2-51) for the combination of the heat transfer coefficients.

$h = \left[(F_{nbf} \cdot h_{nb,o})^n + (F_{tp} \cdot h_l)^n\right]^{1/n}$ (2-63)

In this equation, F_{nbf} is a correction factor that compensates for the differences in pool and flow boiling and $h_{nb,o}$ is the nucleate pool boiling coefficient based on normalised conditions. F_{tp} is the two-phase multiplier and h_l is the liquid phase heat transfer coefficient calculated from equation 2-53. The value of the exponent n determines the transition between the two types of boiling. Regression analysis of their data points showed that n = 3 (Steiner and Taborek, 1992).

The two phase multiplier $F_{tp,}$ is given for qualities less than 0.6 by:

$F_{tp} = \left[(1-x)^{1.5} + 1.9 \cdot x^{0.6} \cdot \left(\frac{\rho_l}{\rho_g}\right)^{0.35}\right]^{1.1}$ (2-64)

The nucleate boiling correction factor, F_{nbf}, is a function of pressure, heat flux, tube diameter, surface roughness and molecular weight:

$F_{nbf} = F_{pf} + \left[\frac{\dot{q}}{\dot{q}_{of}}\right]^{nf(p_r)} + F(d) + F(R_a) + F(M)$ (2-65)

Where: $F_{pf} = \left(2.816 \cdot p_r^{0.45} + \left[3.4 + \frac{1.7}{1-p_r^7}\right] \cdot p_r^{3.7}\right)$ (2-66)

$nf(p_r) = 0.8 - 0.1\exp(1.75 \cdot p_r)$ (2-67)

$F(d) = \left(\frac{D}{0.01}\right)^{-0.4}$ (2-68)

$F(R_a) = 1$ (2-69)

$F(M) = 0.72$ (2-70)

The normalized nucleate boiling heat transfer coefficient, $h_{nb,o}$, for water, is given as 25580 W/m^{2}K (Mills, 1999).

The Steiner-Taborek correlation is based on an extensive data base and is considered by Collier and Thome (1994) as the most accurate vertical tube boiling correlation currently available. The lowest mass flux that this correlation is valid for is 28 kg/m^{2}s.

For internal flow condensation, various correlations have been developed from the assumption that the flow regime is annular. This may lead to some inaccuracy at the point where the condensation process ends and where other flow regimes take over. Soliman et al. (1968) noted the importance of the shear stresses in heat transfer across the liquid film in annular flow, developing the following correlation:

$$h = 0.036 \cdot \frac{k_l \cdot \rho_l^{0.5}}{\mu_l} \cdot Pr_l^{0.65} \cdot \tau_w^{0.5} \tag{2-71}$$

The τ_w term in equation 2-71, consists of the shear terms due to friction, gravity and frictional pressure gradient in the fluid:

$$\tau_w = \tau_i + \tau_z + \tau_a \tag{2-72}$$

$$\tau_i = \frac{D}{4} \cdot \left(-\frac{dP}{dz}\right)_F, \ \left(-\frac{dP}{dz}\right)_F = \phi_g^2 \cdot \left(-\frac{dP}{dz}\right)_v, \qquad \phi_g^2 = 1 + 2.85 \cdot X_{tt}^{0.523} \tag{2-73}$$

$$\tau_z = \frac{D}{4} \cdot (1-\alpha) \cdot (\rho_l - \rho_v) \cdot g \cdot sin\theta, \quad \alpha = \left[1 + \left(\frac{1-x}{x}\right) \cdot \left(\frac{\rho_v}{\rho_l}\right)^{2/3}\right]^{-1} \tag{2-74}$$

$$\tau_a = \frac{D}{4} \cdot \left(\frac{G^2}{\rho_v}\right) \cdot \left(\frac{dx}{dz}\right) \cdot \sum_{n=1}^{5} a_n \cdot \left(\frac{\rho_v}{\rho_l}\right)^{n/3} \tag{2-75}$$

$$a_1 = 2x - 1 - \beta \cdot x \tag{2-76}$$

$$a_2 = 2 \cdot (1-x) \tag{2-77}$$

$$a_3 = 2 \cdot (1 - x - \beta + \beta \cdot x) \tag{2-78}$$

$$a_4 = x^{-1} - 3 + 2 \cdot x \tag{2-79}$$

$$a_5 = \beta \cdot (2 - x^{-1} - x) \tag{2-80}$$

For flow in round tubes and a Reynolds number greater than 2000, the flow is considered turbulent and the value of β is 1.25; for a Reynolds number less than 2000, the flow is considered as laminar and the value of β is 2.0.

Traviss et al. (1973) proposed the following correlation:

$$Nu = \frac{0.15 \cdot Pr_l \cdot Re_l^{0.9}}{F_T} \cdot \left[\frac{1}{X_{tt}} + \frac{2.85}{X_{tt}^{0.476}}\right] \tag{2-81}$$

X_{tt} (in equation 2-81) is the turbulent-turbulent Martinelli parameter and F_T is a function of Pr_l and Re_l:

$$\begin{aligned} F_T &= 5 \cdot Pr_l + 5 \cdot \ln(1 + 5 \cdot Pr_l) + 2.5 \cdot \ln\left(0.0031 \cdot Re_l^{0.812}\right) && \text{for } Re_l > 1125 \\ &= 5 \cdot Pr_l + 5 \cdot \ln(1 + Pr_l \cdot [0.0964 \cdot Re_l^{0.585} - 1]) && \text{for } 50 < Re_l < 1125 \\ &= 0.707 \cdot Pr_l \cdot Re_l^{0.5} && \text{for } Re_l < 50 \end{aligned} \tag{2-82}$$

$$Re_l = \frac{G \cdot (1-x) \cdot D}{\mu_l} \tag{2-83}$$

A correlation based on empirical data for convective (or flow) condensation in round tubes proposed by Shah (1989), is given by:

$$\frac{h}{h_{lo}} = (1-x)^{0.8} + \frac{3.8 \cdot x^{0.76} \cdot (1-x)^{0.04}}{P_r^{0.38}} \quad (2\text{-}84)$$

h_{lo} (in equation 2-84) is calculated using the Dittus Boelter equation:

$$h_{lo} = 0.023 \cdot \left(\frac{k_{lo}}{D}\right) \cdot Re_{lo}^{0.8} \cdot Pr_{lo}^{0.4} \quad (2\text{-}85)$$

Shah (1989) recommends this correlation for $11 \leq G \leq 211$ kg/m^{2}s, $0 \leq x \leq 1$ and $1 \leq Pr \leq 13$.

The three correlations presented above are primarily for horizontal flow. Chen et al. (1987) developed a correlation for annular flow condensation in vertical tubes based on analytical and theoretical results. This correlation takes the form:

$$Nu_x = \left[\left(0.31 \cdot Re_x^{-1.32} + \frac{Re_x^{2.4} \cdot Pr_l^{3.9}}{2.37 \times 10^{14}}\right)^{1/3} + \frac{A_D \cdot Pr_l^{1.3}}{771.6} \cdot (Re_{ter} - Re_x)^{1.4} \cdot Re_x^{0.4}\right]^{1/2} \quad (2\text{-}86)$$

where

$$Nu_x = \frac{h \cdot v_l^{2/3}}{k_l \cdot g^{1/3}} \quad (2\text{-}87)$$

$$Re_x = \frac{G \cdot (1-x) \cdot D}{\mu_l} \quad (2\text{-}88)$$

$$A_D = \frac{0.252 \cdot \mu_l^{1.177} \cdot \mu_v^{0.156}}{D^2 \cdot g^{2/3} \cdot \rho_l^{0.553} \cdot \rho_v^{0.78}} \quad (2\text{-}89)$$

$$Re_{ter} = \frac{G \cdot D}{\mu_l} \quad (2\text{-}90)$$

2.4.1 Summary

From the above literature, four pertinent heat transfer coefficient correlations were identified for specific flow conditions in the numerical simulation. For single phase laminar flow, the Collier correlation will be used (Collier & Thome, 1994):

$$Nu_D = 0.17 Re_D^{0.33} Pr^{0.43} \left(\frac{Pr}{Pr_w}\right)^{0.25} Gr^{0.1} \qquad Re_D \leq 2000 \quad (2\text{-}40)$$

For single phase turbulent flow, the Gnielinski correlation (Mills, 1999) will be used:

$$Nu_D = \frac{(f/8) \cdot (Re_D - 1000) \cdot Pr}{1 + 12.7 \cdot (f/8)^{0.5} \cdot (Pr^{2/3} - 1)} \qquad 3000 \leq Re_D \leq 10^6 \quad (2\text{-}41)$$

For two-phase boiling Chen's correlation (as given by Whalley, 1987) will be used:

$$h = h_{NB} + h_{FC} = Sh_{FZ} + Fh_l \quad (2\text{-}91)$$

Finally for vertical two-phase condensation, the correlation developed by Traviss et al. (1973) will be used (Traviss, Rohsenow, & Baron, 1973):

$$Nu = \frac{0.15 \cdot Pr_l \cdot Re_l^{0.9}}{F_T} \cdot \left[\frac{1}{X_{tt}} + \frac{2.85}{X_{tt}^{0.476}}\right] \quad (2\text{-}92)$$

3 MATHEMATICAL MODELLING OF NATURAL CIRCULATION

3.1 Simplifying Assumptions

To develop a mathematical model, several assumptions have to be made, the most important of these being: the thermodynamic process is quasi-static; compressibility effects due to heating or cooling of the liquid and vapour phases are negligible; and that the flow is one-dimensional.

Çengel defines a quasi-static process as one in which the system proceeds through a sequence of states that remain infinitesimally close to equilibrium (Cengel & Boles, 2002). In other words, the process occurs sufficiently slowly to allow the system to adjust internally so that no one thermodynamic property changes faster than another. This assumption allows for a transient analysis to be modelled by a steady-state analysis at each time step. Its applicability for this thesis is due to the high speed at which pressure waves propagate through the system, effectively changing the pressure instantaneously throughout, bringing it instantaneously to a new state at each time-step.

According to White (2006), a flow is considered to be incompressible if the divergence of the velocity is zero. In other words, flow can be seen as incompressible if the change in mass along the flow axis ($\frac{\partial}{\partial z}\{\rho_k v_k \alpha_k\}$) is zero. This usually assumes constant density, but in this case, the driving force behind the circulatory flow is the buoyancy force, which is temperature and thus density dependent. Thus pseudo-incompressibility (also known as low Mach-number flow), coupled with the Boussinesq approximation, is applicable. This is often used in natural circulation simulation in nuclear reactors. (Chan & Nakayama, 1990; Nayak et. al., 1998; Xinian et. al., 2001; van de Graaf and van der Hagen, 1994).

In essence, the Boussinesq approximation states that the density variation with consecutive time-steps is negligible, except in the gravity driven terms where density is a function of temperature only. This approximation neglects sound wave propagation because they are driven through in-fluid density variations. The pseudo-incompressibility constraint allows for the removal of acoustic waves if the flow remains below a Mach number limit (White (2006) recommends 0.3). For any incompressibility flow assumptions to be valid, the pressure deviation must be very small when compared to the pressure base state. In this case, the pressure variation throughout the loop is insignificant compared with the system pressure which remains in the vicinity of 1.5 atmospheres.

The RCCS was modelled as a one-dimensional system since this is normal practice when simulating natural circulation in nuclear reactors (Reyes, 2007), using the homogenous flow model identified in section 2.3.2.1. Figure 3-1 shows the discretised system: the thermosyphon, evaporator section, condenser section, and expansion tank divided into control volumes.

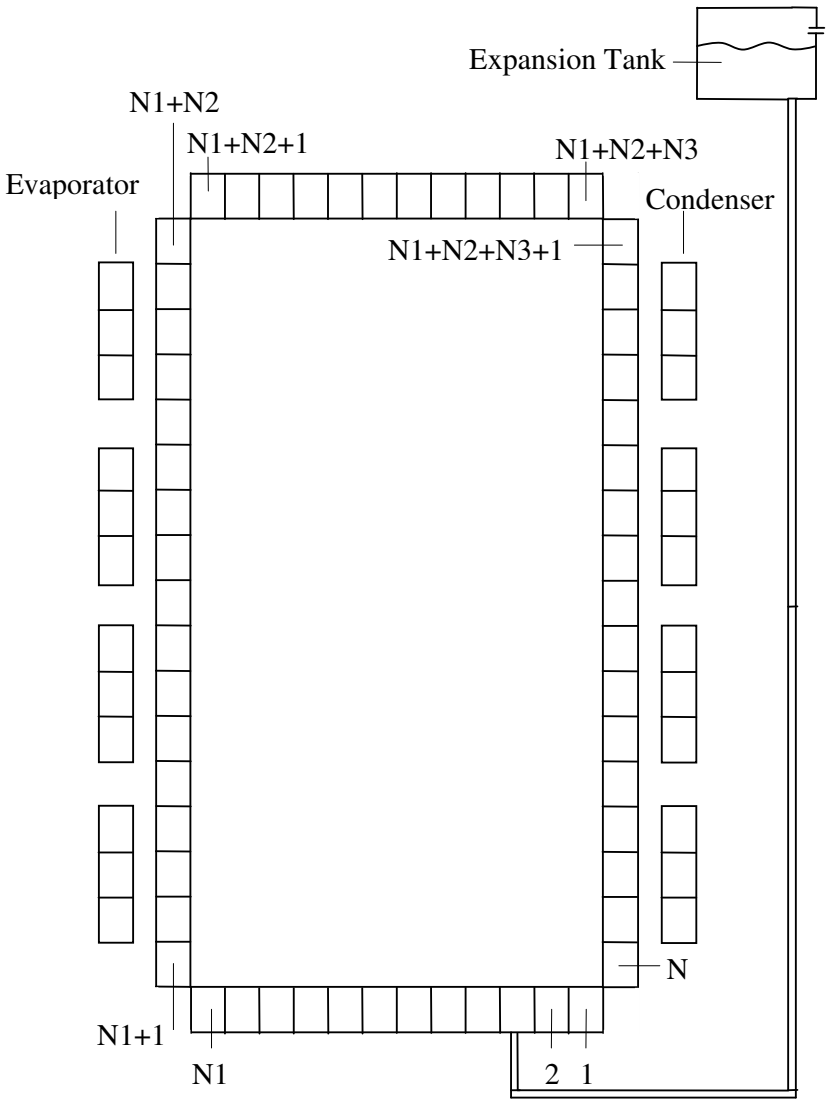

Figure 3-1: The one dimensional discretised theoretical model of the RCCS

3.2 Formulation of the Differential Equations

This section shows how the conservation equations developed in section 2.3.2.1 are applied to each of the control volumes in the discretised system, in order to develop differential equations for the computer simulation. The integration scheme selected is an explicit-type marching process. All partial derivatives are replaced by their forward finite difference approximations, a solution is then found explicitly at a single value of time in terms of the solution at earlier values of time (Farlow, 1993). Unless otherwise stated, all properties are evaluated at the previous time step. Convergence of the integration process is discussed in detail in Appendix C.5.

3.2.1 Working Fluid

Figure 3-2 shows the energy flow across the boundaries of a general working fluid control volume in the discretised system.

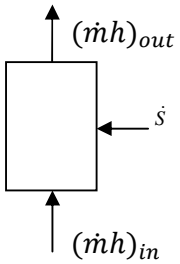

Figure 3-2: Conservation of energy for working fluid control volume

Applying equation 2-30 yields:

$$\frac{\partial U_m}{\partial t} + \frac{\partial}{\partial z}\{\dot{m}_m\langle h_m\rangle\} = \dot{S} \tag{3-1}$$

By definition (Çengel, 2003):

$$U = mC_vT \tag{3-2}$$

Using equation 3-2, equation 3-1 can be reduced as follows (assuming that the mixture mass is constant across the control volume):

$$\frac{\partial m_m C_{v,m} T_m}{\partial t} = \dot{S} - \dot{m}_m(h_{m,out} - h_{m,in}) \tag{3-3}$$

Using the product rule (Stewart, 1999), the first term in equation 3-3 can be defined:

$$\begin{aligned}\frac{\partial m_m C_{v,m} T_m}{\partial t} &= m_m \frac{\partial C_{v,m} T_m}{\partial t} + C_{v,m}\frac{\partial m_m T_m}{\partial t} + T_m \frac{\partial m_m C_{v,m}}{\partial t} \\ &= m_m\left(C_{v,m}\frac{\partial T_m}{\partial t} + T_m\frac{\partial C_{v,m}}{\partial t}\right) + C_{v,m}\left(m_m\frac{\partial T_m}{\partial t} + T_m\frac{\partial m_m}{\partial t}\right) + T_m\left(m_m\frac{\partial C_{v,m}}{\partial t} + C_{v,m}\frac{\partial m_m}{\partial t}\right) \\ &= \frac{\partial T_m}{\partial t}\left(2m_m C_{v,m}\right) + \frac{\partial C_{v,m}}{\partial t}(2m_m T_m) + \frac{\partial m_m}{\partial t}\left(2C_{v,m}T_m\right)\end{aligned} \tag{3-4}$$

Substituting this into equation 3-3:

$$\begin{aligned}&\frac{\partial T_m}{\partial t}\left(2m_m C_{v,m}\right) = \dot{S} - \dot{m}_m(h_{m,out} - h_{m,in}) - \frac{\partial C_{v,m}}{\partial t}(2m_m T_m) - \frac{\partial m_m}{\partial t}\left(2C_{v,m}T_m\right) \\ &\therefore \frac{\partial T_m}{\partial t} = \frac{\dot{S}}{2m_m C_{v,m}} - \frac{\dot{m}_m}{2m_m C_{v,m}}(h_{m,out} - h_{m,in}) - \frac{\partial C_{v,m}}{\partial t}\left(\frac{T_m}{C_{v,m}}\right) - \frac{\partial m_m}{\partial t}\left(\frac{T_m}{m_m}\right)\end{aligned} \tag{3-5}$$

With the quasi-static assumption, equation 3-5 can be written as a difference equation:

$$\begin{aligned}&\frac{\Delta T_m}{\Delta t} = \frac{\dot{S}}{2m_m C_{v,m}} - \frac{\dot{m}_m}{2m_m C_{v,m}}(h_{m,out} - h_{m,in}) - \frac{\Delta C_{v,m}}{\Delta t}\left(\frac{T_m}{C_{v,m}}\right) - \frac{\Delta m_m}{\Delta t}\left(\frac{T_m}{m_m}\right) \\ &\therefore \Delta T_m = \frac{\Delta t\dot{S}}{2m_m C_{v,m}} - \frac{\Delta t\dot{m}_m}{2m_m C_{v,m}}(h_{m,out} - h_{m,in}) - \Delta t\frac{\Delta C_{v,m}}{\Delta t}\left(\frac{T_m}{C_{v,m}}\right) - \Delta t\frac{\Delta m_m}{\Delta t}\left(\frac{T_m}{m_m}\right) \\ &T_m^{t+\Delta t} = T_m^t + \frac{\Delta t\dot{S}}{2m_m C_{v,m}} - \frac{\Delta t\dot{m}_m}{2m_m C_{v,m}}\left(h_{m,out} - h_{m,in}\right) - \Delta t\frac{\Delta C_{v,m}}{\Delta t}\left(\frac{T_m}{C_{v,m}}\right) - \Delta t\frac{\Delta m_m}{\Delta t}\left(\frac{T_m}{m_m}\right)\end{aligned} \tag{3-6}$$

It should be noted that, in the above equations, $\dot{S}$ represents the heat transferred across the control volume boundaries. In equation 2-30, the heat transfer term includes a change in density and sum of shear forces term. The assumption of incompressibility eliminates the change in density. It is also assumed that the energy added to the system due to the shear forces is negligible when compared to the heat transferred from the heating elements. In this analysis, axial conduction is ignored.

Equation 3-6 yields the new temperature which allows the calculation of the internal energy and quality at each time-step (Çengel, 2003):

If $T_m^{t+\Delta t} < T_{sat}$ then $u_m^{t+\Delta t} = C_{v,m} T_m^{t+\Delta t}$ and $x^{t+\Delta t} = 0$ (3-7)

If $T_m^{t+\Delta t} > T_{sat}$ then $T_m^{t+\Delta t} = T_{sat}$, $u_m^{t+\Delta t} = C_{v,m} T_m^{t+\Delta t}$ and $x^{t+\Delta t} = \frac{u_m^{t+\Delta t} - u_f^{t+\Delta t}}{u_{fg}^{t+\Delta t}}$ (3-8)

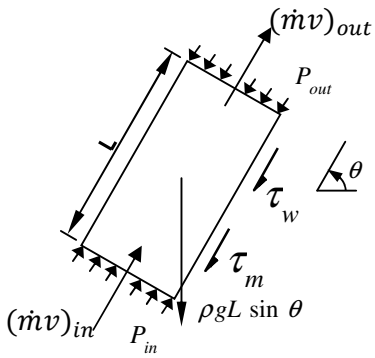

Figure 3-3: Conservation of momentum for working fluid control volume

Figure 3-3 shows forces acting on the boundaries of the working fluid control volume that are taken into consideration when applying the momentum conservation equation (equation 2-24):

$$\frac{\partial(m_m v_m)}{\partial t} + \frac{\partial(\dot{m}_m v_m)}{\partial z} = -A_x \frac{\partial P}{\partial z} - \tau_w A_z - \tau_m A_z - \bar{\rho} g L A_x sin\theta \quad (3\text{-}9)$$

Assuming a constant mass flow rate across the control volume and using the definitions for mass flow rate (Çengel, 2003):

$$\dot{m} = \rho v A \qquad \therefore v_m = \frac{\dot{m}}{\bar{\rho} A_x} \quad (3\text{-}10)$$

Substituting equation 3-10 into equation 3-9:

$$\frac{\partial(m_m v_m)}{\partial t} + \frac{\partial}{\partial z}\left(\frac{\dot{m}_m^2}{\bar{\rho} A_x}\right) = -A_x \frac{\partial P}{\partial z} - \tau_w A_z - \tau_m A_z - \bar{\rho} g L A_x sin\theta \quad (3\text{-}11)$$

Dividing equation 3-11 by A_x:

$$\frac{1}{A_x}\frac{\partial(m_m v_m)}{\partial t} + \frac{\partial}{\partial z}\left(\frac{\dot{m}_m^2}{\bar{\rho} A_x^2}\right) = -\frac{\partial P}{\partial z} - \tau_w \frac{A_z}{A_x} - \tau_m \frac{A_z}{A_x} - \bar{\rho} g L sin\theta \quad (3\text{-}12)$$

The first term in equation 3-12 is defined using the product rule (Stewart, 1999):

$$\frac{\partial(m_m v_m)}{\partial t} = m_m \frac{\partial v_m}{\partial t} + v_m \frac{\partial m_m}{\partial t} \quad (3\text{-}13)$$

Substituting equation 3-13 into equation 3-12:

$$\frac{1}{A_x}\left(m_m\frac{\partial v_m}{\partial t}+v_m\frac{\partial m_m}{\partial t}\right)+\frac{\dot{m}_m^2}{A_x^2}\frac{\partial}{\partial z}\left(\frac{1}{\bar{\rho}}\right)=-\frac{\partial P}{\partial z}-\tau_w\frac{A_z}{A_x}-\tau_m\frac{A_z}{A_x}-\bar{\rho}gLsin\theta$$

$$\therefore \frac{m_m}{A_x}\frac{\partial v_m}{\partial t}=-\frac{\partial P}{\partial z}-\tau_w\frac{A_z}{A_x}-\tau_m\frac{A_z}{A_x}-\bar{\rho}gLsin\theta-\frac{v_m}{A_x}\frac{\partial m_m}{\partial t}-\frac{\dot{m}_m^2}{A_x^2}\frac{\partial}{\partial z}\left(\frac{1}{\bar{\rho}}\right)$$

$$\therefore \frac{\partial v_m}{\partial t}=-\frac{A_x}{m_m}\frac{\partial P}{\partial z}-\tau_w\frac{A_z}{m_m}-\tau_m\frac{A_z}{m_m}-\frac{\bar{\rho}gLA_x}{m_m}sin\theta-\frac{\dot{m}}{m_m\bar{\rho}A_x}\frac{\partial m_m}{\partial t}-\frac{\dot{m}_m^2}{m_mA_x}\frac{\partial}{\partial z}\left(\frac{1}{\bar{\rho}}\right) \quad (3\text{-}14)$$

Using the definitions for mass (Çengel, 2003):

$$m=\rho V \qquad \therefore m_m=\bar{\rho}A_xL \quad (3\text{-}15)$$

Substituting equation 3-15 into equation 3-14:

$$\frac{\partial v_m}{\partial t}=-\frac{1}{\bar{\rho}L}\frac{\partial P}{\partial z}-\tau_w\frac{A_z}{\bar{\rho}A_xL}-\tau_m\frac{A_z}{\bar{\rho}A_xL}-gsin\theta-\frac{\dot{m}}{\bar{\rho}^2A_xL}\frac{\partial\bar{\rho}}{\partial t}-\frac{\dot{m}_m^2}{\bar{\rho}\,{A_x}^2L}\frac{\partial}{\partial z}\left(\frac{1}{\bar{\rho}}\right) \quad (3\text{-}16)$$

In the momentum conservation equation the wall shear stress and minor flow losses can be calculated using the definitions (Crowe, Elger, & Roberson, 2001):

$$\tau_w=\frac{1}{2}\frac{f}{4}\bar{\rho}v_m^2 \quad (3\text{-}17)$$

$$\tau_m=\frac{1}{2}k\bar{\rho}v_m^2 \quad (3\text{-}18)$$

Applying the above equations, as well as equation 3-10 to equation 3-16 yields:

$$\frac{\partial v_m}{\partial t}=-\frac{1}{\bar{\rho}L}\frac{\partial P}{\partial z}-\frac{f\dot{m}^2A_z}{8\bar{\rho}^2{A_x}^3L}-\frac{k\dot{m}^2A_z}{2\bar{\rho}^2{A_x}^3L}-gsin\theta-\frac{\dot{m}}{\bar{\rho}^2A_xL}\frac{\partial\bar{\rho}}{\partial t}-\frac{\dot{m}_m^2}{\bar{\rho}\,{A_x}^2L}\frac{\partial}{\partial z}\left(\frac{1}{\bar{\rho}}\right) \quad (3\text{-}19)$$

Integrating around the loop cancels out the positional pressure and density variations, and applying the quasi-static assumption, equation 3-19 can be written as a difference equation:

$$v_m^{t+\Delta t}=v_m^t+\Delta t\left(-\sum\left(\frac{f}{4}+k\right)\frac{\dot{m}^2A_z}{2\bar{\rho}^2{A_x}^3L}-\sum gsin\theta\ -\frac{\bar{\rho}^t-\bar{\rho}^{t-\Delta t}}{\Delta t}\sum\frac{\dot{m}}{\bar{\rho}^2A_xL}\right) \quad (3\text{-}20)$$

Equation 3-20 yields the new velocity, which allows for the calculation of the mass flow rate at each time-step using equation 3-10. Note that mass flow rate is defined as the mass leaving the control volume in a given time step.

In order to determine how much mass is transferred to or from the expansion tank, it is necessary to apply the mass conservation equation (equation 2-20), as shown in Figure 3-4:

$$\frac{\partial m_m}{\partial t}=\dot{m}_{in}-\dot{m}_{out} \quad (3\text{-}21)$$

Writing equation 3-21 as a difference equation yields:

$${m_m}^{t+\Delta t}={m_m}^t+\Delta t\left(\dot{m}_{t,i-1}-\dot{m}_{t,i}\right) \quad (3\text{-}22)$$

Equation 3-22 yields the new mixture mass using the new mass flow rate of the current and previous control volume. This, in conjunction with the new quality calculated using equations 3-7 and 3-8, allows for the calculation of the new phase masses by using the following identities (Whalley, 1987):

$$m_v=xm_m \quad (3\text{-}23)$$

$$m_l=(1-x)m_m \quad (3\text{-}24)$$

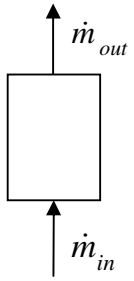

Figure 3-4: Conservation of mass for working fluid control volume

Using the definition for mass (equation 3-15) and a correlation for fluid density at the new temperature, the new phase volumes for can be calculated:

$$V_k = \frac{m_k}{\rho_k} \tag{3-25}$$

The new mixture volume can now be calculated:

$$V_m = V_l + V_v \tag{3-26}$$

But the control volume retains a constant volume. The change in mixture volume is compensated for by the expansion tank. In other words, if the new volume is greater than that of the control volume, the excess liquid is forced into the expansion tank (it is assumed that this takes place instantaneously to simplify calculation). If the new volume is less than that of the control volume, the deficit is made up by content from the expansion tank.

$$dV = V_m^{new} - V_{cv} \tag{3-27}$$

$$V_{l,cv} = V_l^{new} - dV \tag{3-28}$$

$$V_{et}^{new} = V_{et}^{old} + dV \tag{3-29}$$

3.3 Numerical Considerations

In order to generate solutions with the mathematical model outlined in section 3.2.1, correlations for the friction factor, heat transfer coefficient, void fraction and two-phase frictional multiplier must be identified. Due to the lack of relevant natural flow correlations, most of the correlations used are for forced flow which introduces room for over- or under-prediction of the model as the working fluid flow might not be fully developed at all times.

3.3.1 Friction Factor

Crowe, Elger & Roberson (2001) give correlations for the laminar and turbulent friction factor for flow in conduits. The resistance coefficient for laminar, fully developed flow (smooth surface) is given by:

$$f = \frac{64}{Re_D} \qquad Re_D > 2000 \tag{3-30}$$

For turbulent flow, analytical and empirical results using smooth pipes give an approximate correlation for the friction factor:

$$\frac{1}{\sqrt{f}} = 2\log\left(Re_D\sqrt{f}\right) - 0.8 \qquad Re_D > 3000 \tag{3-31}$$

An explicit equation for the friction factor was developed by Crowe et al. (2001) that differs less than 3% from the Moody diagram predictions for $4 \times 10^3 < Re_D < 10^8$ and $10^{-5} < \frac{k_s}{D} < 2 \times 10^{-2}$.

$$f = \frac{0.25}{\left[log_{10}\left(\frac{k_S}{3.7D}\right) + \frac{5.74}{Re_D^{0.9}}\right]^2} \tag{3-32}$$

3.3.2 Heat Transfer Correlations

From the literature study, four pertinent heat transfer coefficient correlations were identified. For convenience they are briefly repeated here. For single phase laminar flow, the Collier correlation will be used (Collier & Thome, 1994):

$$Nu_D = 0.17 Re_D^{0.33} Pr^{0.43} \left(\frac{Pr}{Pr_w}\right)^{0.25} Gr^{0.1} \qquad Re_D \leq 2000 \tag{2-40}$$

For single phase turbulent flow, the Gnielinski correlation (Mills, 1999) is used:

$$Nu_D = \frac{(f/8)\cdot(Re_D - 1000)\cdot Pr}{1 + 12.7\cdot(f/8)^{0.5}\cdot(Pr^{2/3} - 1)} \qquad 3000 \leq Re_D \leq 10^6 \tag{2-41}$$

For two-phase boiling Chen's correlation (as given by Whalley, 1987) is used:

$$h = h_{NB} + h_{FC} = Sh_{FZ} + Fh_l \tag{2-33}$$

Finally for vertical two-phase condensation, the correlation developed by Traviss et al. (1973) will be used (Traviss, Rohsenow, & Baron, 1973):

$$\frac{h}{h_{lo}} = (1 - x)^{0.8} + \frac{3.8\cdot x^{0.76}\cdot(1-x)^{0.04}}{P_r^{0.38}} \tag{2-83}$$

3.3.3 Void Fraction

The void fraction is defined as the time-averaged volumetric fraction of vapour in the two-phase mixture. The general equation is given as (Mills, 1999):

$$\alpha = \frac{1}{1 + \left(S\frac{1-x}{x}\frac{\rho_g}{\rho_l}\right)} \qquad \text{where} \qquad S = \frac{v_g}{v_l} \tag{3-34}$$

Void fraction models use different values and correlations for the slip ratio. The homogenous flow model assumes that the two fluid phases are well mixed and travelling at the same velocity, thus the slip ratio is one. The separated flow model requires a slip ratio greater than one, i.e. the liquid phase velocity is less than the vapour phase velocity (Mills, 1999).

Saha (2009) recommends the commonly used Modified Smith model:

$$S = K + (1 + K)\left\{\frac{\frac{\rho_l}{\rho_v} + K\left(\frac{1}{x} - 1\right)}{1 + K\left(\frac{1}{x} - 1\right)}\right\}^{0.5} \tag{3-35}$$

In equation 3-35:

$$K = 0.95\tanh(5x) + 0.05 \quad (3\text{-}36)$$

3.3.4 Two Phase Multiplier

In two-phase flow, the pressure drop due to friction is approximated using well established, single phase flow, frictional pressure drop equations and a two-phase multiplier correlation. The two-phase flow correlation is defined as the ratio between the two-phase frictional pressure drop and the frictional pressure drop for flow with mass flow rates corresponding to mixture or individual phase flow rates. The most common of these definitions is the liquid only two-phase multiplier. Saha (2009) recommends the Martinelli-Nelson correlation for water:

$$\phi_{LO}^2 = (1-x)^{1.75}\phi_L^2 \quad (3\text{-}37)$$

In equation 3-37, ϕ_L^2 refers to the Lockhart-Mertinelli correlation for the two-phase multiplier for liquid phase friction and is given by (Carey, 1992):

$$\phi_L^2 = \left(1 + \frac{20}{\mathrm{X}} + \frac{1}{\mathrm{X}^2}\right)^{0.5} \quad (3\text{-}38)$$

X in the above equation is the Martinelli parameter given by the following correlation, assuming both phases are turbulent (Carey, 1992):

$$X_{tt} = \left(\frac{1-x}{x}\right)^{0.9}\left(\frac{\rho_v}{\rho_l}\right)^{0.5}\left(\frac{\mu_l}{\mu_v}\right)^{0.1} \quad (3\text{-}39)$$

3.4 Solution Procedure

A computer program was written using PowerBasic Compiler 9.0 (copyright 2008). Results from the computer program were imported into Microsoft Excel which was used to generate graphs.

The solution procedure proceeds stepwise as follows:

1) Define constants and material properties taken as constant
2) Define geometry
3) Apply initial conditions
   a. Initial control volume temperature and mass fraction
   b. Initial control volume density and mass
   c. Initial control volume interface pressures
   d. Initial average pressure and saturation temperature
   e. Initial cooling water temperatures and masses
   f. Initial expansion tank mass
   g. Net initial heat flow to each control volume
4) Calculate initial net heat transfer to control volume
5) Calculate net heat transfer to control volume
6) Calculate the new control volume temperature using equation 3-6
7) Using the new temperature, calculate the new void fraction using equation 3-25
8) Calculate the new mass fraction using equations 3-7 and 3-8

9) Using the new void fraction, calculate the new mixture density and mass
10) Calculate the two-phase multiplier using equation 3-28
11) Calculate the new coolant temperatures in the condenser
12) Calculate the new expansion tank temperature
13) Using equation 3-20, calculate the new mixture velocity
14) Calculate the new mass flow rate using equation 3-10
15) Calculate the new fluid pressure drop and use this knowledge to determine the new interface pressures and average control volume pressures
16) Calculate the new saturation temperature
17) Calculate the stability criteria, check the time interval and adjust if necessary
18) Apply mass conservation equation to determine the amount of mass transferred to or from expansion tank
19) Write output data to result file
20) Repeat steps 4 to 18 until final time step is attained

In order to verify the correct implementation of the equations developed in section 3.2 step by step hand calculations were performed. Sample calculations for a single iteration are presented in Appendix C.6.

4 EXPERIMENTAL MODEL

This section describes the thermosyphon loop designed and built to obtain experimental data. The experimental setup is given, with specific reference to thermosyphon geometry, the materials used for the separate components, the sensors used to capture data and the data acquisition system. The procedure followed during experimentation is also discussed. Design specification and limited design calculations are given in Appendix D.

4.1 Introduction

As described in Section 1, the objective of the experimental model is to simulate an axially symmetric section of the RCCS by making use of a one-third-height scale model, consisting of a single natural circulation loop heated by electrical heaters and cooled with pipe-in-pipe heat exchangers to validate the theoretical model. Before design of the experimental model commenced, two operating modes were identified. Single phase flow, the first of the operating modes, does not allow boiling in the loop. This mode is popular with passive safety systems as it eliminates two-phase instabilities. The second operating mode is the single to two-phase operating mode. Here operation starts in the single phase mode. Heat added to the working fluid by the heating elements eventually causes the fluid to boil allowing both vapour and liquid phases to coexist in the system. Both of the operating modes mentioned require the use of an expansion tank to allow for a constant pressure process.

4.2 Experimental Setup

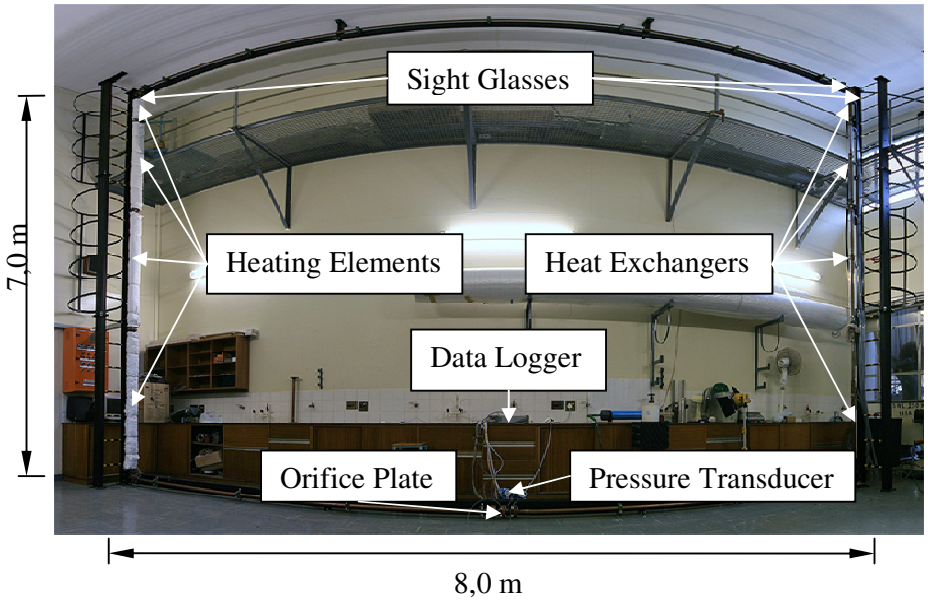

Figure 4-1: Experimental setup with element covers removed (taken with a wide angle lens)

Figure 4-1 shows the experimental setup, the orifice plate, heat exchangers, heating elements and pressure transducers. Note that the loop is rectangular in one plane. The apparent distortion is due to the wide angle camera lens. In order to be comparable to theoretical data, temperatures were measured in the heating elements, working fluid and cooling fluid, as shown in Figure 4-2: Thermosyphon loop. The following paragraphs describe the geometry and materials, sensors, data acquisition and procedures followed to obtain the results.

4.2.1 Geometry and Materials

Figure 4-2 shows a schematic representation of the thermosyphon loop. The loop is constructed from 35 mm OD, 32 mm ID copper tubes and measures 8 m wide and 7 m in height. Ruppersberg (2007) identified that material surface properties play a major role in experimentation. The parameters he found were average values which do not necessarily represent the same conditions of the experiment. Copper was used, not only because of its high thermal conductivity, but also because of the extensive knowledge of heat transfer and material properties available in literature to overcome this problem.

To connect the various sections of the loop, standard 90˚ elbows were used and ISO 7005-3:1988 standard copper alloy flanges were designed and manufactured (ISO, 1988). The working fluid (water) for the natural circulation loop was chosen based on cost, availability and abundance of fluid, availability of heat transfer properties for the fluid, ease of use with specific regards to identifying and stopping leaks, sealing, filling and emptying the loop, etc.

In previous studies, flow oscillations were identified during experimenting (Ruppersberg, 2007; Verwey, 2007). It was therefore decided that a flow meter, capable of bi-directional flow measurement, is necessary, resulting in the design and manufacture of a British standard, unbevelled orifice plate with a β-ratio of 0.3125. Adhering to the standard, a straight length greater than 12 diameters precede the inlet (in both directions) to eliminate swirl and eddies induced in the elbows and flange tappings (BSI, 1981).

The evaporator section of the thermosyphon consists of four heated sections. Three of the sections consist of a copper pipe, 2 m in length, onto which copper rectangular fins, 1.85 m in length, 50 mm wide and 10 mm thick were welded along the length. Custom made heating elements with a resistance of 35.0 Ω, each capable of providing 1500 W of heat, are attached to each fin. B64-25 Ceramic fibre (7.32 x 610 x 25 mm) insulation material surrounds the assembly. The fibre has a density of 64 kg/m^3 and a thermal conductivity of 0.07 W/m K (Thermal Ceramics Pty Ltd). The fourth, and highest heating section is identical in construction to the other three but is only 650 mm in length and the heating elements have a resistance of 105 Ω, capable of providing 500 W of heat each. This gives the evaporator section a total electrical yield of 10 kW (Loubser, 2008). Figure 4-3 shows a heating element and a typical finned copper pipe.

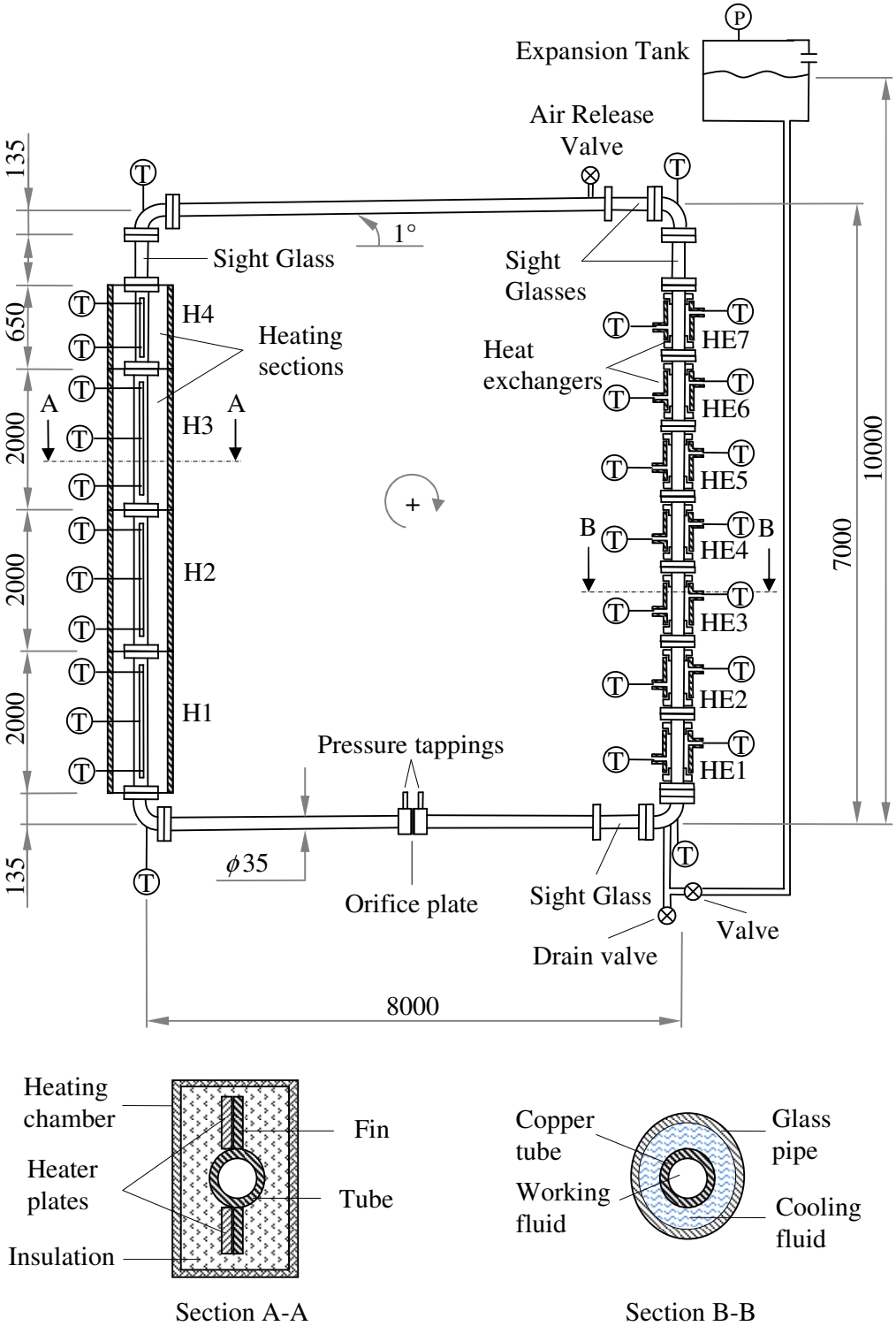

Figure 4-2: Thermosyphon loop

(a)

(b)

Figure 4-3: a) Heating element and b) finned copper pipe

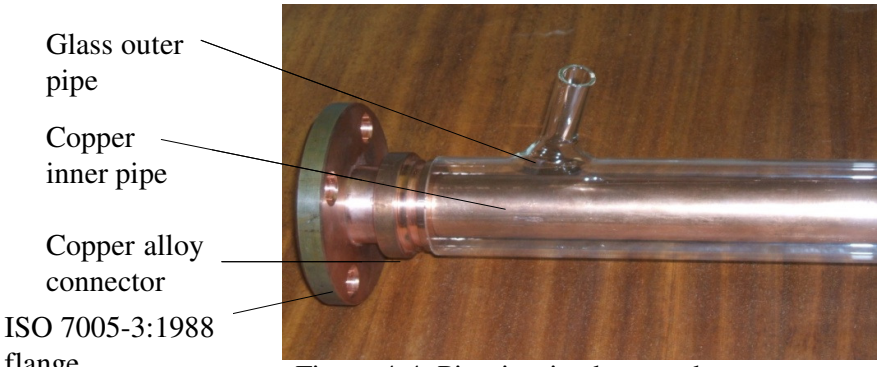

Figure 4-4: Pipe-in-pipe heat exchanger

The condenser section of the thermosyphon consists of seven pipe-in-pipe heat exchangers. Six of the sections consist of a 1 m copper pipe onto which two glass outer pipes are attached using a custom made copper alloy connector and silicon O-rings yielding a total cooled length of 1.85 m. The copper alloy connector is designed with an inner groove allowing for 2 mm diameter silicon O-ring, to ensure that a leak proof seal occurs between the connector and the copper pipe. The outside of the copper alloy connector also incorporates an O-ring groove, to ensure a leak proof seal between the connector and the glass pipe. The glass pipes have an inlet that is angled 45° to the vertical and the horizontal, ensuring that the cold water flows over the entire length of the exposed pipe, and turbulence is maintained in the cooling water in so far as possible. The fourth section, though similar in construction to the other three, consists of a 650 mm copper pipe and a 550 mm glass outer pipe. Figure 4-4 shows a detailed view of one end of a pipe-in-pipe heat exchanger

As can be seen in Figure 4-2, four transparent polycarbonate sight glasses are positioned in strategic places in order to visually identify two-phase flow patterns. Figure 4-5 shows a sight glass and some expected two-phase flow patterns for

horizontal and vertical flow. The sight glasses are manufactured from clear polycarbonate rod with a glass transition temperature of approximately 140 °C.

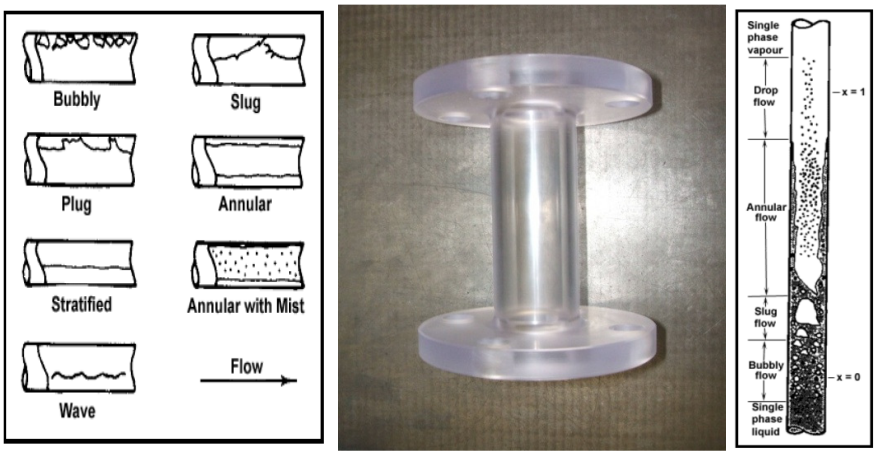

(a) (b) (c)

Figure 4-5: a) Horizontal two-phase flow patterns (Wolverine Tube, 2007). b) Polycarbonate sight glass. c) Vertical two-phase flow patterns (Collier & Thome, 1994)

A stainless steel expansion tank was manufactured and fitted with a glass tube level indicator in order to measure the variation in tank fill level. The tank is connected to the loop through a valve attached to the loop return line and is placed at a height of 12 m above the lower horizontal section of the loop.

4.2.2 Sensors

The physical layout of the thermocouples used in the experimental loop can be seen in Figure 4-2. Twelve sheathed, K-type thermocouple probes were used to measure the working fluid temperatures at the inlet and outlet of the condenser and evaporator section of the loop as well as at the inlet and outlet of each heat exchanger. A further eleven K-type thermocouples were placed 25 mm from the tip and central to each fin in a 20 mm deep Ø 1.8 mm hole within the fin to measure the temperature distribution.

In order to account for variation in the characteristics of different batches of thermocouple wire, the twelve sheathed thermocouples were purchased from the same roll. The eleven self-made thermocouples were also manufactured from consecutive sections of the same roll of thermocouple wire. The accuracy of these thermocouples and their respective data acquisition unit channels was verified by testing the thermocouples against a calibrated ISOTECH platinum resistance thermometer (PRT), as laid out in Appendix B.1. Though the test indicated that the thermocouples measure within an acceptable accuracy range, it was noticed that the error percentage increases incrementally with each subsequent channel, indicating that the error could be attributed to a drift error in the data acquisition

unit or card. To limit the effect of this error, the thermocouples were calibrated in specific channels and kept in the calibrated channels for the duration of the experiments.

The pressure difference across the orifice plate was measured using a HBM DP1-type transducer, No. 2929, with a 0.01 bar full scale reading; allowable nominal operating pressure is 50 bar. The pressure transducer was calibrated using a van Essen, BETZ 5000 water micro-manometer and a calibration curve was generated for both positive and negative pressure differences across the orifice plate pressure tappings. In order to identify the relationship between the mass flow rate and the pressure difference, the orifice plate was calibrated in-situ for bi-directional flow. Besides for ease of calibration, this has the added advantage of capturing the experimental geometry and equipment dependent variances and characteristics. Several tests were performed to establish repeatability and the resulting calibration curve is shown in Appendix B.2.

4.2.3 Data Acquisition

All fluid temperature and mass flow rate sensors were connected to a 34970A Agilent data logger with serial number MY44045582. Data integration took place over a period of 10 ms and was logged every ten seconds.

4.3 Experimental Procedure

Prior to experimentation, the loop was filled through the expansion tank with untreated tap water. Air was allowed to escape during the fill process through the air release valve at the top of the loop. This is crucial because the air trapped in the working fluid acts as an insulator and detrimentally affects heat transfer and consequently heat transfer coefficient accuracy. Air released by the working fluid during boiling was purged continuously until it was certain that no air remained in the system. This was ascertained visually by checking for air bubbles in the sight glasses and determining whether condensate and steam was present in the escaping gas. Prior to each experimental run, the water level in the expansion tank, room temperature, and ambient pressure were measured and noted. The test procedure as detailed in Appendix E was followed, digitally logging temperatures and pressure difference across the orifice plate. The mass flow rate of the cooling water in the heat exchanger and ammeter readings for each heating section were logged manually.

Note that the working fluid mass flow rate refers to the mass flow rate of the fluid inside the closed loop, as measured by the pressure difference across the orifice plate. This flow rate increases from zero as flow is developed in the loop and thus has a transient profile. The cooling water mass flow rate ($\dot{m}_{cw}$) refers to the mass flow rate of the cooling water in each of the condenser sections as measured manually. This mass flow rate is controlled through the use of a constant header

tank as well as ball valves at the outlet of each condenser section and thus has a constant value for the duration of the experiment for each condenser section.

Each experiment followed the same heat input procedure. During start-up, each heating element was set to 30% of maximum power input. The working fluid temperature was monitored and the power input maintained until thermal equilibrium was reached. At that stage, the power input was increased to 50%, 70% and 100% and the process repeated. The power supply was then switched off and the system was allowed to cool to initial conditions and the next experiment was only started once the loop was in thermal equilibrium with its surroundings.

5 RESULTS

In this section, the results obtained with the experimental setup, shown in section 4, are discussed in the light of different sets of representative test data. The results generated by the mathematical model described in section 3 are then discussed. Finally, a comparison is made between the theory and experiment.

5.1 Experimental Results

Twelve experiments, lasting at least 5 hours each, were performed with data logging occurring every ten seconds. The vast number of data points obtained would make presenting all the results meaningfully, neigh-impossible. Consequently, this section shows selected but typical experimental results for single and two-phase flow operating modes. Error analyses and repeatability of experimental measurements for single and two-phase operating modes as well as cooling water mass flow rates are given in Appendix C.

5.1.1 Single Phase Flow

Initially, the experimental loop was tested with all seven pipe-within-pipe heat exchangers operational. Table 5-11 shows the electrical power input, from start-up to shutdown, of a typical single phase operating mode with high cooling water mass flow rate. The table shows the percentage of full power, the time at which the power was increased, the equivalent electrical power of each heating section and the total electrical power. The power input was shut down at 15720 seconds and allowed to cool down. The cooling water mass flow rates corresponding to the condensers HE1 to HE7 are 0.085 kg/s, 0.106 kg/s, 0.093 kg/s, 0.112 kg/s, 0.116 kg/s, 0.089 kg/s and 0.090 kg/s respectively.

Table 5-1: Electrical power input (single phase, high cooling water mass flow rate)

Power	Time	Heater 1	Heater 2	Heater 3	Heater 4	Total
30%	0	437.5 W	437.5 W	226.8 W	118.1 W	1219.9 W
50%	4710	1264.4 W	1264.4 W	1064.7 W	382.7 W	3976.2 W
70%	8380	2041.2 W	2117.5 W	2117.5 W	718.7 W	6994.9 W
100%	12050	2822.6 W	2778.3 W	2912.2 W	970.7 W	9483.8 W

Figure 5-1 shows a typical set of experimental results for single phase operating mode with high cooling water mass flow rate. Figure 5-1(a) shows the average fin temperatures for each heating section (labelled 1 – 4 as outlined in Section 4); Figure 5-1(b) shows the working fluid temperatures measured at the four corners of the experimental loop; Figure 5-1(c) shows the difference in the condenser section inlet and outlet temperatures (labelled 1-7 as outlined in Section 4); Figure 5-1(d) shows the working fluid mass flow rate.

The working fluid temperatures are depicted in Figure 5-1(b). The temperature measured at the top of the evaporator section, T_{TL}, shows four distinct levels corresponding to increases in power input. Initially, the power input is 30% of full power and T_{TL} increases steadily to a plateau of 31.5 °C, when thermal equilibrium is reached. Once the power is increased to 50%, T_{TL} increases sharply and then steadily until it peaks at 49.8 °C. The third and fourth peaks, 72.0 °C and 77.5 °C respectively, correspond to further power increases to 70% and 100% of full power. These sections show typical responses for single-phase forced convection where the heat transfer coefficient is almost constant at thermal equilibrium (Whalley, 1987). The temperature measured at the top of the condenser section, T_{TR}, follows the same trend as T_{TL}, with a slightly lower peak. This slight drop in temperature is explained by the heat lost to the environment over the length of the upper horizontal copper pipe.

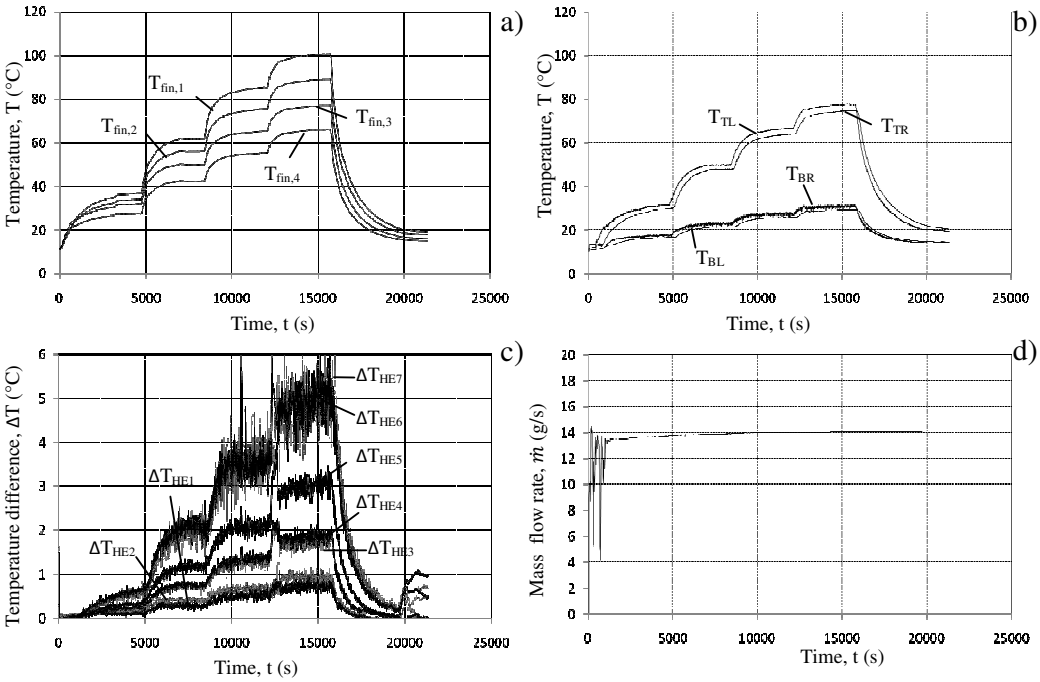

Figure 5-1 :Single phase flow operating mode, (a) average fin temperatures, (b) working fluid temperatures, (c) condenser cooling water temperature differences and (d) working fluid mass flow rate

The temperature measured at the bottom of the condenser, T_{BR}, increases steadily with time and follows a similar trend to the inlet temperature, with much lower maximum temperature levels. The peak temperatures corresponding to 30%, 50%, 70% and full power are 17.6 °C, 24.4°C, 30.0 °C and 31.5 °C respectively. The temperature measured at the evaporator inlet, T_{BL}, follows the same trend as T_{BR}. This slight drop in temperature is also due to the heat lost to the environment over the length of the lower horizontal copper pipe.

Figure 5-1(b) shows that the maximum working fluid temperature difference over the length of the condenser section ($T_{TR} - T_{BR}$) occurs at full power and equals 46.0 °C.

Figure 5-1(a) shows the average fin temperatures for the heating sections. The temperature profiles show steady inclines and definite steps at each power increase interval. The difference between the fin temperatures is due to individual resistances and power ratings (as can be seen in Table 5-11). The highest fin temperature, $T_{fin,1}$, reaches 100.0 °C, at 100% power, which is below working fluid saturation temperature (105.0 °C), indicating that nucleate boiling inception does not occur.

Figure 5-1(c) shows the temperature drops across the condenser sections. The profile is obtained by subtracting the measured inlet temperature from the measured outlet temperature and plotting the result. The largest temperature difference, corresponding to the most heat removed, occurs in the upper-most heat exchangers in the condenser section. The temperature drop across the sixth heat exchanger, ΔT_{HE6}, is not clearly visible, as it is overlapped by the temperature drop across the top heat exchanger, ΔT_{HE7}. Four distinct steps, corresponding to the increase in power input, are evident in the profile of ΔT_{HE7}. At full power, the average temperature difference is 5 °C with a ±0.5 °C oscillation. Heat is removed from the working fluid through the heat exchanger, as is evident from the increase in cooling water temperature difference. Since the inlet temperature remains practically constant, this increase indicates an increase in cooling water outlet temperature, which results in a decrease in working fluid temperature along the length of the heat exchanger. The next sequential heat exchanger will then have a lowered inlet working fluid temperature, resulting in a smaller temperature difference in the cooling fluid inlet and outlet temperatures. This explains the decrease in peak temperature differences from ΔT_{HE6} through ΔT_{HE1}.

Figure 5-1(d) shows the mass flow rate of the working fluid as measured by the pressure drop over the orifice plate. At start-up, the mass flow rate oscillates prior to stabilising at 14 g/s. This oscillation, typical of natural circulation loop start-up (Ruppersberg, 2007; Dobson and Ruppersburg, 2006), is explained as follows. Initially, the flow rate is zero. Heat is added to the system, increasing the temperature of the working fluid in the evaporator section and decreasing the density. The less dense fluid is driven by buoyancy, forced to rise and be replaced by the denser, cooler working fluid in the condenser section. This motion is impeded by friction, so, for the first 10 seconds, the mass flow rate remains zero while the difference in gradients between the working fluid in the evaporator section and the condenser section, increases. Once the buoyancy force overcomes the static friction force, the working fluid mass flow rate increases sharply. The working fluid in the evaporator section is buoyancy driven into the upper horizontal section of the experimental loop and the denser, cooler working fluid in the condenser section is gravity fed into the lower horizontal section. A practically instantaneous decrease in temperature, and increase in density, in the evaporator

section occurs, decreasing the mass flow rate. This process repeats itself until the mass flow rate stabilises, within the first 20 minutes of experimentation.

Experimentation resumed at a later date, with a decreased cooling water mass flow rate to attempt to achieve boiling in the experimental loop. The cooling water mass flow rates corresponding to the condensers HE1 to HE7 are 0.006 kg/s, 0.009 kg/s, 0.020 kg/s, 0.020 kg/s, 0.014 kg/s, 0.014 kg/s and 0.025 kg/s respectively. Table 5-2 shows the electrical power input, from start-up to shutdown, of a single phase operating mode with the lowest cooling water mass flow rate. The table shows the percentage of full power, the time at which the power was increased, the equivalent electrical power of each heating section and the total electrical power. The power input was shut down at 15890 seconds and the experimental equipment allowed to cool down for at least 24 hours.

Table 5-2: Electrical power input (single phase, low cooling water mass flow rate)

Power	Time	Heater 1	Heater 2	Heater 3	Heater 4	Total
30%	0	473.2 W	529.4 W	280 W	134.4 W	1417 W
50%	3700	1234.8 W	1176.7 W	1010.8 W	382.7 W	3805 W
70%	7950	2003.6 W	2003.6 W	1966.3 W	718.7 W	6692.2 W
100%	12210	2822.6 W	2778.3 W	2912.2 W	970.7 W	9483.8 W

Figure 5-2 shows the experimental results for single phase operating mode with low cooling water mass flow rate. Figure 5-2(a) shows the average fin temperatures for each heating section (labelled 1 to 4 as outlined in Section 4); Figure 5-2(b) shows the working fluid temperatures measured at the four corners of the experimental loop; Figure 5-2(c) shows the difference in the condenser section inlet and outlet temperatures (labelled 1-7 as outline in Section 4); Figure 5-2(d) shows the working fluid mass flow rate.

The working fluid temperatures, depicted in Figure 5-2(b), follow the same trends as in the previous experiments, with higher peak temperatures. T_{TL} peaks at 86.3 °C at 100% power, 8.8 °C higher than the corresponding peak for high cooling water mass flow rate. T_{BR} peaks at 38.3 °C, 6.8 °C higher than the corresponding peak in Figure 5-1(b). These increases are expected as less heat is removed with a lower flow rate, resulting in increased working fluid temperatures. Again, a slight drop in temperature over the length of the horizontal copper pipes is observed, yielding T_{TR} and T_{BR} profiles similar to, but slightly lower than T_{TL} and T_{BL} respectively. The maximum working fluid temperature difference over the length of the condenser section, ($T_{TR} - T_{BR}$), occurs at full power and equals 48 °C, 2 °C higher than experiments conducted with a high cooling water mass flow rate.

Figure 5-2(a) shows the average fin temperatures for the heating sections. The temperature profiles correspond well to those obtained in Figure 5-1(a). $T_{fin,1}$ shows a sudden drop in temperature around 7500 s. This corresponds to a thermocouple malfunction which occurred at that time. The thermocouple measuring the central fin temperature was accidentally detached from the fin,

coming into contact with the insulation material; the temperature measured is thus not indicative of the actual fin temperature. This failure would not affect the rest of the measurements and was ignored for the duration of this experiment.

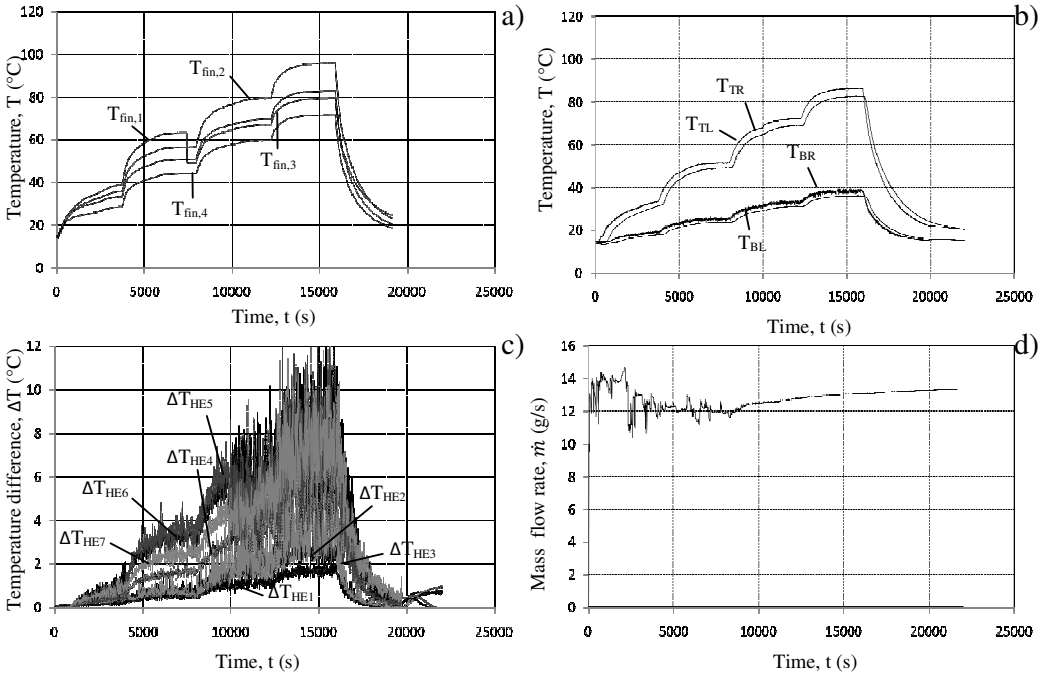

Figure 5-2 :Single flow operating mode (low cooling water mass flow rate), (a) average fin temperatures, (b) working fluid temperatures, (c) condenser cooling water temperature differences and (d) working fluid mass flow rate

Figure 5-2(c) shows the temperature difference across the condenser section. Looking at the graph, ΔT_{HE1} is the lowest profile and is depicted in black. ΔT_{HE2}, the next higher profile, is presented in black and is almost completely overlapped by the profile of ΔT_{HE3}, presented in the graph in light grey. ΔT_{HE4} and ΔT_{HE7}, the next successive profiles, are depicted in black and light grey respectively. ΔT_{HE6} is depicted in black and is almost completely overlapped by the profile of ΔT_{HE5}, depicted in a dark grey. The profiles follow the same trends observed in the previous experiments, with higher values and a smaller difference between heat exchanger temperature differences. ΔT_{HE6} and ΔT_{HE5} overlap almost entirely and peak at approximately 8 °C, with a ±2 °C oscillation. The peak is 3 °C higher than the previous experiment and the oscillations increase four-fold at full power. This increase in oscillations can be explained by the increased effect of air presence in the cooling water at low flow rates. The next sequential heat exchanger temperature differences decrease in maximum values from ΔT_{HE4} to ΔT_{HE1}.

Figure 5-2(d) shows the mass flow rate of the working fluid as measured by the pressure drop over the orifice plate. At start-up, the mass flow rate shows similar oscillations to those in Figure 5-2 (d) with a lower amplitude and frequency. The

flow rate takes longer to stabilise, with oscillations terminating only after 2 hrs of experimentation. It is clear from Figure 5-2 that boiling will not occur with all seven heat exchangers active. The single phase operating mode is able to remove the maximum available input of 9483.8 W.

5.1.2 Single to Two-Phase Flow

In order to achieve boiling in the experimental loop, only the top most heat exchanger was operated while the other six were bypassed. Table 5-3 shows the electrical power input, from start-up to shutdown, of a typical single to two phase operating mode experiment. The table shows the percentage of full power, the time at which the power was increased, the equivalent electrical power of each heating section and the total electrical power. Boiling started at t = 11090 s. The power input was shut down at 17040 s and allowed to cool down. The cooling water mass flow rates corresponding to the condenser HE7 is 0.192 kg/s.

Table 5-3: Electrical power input (single to two-phase)

Power	Time	Heater 1	Heater 2	Heater 3	Heater 4	Total
30%	0	420.2 W	437.5 W	226.8 W	118.1 W	1202.6 W
50%	4140	1205.6 W	1176.7 W	1010.8 W	354.9 W	3748 W
70%	7800	2041.2 W	1966.3 W	2003.6 W	680.4 W	6691.5 W
100%	13290	2822.68 W	2778.3 W	2912.2 W	926.1 W	9439.2 W

Figure 5-3 shows the visually identified flow patterns at each of the active sight glasses. Single phase flow is identified by the presence of only water in the three sight glasses. As the quality in the working fluid increases from zero, distinct two-phase flow patterns are identified. Two-phase flow is initially exhibited by the flow of small (<1 mm diameter) bubbles which grow and increase in number to establish bubbly flow with bubbles of approximately uniform size. As the quality increases, the amount of vapour and thus the number of bubbles increases, increasing collisions between the bubbles. Some of these collisions result in bubbles coalescing and forming large bullet shaped bubbles, or plugs. These plugs, together with some small bubbles distributed through the flow, are indicative of plug flow. The plugs, due to buoyancy, flow upward, while the liquid film around the plug has a gravity driven, downward flow. As the quality increases, the vapour velocity increases, ultimately disrupting the liquid film and resulting in churn flow. Churn flow is visually identified by liquid level oscillations and no uniform bubble flow (Whalley, 1987). This flow pattern is evident until boiling subsides after shutdown.

The sight glass positioned in the upper horizontal pipe does not show the expected development of two-phase flow patterns. Bubbly and plug flow are bypassed and only stratified flow, with interlopes of wavy flow, are evident. Bubbly flow enters the horizontal pipe, the denser liquid remains at the bottom of the pipe while the lighter, buoyancy driven vapour bubbles collect at the top. The bubbles, over the length of the pipe, coalesce, until eventually the liquid and vapour phases of the

working fluid are fully stratified with a smooth phase interface (Whalley, 1987). Wavy flow occurs when the liquid flow smashes into the 90° elbow. A periodic counter flow wave moves back into the pipe as a result of liquid build up and bridging before the 90° elbow at the condenser entrance.

When the stratified flow in the horizontal pipe reaches the condenser section, the liquid tends to flow along the sides forming an annular liquid film, containing a predominantly vapour core. Some small liquid drops are visible within the core, as is indicative of vertical annular flow.

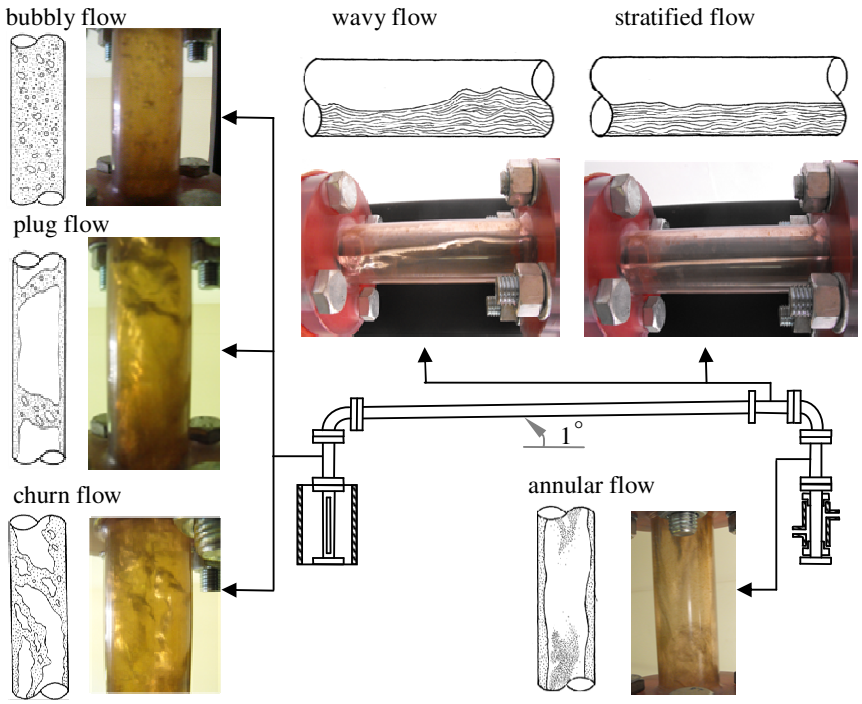

Figure 5-3: Visually identified flow patterns

Figure 5-4 shows a typical set of experimental results for single to two-phase operating mode. Figure 5-4(a) shows the average fin temperatures for each heating section (labelled 1 to 4 as outlined in Section 4); Figure 5-4(b) shows the working fluid temperatures measured at the four corners of the experimental loop; Figure 5-4(c) shows the difference in the condenser section inlet and outlet temperatures; Figure 5-4(d) shows the working fluid mass flow rate.

The working fluid temperatures are depicted in Figure 5-4(b). The temperature measured at the top of the evaporator section, T_{TL}, increases steadily to 40 °C, while the power input is 30% of full power. A second rise corresponds to the increase of power to 50%, where the temperature rises to 72 °C. These sections show typical responses for single-phase forced convection where the heat transfer coefficient is almost constant at thermal equilibrium (Whalley, 1987). The third

rise, corresponding to the power increase to 70% shows a sudden increase in temperature after about 10500 s. This increase can be explained by the onset of subcooled nucleate boiling which is characterized by an increase in heat transfer coefficient until the bulk fluid temperature reaches saturation temperature (Mills, 1999). The fin temperature, and thus the wall temperature, exceeds the saturation temperature (as can be seen in Figure 5-4(a)) and bubble growth occurs at the nucleation sites. As these bubbles grow, they protrude into the cooler liquid, which collapses them and rapidly increasing the bulk fluid temperature until saturation is reached (Whalley, 1987). T_{TL} peaks at 113.24 °C, at 11090 s, the saturation temperature of the working fluid. During boiling, the temperature oscillates between 110 and 113.24 °C and remains constant despite a further increase to 100% power. The slight variation in temperature can be ascribed to the mass flow rate oscillations. An increase in mass flow rate equates to an increase in net heat transferred to the fluid and thus a temperature increase and vice versa. Thus, variation in mass flow rate would mean a variance in the heat transferred to the working fluid through the fins and results in a variation in the working fluid temperature, this dynamic behaviour being characteristic of flow when boiling occurs. The temperature measured at the top of the condenser section, T_{TR}, follows the same trend as T_{TL}, with a slightly lower peak. This slight drop in temperature is due to the heat lost to the environment over the length of the upper horizontal copper pipe.

The temperature measured at the bottom of the condenser, T_{BR}, increases steadily with time and follows a similar trend to the inlet temperature until boiling starts. At the onset of boiling, the temperature drops steadily to a minimum of 50 °C at approximately 14000 s. As the bulk fluid temperature increases to saturation temperature, the heat transfer coefficient also steadily increases. The subcooled boiling becomes saturated nucleate boiling which is characterized by a high, relatively constant heat transfer coefficient (Whalley, 1987). This increased heat transfer coefficient results in more effective cooling in the condenser section, explaining the temperature drop. Nucleate boiling continues while the radial temperature distribution in the working fluid remains linear (Whalley, 1987). After the power is increased at 13290 s, T_{BR} again increases steadily until system shutdown. This increase is attributed to the departure from nucleate boiling and the gradual supplanting of convective boiling, where heat is transferred by conduction and convection through a thin liquid film into the vapour core (also known as film evaporation) (Mills, 1999). Evaporation takes place at the liquid-vapour interface and the heat transfer coefficient increases slowly. This increase in heat transfer coefficient is due to the predominance of annular flow and a constant decrease in film thickness with an increase in quality (Mills, 1999). The temperature oscillates with an amplitude of approximately 5 °C during boiling, which again can be attributed to the oscillating mass flow rate. The temperature measured at the evaporator inlet, T_{BL}, follows the same trend as T_{BR}, with a slightly lower value. This slight drop in temperature is, as ever, due to the heat lost to the environment over the length of the lower horizontal copper pipe.

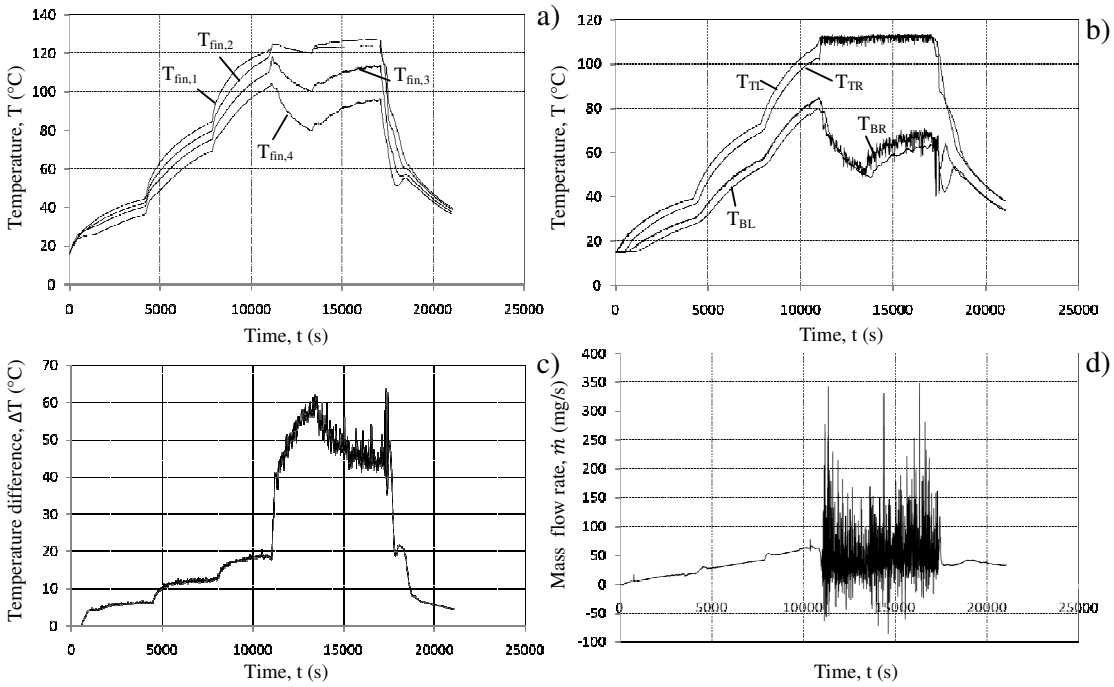

Figure 5-4 :Single to two-phase flow operating mode, (a) average fin temperatures, (b) working fluid temperatures, (c) condenser cooling water temperature differences and (d) working fluid mass flow rate

Figure 5-4(a) shows the average fin temperatures for the heating sections. The temperature profiles show steady inclines and definite steps at each power increase interval. At the onset of subcooled nucleate boiling, a peak appears in the fin temperatures. This peak coincides with a sudden drop in mass flow rate, as seen in Figure 5-4(d), prior to fully saturated nucleate boiling and results in a decrease in heat transferred from the fin to the working fluid. As the electrical input is constant, the fin temperatures increase with this decrease in mass flow rate. Once the boiling is fully saturated, the temperature profiles follow a similar trend to T_{BR}, showing an initial decrease where nucleate boiling is dominant and gradual increase as convective boiling supplants nucleation. The figure shows a clear difference in temperatures along the length of the evaporator section. The bottom two heating section temperatures ($T_{fin,1}$ and $T_{fin,2}$) are much higher than the top two ($T_{fin,3}$ and $T_{fin,4}$) and peak at approximately 125 °C. This is because boiling inception only occurs midway in the third heating section. The bottom two sections are thus exposed to single phase fluid only, which significantly decreases the heat transfer coefficient in these regions.

Figure 5-4(c) shows the temperature drop across the condenser section. The profile is obtained by subtracting the measured inlet temperature ($HE_{7,in}$) from the measured outlet temperature ($HE_{7,out}$) and plotting the result. It is interesting to note that in the single phase region, the temperature difference is directly

proportional to the power input. If the first peak of 7.52 °C corresponds to a 30% power input, theoretically the 50% and 70% peaks should be 12.53 °C and 17.55 °C respectively. The 50% power input peak occurs at 12.4 °C and the 70% peak at 18.6 °C. The small discrepancy from theoretical values can be attributed to the relative inaccuracy of the variable voltage dial limiting the input power. At the onset of nucleate boiling, the temperature difference jumps to 40 °C and then slowly increases to a maximum 60 °C. This is due to the high boiling heat transfer coefficient indicative of this boiling type (Whalley, 1987). Once convective boiling supplants nucleate boiling, the temperature difference decreases steadily to approximately 45 °C. The cause of this decrease, as can be clearly seen in Figure 5-4(b), is the increase in bulk fluid temperature at the condenser outlet due to a steadily increasing evaporative heat transfer coefficient during convective boiling. This figure shows clearly that more heat can be removed during the two-phase operating mode than utilising only single phase liquid.

Figure 5-4(d) shows the mass flow rate of the working fluid. During single phase operation, the mass flow rate steadily increases and stabilises at 17.98 mg/s for 30% power, 39.5 mg/s for 50% power and 61.2 mg/s for 70% power. Each increase of power input results in a relatively small peak in mass flow rate. The heat transferred to the working fluid is directly proportional to the difference in fin and bulk fluid temperature, as well as the flow rate. The instant the power is increased, the temperature difference is unchanged, resulting in an increased mass flow rate. At the onset of subcooled nucleate boiling, the mass flow rate drops sharply. During subcooled boiling, the wall temperature exceeds the bulk fluid temperature. Bubbles form at nucleation sites on the tube wall but, due to the cooler core bulk temperature, remain affixed to the wall (Whalley, 1987). Once the bubbles break free, the cooler fluid temperature forces the vapour to condense, collapsing the bubble. While these bubbles line the tube wall they act as flow restrictions, increasing the wall friction and thus decreasing the working fluid flow rate. Once the nucleate boiling becomes saturated, the mass flow rate starts oscillating with a relatively large amplitude. The oscillations can be attributed to the varying driving force as a result of pressure differences between the heated and cooled section. As T_{BR} decreases, the amplitude of the oscillations decreases, reaching a local minimum of approximately 100 mg/s. Once T_{BR} increases again, the amplitude increases until the system is shut down.

The mass flow rate obtained during the single to two-phase operating mode experiments is much lower than those obtained for single phase operating mode experiments. This is expected because the density gradient is greater while all seven heat exchangers are operating.

5.1.3 Heat Transfer Coefficients

This section details how experimental inside-pipe heat transfer coefficients were calculated for both the evaporator and condenser sections.

5.1.3.1 Evaporator

The total heat added to the system can be calculated by summing the heat removed by the cooling water and the calculated heat loss:

$$\dot{Q}_{in} = \dot{Q}_{cw} + \dot{Q}_{loss} \quad (5\text{-}1)$$

In equation 5-1, Q_{loss} is the heat lost from the pipework to the surroundings.

The total heat transfer from the fins to the working fluid can also be written as:

$$\dot{Q}_{in} = A_{zod} h_{e,i} \left(T_{e,wall} - T_l\right) \quad (5\text{-}2)$$

In equation 5-2, A_{zod} refers to the heated area of the pipe section.

Setting equation 5-1 equal to equation 5-2 and solving for h_i yields:

$$h_{e,i} = \frac{\dot{Q}_{cw} + \dot{Q}_{loss}}{A_{zod}(T_{wall} - T_l)} \quad (5\text{-}3)$$

The experimental results obtained and detailed in Sections 5.1.1 and 5.1.2 were used in equation 5-3 to calculate inside-pipe evaporator heat transfer coefficient.

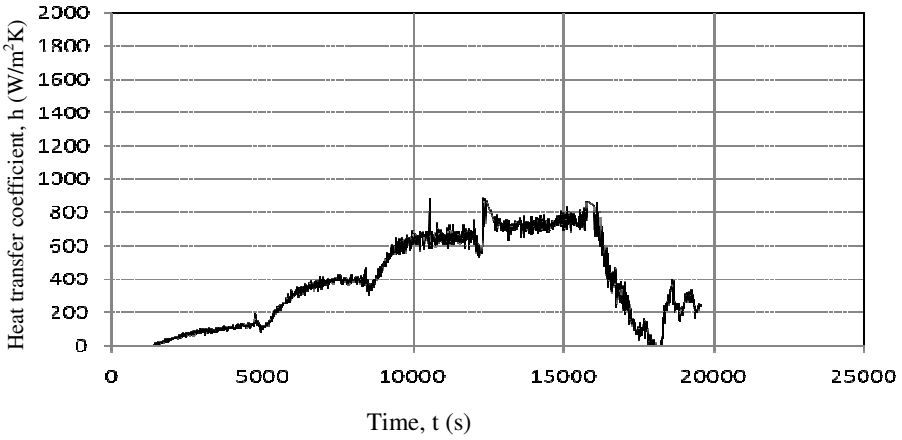

Figure 5-5: Experimentally determined inside-pipe evaporator heat transfer coefficient for single phase operating mode, high cooling water mass flow rate, for H3

Figure 5-5 shows the experimentally determined heat transfer coefficients for single phase flow operating mode with high cooling water mass flow rate, for the third heating section, $h_{e,i,H3}$. The figure shows that the heat transfer coefficient rises steadily in four distinct steps, corresponding to the increase in electrical power input. These steps show a rise in heat transfer coefficient value until a plateau is neared as the system approaches thermal equilibrium. This corresponds to expected heat transfer coefficient theoretical behaviour (Whalley, 1987). The

heat transfer coefficient peaks at approximately 121 W/m^{2}K at 30% power, 405 W/m^{2}K at 50% power, 669 W/m^{2}K at 70% power and 753 W/m^{2}K at full power.

Figure 5-6 shows the experimentally determined inside-pipe evaporator heat transfer coefficients, for single phase flow operating mode with low cooling water mass flow rate, for the third heating section. The heat transfer coefficient profile follows a similar trend to that in Figure 5-5 with higher peak values. The heat transfer coefficient peaks at approximately 132 W/m^{2}K at 30% power, 507 W/m^{2}K at 50% power, 963 W/m^{2}K at 70% power and 1204 W/m^{2}K at full power.

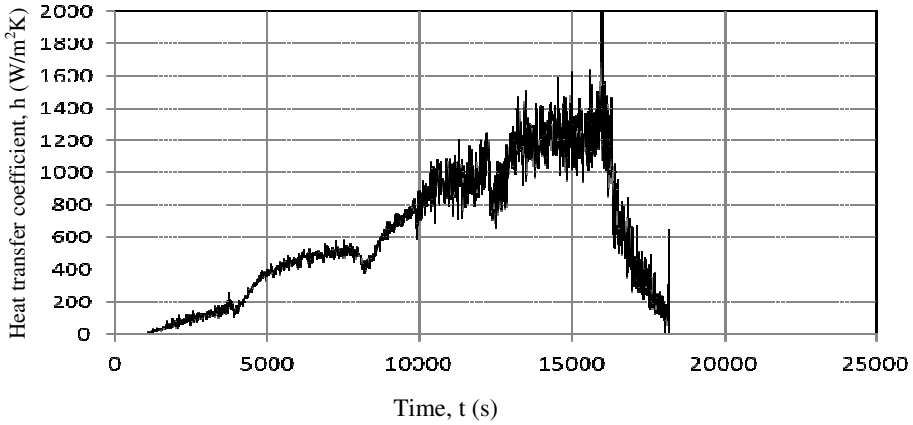

Figure 5-6: Experimentally determined inside-pipe evaporator heat transfer coefficient for single phase operating mode, low cooling water mass flow rate, for H3

Figure 5-7 shows the experimentally determined heat transfer coefficients, for single to two-phase flow operating mode, for the third heating section, where boiling inception occurred. In the single phase region, the heat transfer coefficient rises steadily in three distinct steps, similar to the profiles obtained in Figure 5-5 and Figure 5-6. The heat transfer coefficient peaks at approximately 109 W/m^{2}K at 30% power, 223 W/m^{2}K at 50% power and 401 W/m^{2}K at 70% power prior to the onset of boiling.

At approximately 10500 s, the heat transfer rate rises sharply to an average peak value of 1100 W/m^{2}K. This rapid increase is a typical indication of the onset of nucleate boiling (Whalley, 1987). Once the nucleate boiling becomes saturated, the heat transfer coefficient ceases rising and remains relatively constant at a local averaged minimum of approximately 756 W/m^2 K.

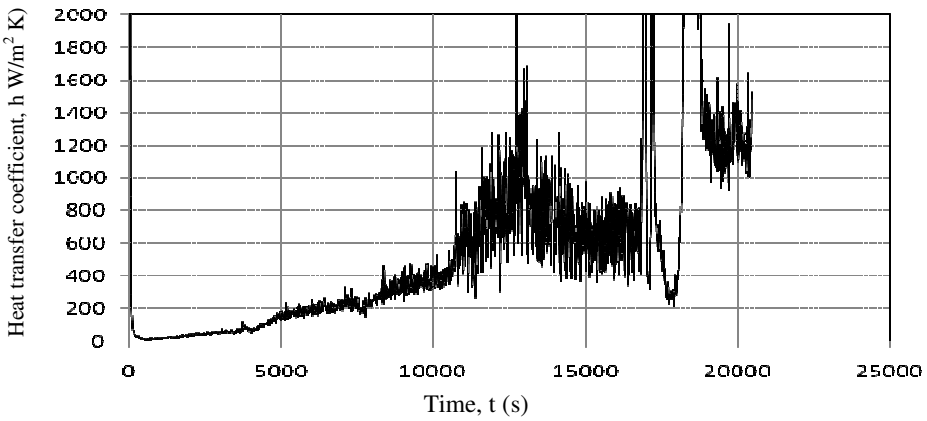

Figure 5-7: Experimentally determined inside-pipe evaporator heat transfer coefficient for single to two-phase operating mode, for H3

5.1.3.2 Condenser

The total heat removed by the heat exchangers is calculated using:

$$\dot{Q}_{cw} = \dot{m}_{cw} C_p \Delta \mathrm{T_{cw}} \tag{5-4}$$

The total heat transfer in the exchanger can also be written, using the logarithmic mean temperature method (Mills, 1999), as:

$$\dot{Q}_{cw} = U \wp L \Delta T_{lm} \tag{5-5}$$

The perimeter, $\wp$, in equation 5-5 need not be specified since only the overall heat transfer coefficient and perimeter product, $U\wp$, will be used in further calculations.

Where the logarithmic mean temperature difference (LMTD) for counter flow heat exchangers is calculated as follows (Mills, 1999):

$$\Delta T_{lm} = \frac{(T_H - T_C)_L - (T_H - T_C)_0}{ln[(T_H - T_C)_L / (T_H - T_C)_0]} \tag{5-6}$$

Setting equation 5-4 equal to equation 5-5 and solving for $U\wp$ yields:

$$U \wp = \frac{\dot{m}_{cw} C_p \Delta \mathrm{T_{cw}}}{L \Delta T_{lm}} \tag{5-7}$$

The experimental results obtained and detailed in Section 5.1 were used in equation 5-7 to solve for the overall heat transfer coefficient and perimeter product. In order to isolate the inside-pipe convective heat transfer coefficient, the heat transferred through the exchanger is analysed, taking into consideration convection from the heated water inside the copper pipe, conduction through the pipe wall and convection through the cooling water. Figure 5-8 shows an axially symmetric section of the heat exchanger and the corresponding thermal circuit for heat flow through the exchanger tube.

By definition of the overall heat transfer coefficient (Mills, 1999):

$$\frac{1}{U_{\wp} L} = \sum R = R_{c,i} + R_k + R_{c,o} \tag{5-8}$$

$$\therefore \frac{1}{U_{\wp} L} = \frac{1}{2\pi L r_i h_{c,i}} + \frac{\ln(r_o/r_i)}{2\pi k L} + \frac{1}{2\pi L r_o h_{c,o}} \tag{5-9}$$

In equation 5-9, the outside convective heat transfer coefficient is calculated using established correlations for forced convection. For laminar flow, a constant value is taken for the Nusselt number, and the Gnielinski correlation (equation 2-42) is used for turbulent flow:

$$h_{c,o} = \frac{Nu_{cw} k_{cw}}{D_{eq}} \tag{5-10}$$

$$Nu_{cw} = \begin{cases} 4.861 & if\ Re_{cw} < 1181 \\ \frac{(f_{cw}/8)\cdot(Re_{cw}-1000)\cdot Pr_{cw}}{1+12.7\cdot(f_{cw}/8)^{0.5}\cdot(Pr_{cw}{}^{2/3}-1)} & if\ Re_{cw} \geq 1181 \end{cases} \tag{5-11}$$

The validity of using equation 5-11 to accurately determine $h_{c,o}$ is addressed in Appendix B-3.

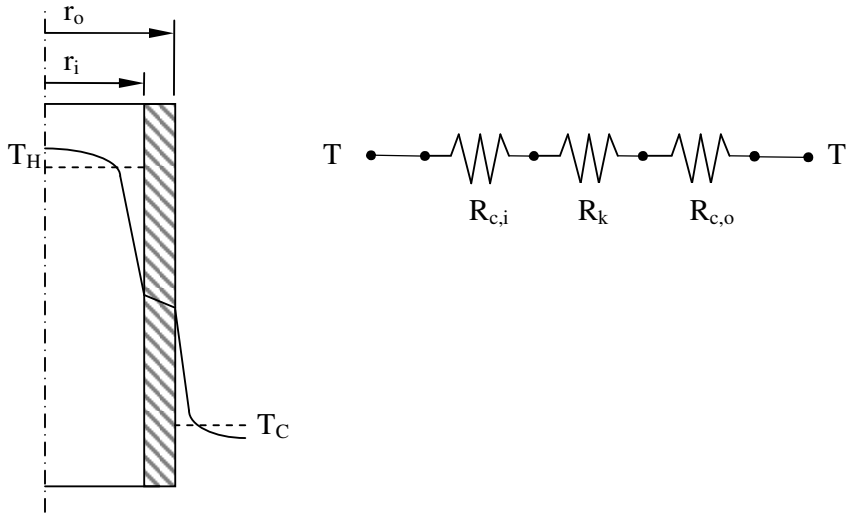

Figure 5-8: Local temperature profile and thermal circuit for heat flow through the exchanger tube (Mills, 1999)

Isolating the inside-pipe convective heat transfer coefficient in equation 5-9 yields:

$$h_{c,i} = \left(2\pi r_i \left(\frac{1}{U_{\wp}} - \frac{\ln(r_o/r_i)}{2\pi k} - \frac{1}{2\pi r_o h_{c,o}}\right)\right)^{-1} \tag{5-12}$$

Figure 5-9 shows the experimentally determined heat transfer coefficients for single phase flow operating mode with high cooling water mass flow rate, for the upper most heat exchanger (HE_7) in the condenser section. The figure shows that the heat transfer coefficient rises in four steps, corresponding to the increase in electrical power input. These steps show a rise in heat transfer coefficient value

until a plateau is neared as the system approaches thermal equilibrium. This corresponds to condensation heat transfer coefficient theory (Whalley, 1987). The heat transfer coefficient peaks at approximately 253 W/m^{2}K at 30% power, 401 W/m^{2}K at 50% power, 517 W/m^{2}K at 70% power and 577 W/m^{2}K at full power. Oscillations vary between ±50 W/m^{2}K at 30% power, to ±100 W/m^{2}K at 100% power.

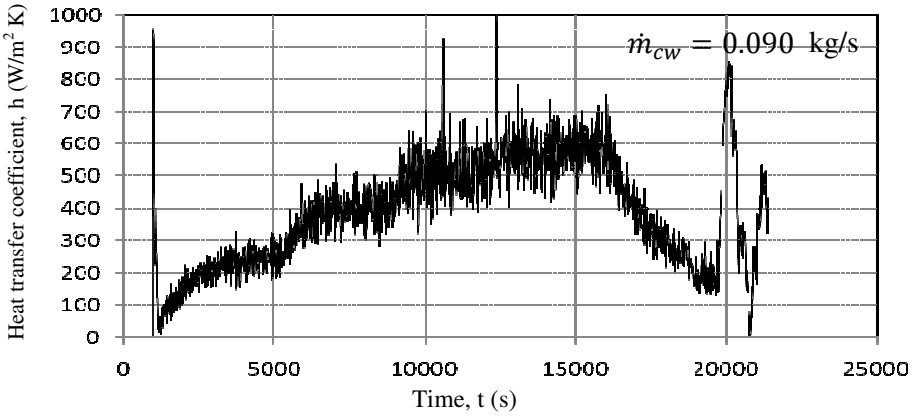

Figure 5-9: Experimentally determined inside-pipe condenser heat transfer coefficient for single phase operating mode, high cooling water mass flow rate, for HE_7

Figure 5-10 shows the experimentally determined heat transfer coefficients for single phase flow operating mode with low cooling water mass flow rate, for the upper most heat exchanger (HE_7) in the condenser section. The heat transfer coefficient profile follows a similar trend to that in Figure 5-9 with lower and less distinct peaks. The heat transfer coefficient peaks at approximately 220 W/m^{2}K at 30% power, 295 W/m^{2}K at 50% power, 364 W/m^{2}K at 70% power and 492 W/m^{2}K at full power. This decrease in the peaks is due to the dependency of the heat transfer coefficient on cooling water mass flow rate (shown in Equation 5-7).

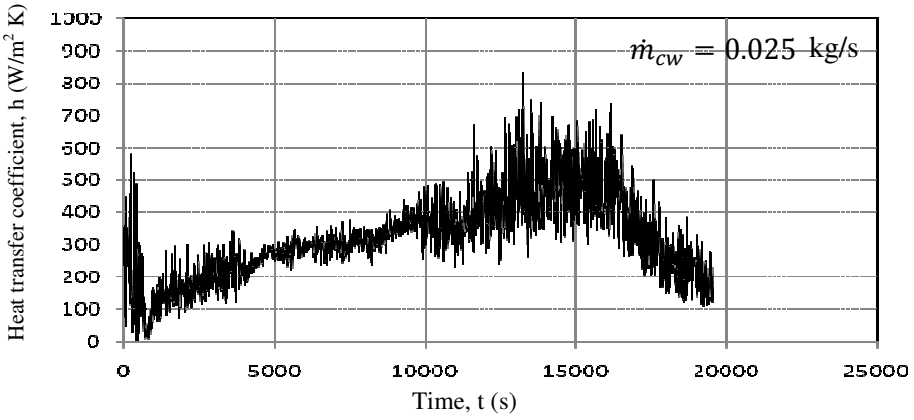

Figure 5-10: Experimentally determined inside-pipe condenser heat transfer coefficient for single phase operating mode, low cooling water mass flow rate, for HE_7

Figure 5-11 shows the experimentally determined heat transfer coefficients for a typical single to two phase operation mode experiment.

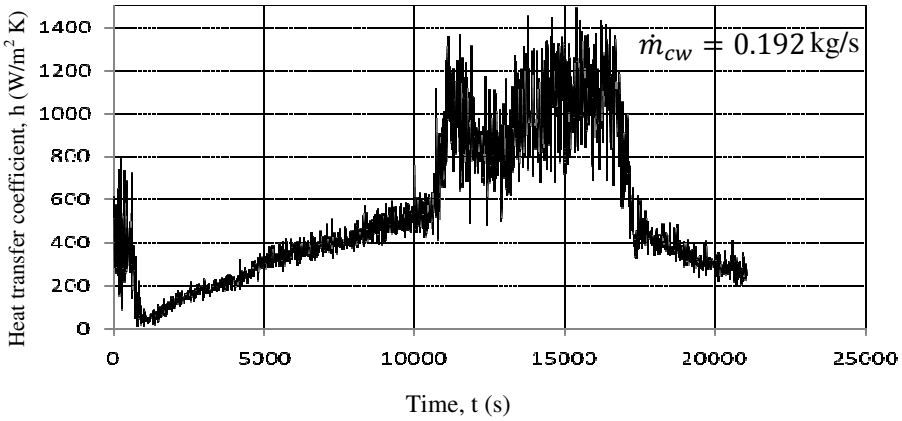

Figure 5-11: Experimentally determined inside-pipe condenser heat transfer coefficient for single to two-phase operating mode, for HE_7

The figure shows that in the single phase region, the heat transfer coefficient rises steadily in three distinct steps. These steps show a rise in heat transfer coefficient value until a constant peak is neared as the system approaches thermal equilibrium at each of the power input levels, which corresponds to theoretical behaviour (Whalley, 1987). The heat transfer coefficient peaks at approximately 200 W/m^{2}K at 30% power, 400 W/m^{2}K at 50% power and 560 W/m^{2}K at 70% power prior to the onset of boiling. At the onset of saturated nucleate boiling, the heat transfer rate rises sharply to an average peak value of 1200 W/m^{2}K and then decreases to a local averaged minimum of 845 W/m^2 K. As the vapour, generated initially through saturated nucleate boiling, reaches the externally cooled condenser section, condensate forms on the walls of the copper pipe. This occurs in the form of film condensation and a liquid film wets the entire surface. This film acts as thermal resistance to heat transfer from the bulk fluid to the condenser section walls (Mills, 1999). As the film thickness grows, the resistance to heat transfer increases, thereby decreasing the heat transfer coefficient in the condenser.

As convective boiling gradually supplants nucleate boiling, the inside-pipe heat transfer coefficient increases steadily and stabilises at a peak average value of 1100 W/m^{2}K. This increase occurs because the vapour quality in the bulk fluid increases (Mills, 1999), as the convective boiling becomes more dominant. This effectively decreases the film thickness, decreasing the resistance to flow and increasing the heat transfer coefficient.

5.2 Theoretical Results

The theoretical heat transfer coefficients were calculated using the mathematical model detailed in section 3 and correlations given in section 2.4.1. Fluid parameters were evaluated using experimentally determined temperatures and mass flow rates.

5.2.1.1 Evaporator

For single phase operating mode, the maximum Reynolds number falls below the critical value, the flow is therefore always laminar and only the Collier correlation can be used (Collier & Thome, 1994) to calculate the inside-pipe evaporator heat transfer coefficients:

$$Nu_D = 0.17 Re_D^{0.33} Pr^{0.43} \left(\frac{Pr}{Pr_w}\right)^{0.25} Gr^{0.1} \qquad Re_D \leq 2000 \qquad (2\text{-}40)$$

In Equation 2-40, the Prandtl and Grashof numbers are calculated as follows (Mills, 1999):

$$Pr = \frac{c_p \mu_l}{k_l} \qquad (5\text{-}13)$$

$$Gr = \frac{\beta \Delta T g L^3}{\left(\frac{\mu}{\rho}\right)^2} \qquad (5\text{-}14)$$

In equation 5-14, L refers to length of control volume in the direction of flow.

During the single to two-phase operating mode experiments, the Reynolds number does exceed the critical value, shortly after the onset of nucleate boiling. The Gnielinski correlation (as given by Mills, 1999) is thus used, with Equation 2-40, in the single phase region, to calculate the inside-pipe evaporator heat transfer coefficients.

$$Nu_D = \frac{(f/8)\cdot(Re_D - 1000)\cdot Pr}{1 + 12.7\cdot(f/8)^{0.5}\cdot(Pr^{2/3} - 1)} \qquad 3000 \leq Re_D \leq 10^6 \qquad (2\text{-}41)$$

For two-phase boiling, Chen's correlation (as given by Whalley, 1987) is used:

$$h = h_{NB} + h_{FC} = Sh_{FZ} + Fh_l \qquad (2\text{-}44)$$

Figure 5-12 shows the resulting theoretically determined inside-pipe evaporator heat transfer coefficients for the third heating section for single phase operating mode with high cooling water mass flow rate (Figure 5-12(a)), with low cooling water mass flow rate (Figure 5-12(b)) and single to two-phase operating mode (Figure 5-12(c)). Figure 5-12(a) shows the theoretically determined heat transfer coefficients for single phase flow operating mode with high cooling water mass flow rate, for the third heating section. At start-up, the theoretical profile oscillates with an amplitude and frequency corresponding to the mass flow rate as shown in Figure 5-1(d). Figure 5-12(a) shows that the heat transfer coefficient rises steadily in four distinct steps, corresponding to the increase in electrical power input. The heat transfer coefficient peaks at approximately 168 W/m^{2}K at 30% power, 188

W/m^{2}K at 50% power, 211 W/m^{2}K at 70% power and 227 W/m^{2}K at full power.

Figure 5-12(b) shows the theoretically determined heat transfer coefficients for single phase flow operating mode with low cooling water mass flow rate, for the third heating section. Four distinct steps, corresponding to the increase in electrical power input, are also visible, but at slightly lower values than those obtained in Figure 5-12(a). The start-up oscillations are lower in amplitude, but the heat transfer coefficient takes longer to stabilise, corresponding to the mass flow rate in Figure 5-2(d). The heat transfer coefficient peaks at approximately 151 W/m^{2}K at 30% power, 169 W/m^{2}K at 50% power, 203 W/m^{2}K at 70% power and 223 W/m^{2}K at full power.

Figure 5-12(c) shows the experimentally determined heat transfer coefficients, for single to two-phase flow operating mode, for the third heating section. In the single phase region, the heat transfer coefficient rises steadily in three distinct steps. The heat transfer coefficient peaks at approximately 50 W/m^{2}K at 30% power, 127 W/m^{2}K at 50% power and 166 W/m^{2}K at 70% power prior to the onset of boiling.

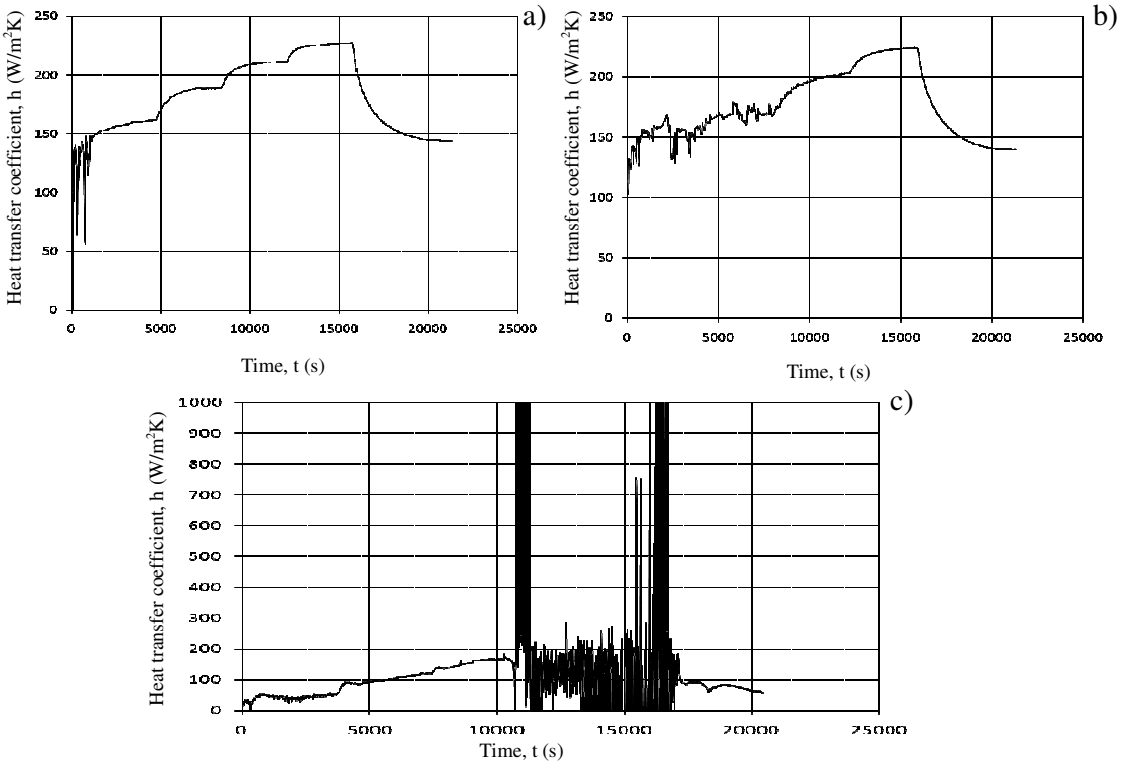

Figure 5-12: Theoretically determined inside-pipe evaporator heat transfer coefficient for (a) single phase operating mode with high cooling water mass flow rate, for H3, (b) single phase operating mode with low cooling water mass flow rate, for H3, and (c) single to two-phase operating mode, for H3

At approximately 10100 s, the heat transfer rate decreases sharply and starts to oscillate, though the average value does not increase. This rapid decrease is atypical of heat transfer coefficient behaviour at the onset of nucleate boiling (Whalley, 1987). This could be explained by calculation error and uncertainty. A relatively small difference between the small values in equation 5-10 would give amplified errors. Once the nucleate boiling becomes saturated, the oscillations decrease and heat transfer coefficient remains relatively constant at approximately 133 W/m^2 K. After approximately 13620s, corresponding to the point of departure from nucleate boiling, the oscillations increase rapidly while the average heat transfer coefficient value decreases.

5.2.1.2 Condenser

For single phase operating mode, the maximum Reynolds number falls below the critical value, the flow is therefore always laminar and only the Collier correlation can be used (as with the evaporator) (Collier & Thome, 1994) to calculate the heat transfer coefficients:

$$Nu_D = 0.17 Re_D^{0.33} Pr^{0.43} \left(\frac{Pr}{Pr_w}\right)^{0.25} Gr^{0.1} \qquad Re_D \leq 2000 \qquad (2\text{-}40)$$

During the single to two-phase operating mode experiments, the Reynolds number does exceed the critical value, shortly after the onset of nucleate boiling. The Gnielinski correlation (as given by Mills, 1999) is thus included, with Equation 2-40, in the single phase region, to calculate the heat transfer coefficients.

$$Nu_D = \frac{(f/8)\cdot(Re_D - 1000)\cdot Pr}{1 + 12.7\cdot(f/8)^{0.5}\cdot(Pr^{2/3} - 1)} \qquad 3000 \leq Re_D \leq 10^6 \qquad (2\text{-}41)$$

For vertical two-phase condensation, the correlation developed by Chen is used (Chen, Gerner, & Tien, 1987):

$$Nu_x = \left[\left(0.31 \cdot Re_x^{-1.32} + \frac{Re_x^{2.4}\cdot Pr_l^{3.9}}{2.37\times10^{14}}\right)^{\frac{1}{3}} + \frac{A_D \cdot Pr_l^{1.3}}{771.6} \cdot (Re_{ter} - Re_x)^{1.4} \cdot Re_x^{0.4}\right]^{1/2} \qquad (2\text{-}85)$$

Figure 5-13 shows the resulting theoretically determined heat transfer coefficients for the upper-most heat exchanger (HE_7) in the condenser section. The figure shows results for single phase operating mode with high cooling water mass flow rate (Figure 5-13(a)), single phase operating mode with low cooling water mass flow rate (Figure 5-13(b)) and single to two-phase operating mode (Figure 5-13(c)). Figure 5-13(a) shows the theoretically determined heat transfer coefficients for single phase flow operating mode with high cooling water mass flow rate. The heat transfer coefficient follows the same trend as those obtained for the evaporator section, shown in Figure 5-12(a). The heat transfer coefficient rises steadily in four distinct steps, corresponding to the increase in electrical power input. The heat transfer coefficient peaks at approximately 160 W/m^{2}K at 30% power, 189 W/m^{2}K at 50% power, 213 W/m^{2}K at 70% power and 228 W/m^{2}K at full power.

Figure 5-13(b) shows the theoretically determined heat transfer coefficients for single phase flow operating mode with low cooling water mass flow rate, for the upper most heat exchanger (HE_7) in the condenser section. The heat transfer coefficient profile follows a similar trend to that in Figure 5-12(b). The heat transfer coefficient peaks at approximately 150 W/m^{2}K at 30% power, 169 W/m^{2}K at 50% power, 205 W/m^{2}K at 70% power and 225 W/m^{2}K at full power.

Figure 5-13(c) shows the theoretically determined heat transfer coefficients, for single to two-phase flow operating mode, for the upper-most heat exchanger in the condenser section. In the single phase region, the heat transfer coefficient rises steadily in three distinct steps. The heat transfer coefficient peaks at approximately 48 W/m^{2}K at 30% power, 115 W/m^{2}K at 50% power and 167 W/m^{2}K at 70% power prior to the onset of boiling.

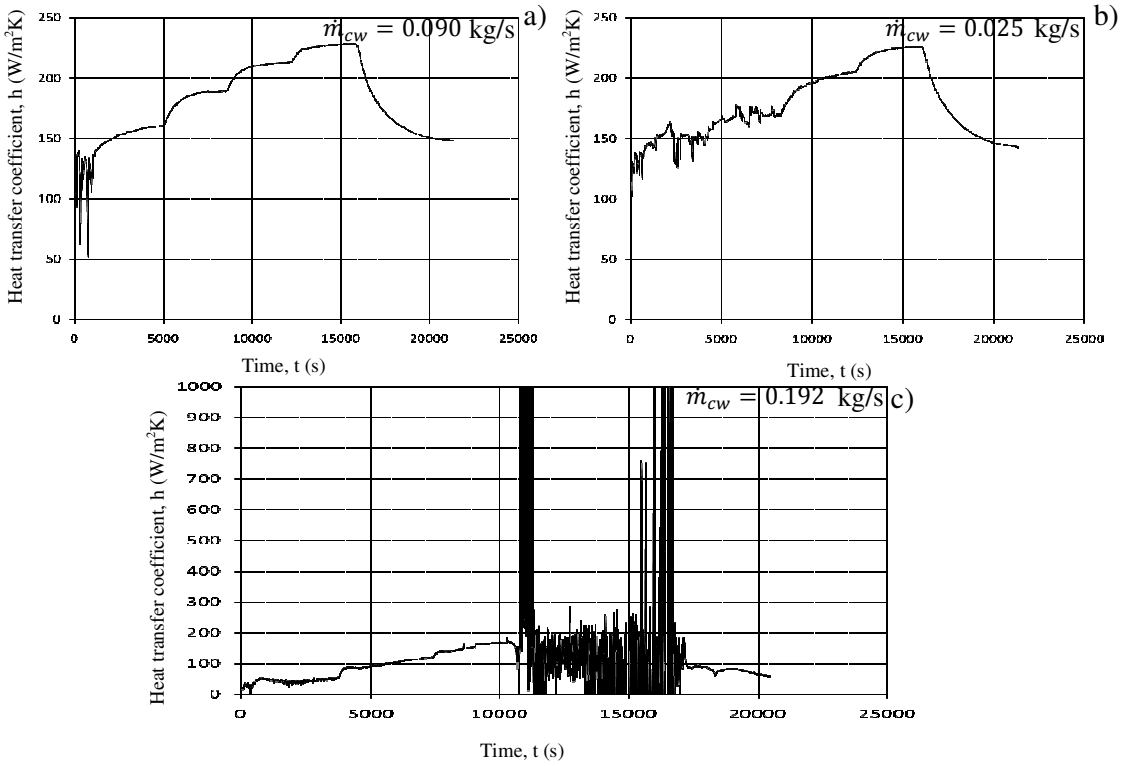

Figure 5-13: Theoretically determined inside-pipe condenser heat transfer coefficient for (a) single phase operating mode with high cooling water mass flow rate, for HE_7, (b) single phase operating mode with low cooling water mass flow rate, for HE_7, and (c) single to two-phase operating mode, for HE_7

The two-phase condenser heat transfer coefficient follows a trend very similar to the evaporator heat transfer coefficient in Figure 5-12(c).

5.3 Comparison of Results

The experimental results, shown in Figure 5-9, Figure 5-10 and Figure 5-11, are combined with the theoretical results, shown in Figure 5-12 and Figure 5-13, and are presented in Figure 5-14 and Figure 5-15. The figures show, respectively, the inside-pipe heat transfer coefficients for the third heating section in the evaporator and the upper-most heat exchanger in the condenser section.

Figure 5-14 shows the inside-pipe evaporator heat transfer coefficients for the evaporator section for single phase flow operating mode with a high cooling water mass flow rate, Figure 5-14(a), single phase flow operating mode with a low cooling water mass flow rate, Figure 5-14(b) and single to two-phase flow operating mode, Figure 5-14(c). It is clear from the Figures 5-14(a) and (b), that the correlations chosen, grossly underestimate the heat transfer coefficients in the single phase region, despite following the same trends. The single phase correlations also do not appear capture the oscillations in the heat transfer coefficient profiles. At the onset of boiling in Figure 5-14(c), the heat transfer coefficient correlation oscillates with an amplitude far exceeding experimentally obtained values and does not follow the same trend.

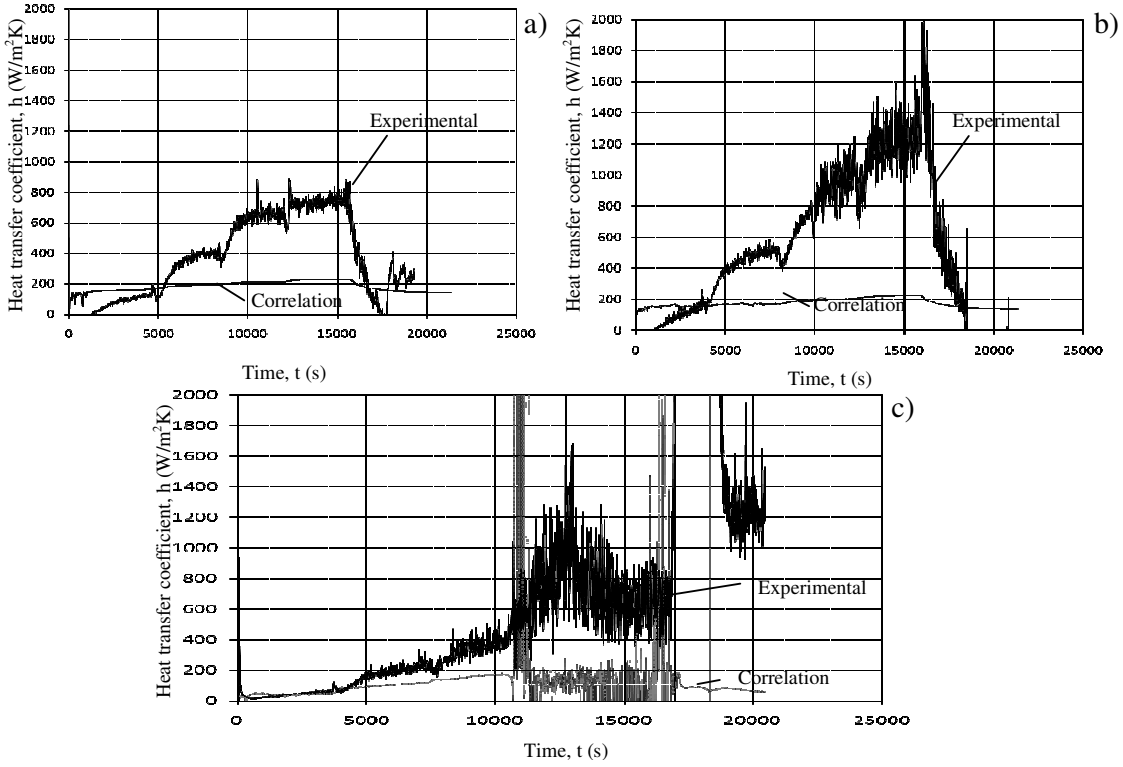

Figure 5-14: Comparison of inside-pipe evaporator heat transfer coefficient for (a) single phase operating mode with high cooling water mass flow rate, for H3, (b) single phase operating mode with low cooling water mass flow rate, for H3, and (c) single to two-phase operating mode, for H3

Figure 5-15 shows the inside-pipe condenser heat transfer coefficients for the condenser section for single phase flow operating mode with a high cooling water mass flow rate, Figure 5-15(a), single phase flow operating mode with a low cooling water mass flow rate, Figure 5-15(b) and single to two-phase flow operating mode, Figure 5-15(c). Figures 5-15(a) and (b) show that the correlations still underestimate the heat transfer coefficients in the single phase region, but definitely capture the general trend. The difference between the correlations and experimental data is less than those obtained in Figure 5-14. Whalley (1987), notes that heat transfer coefficients used in condenser sections are often up to 30% more accurate than those used in evaporator sections, though there is no apparent explanation for this. At the onset of boiling in Figure 5-15(c), the heat transfer coefficient correlation oscillates with an amplitude far exceeding experimentally obtained values and does not follow the same trend.

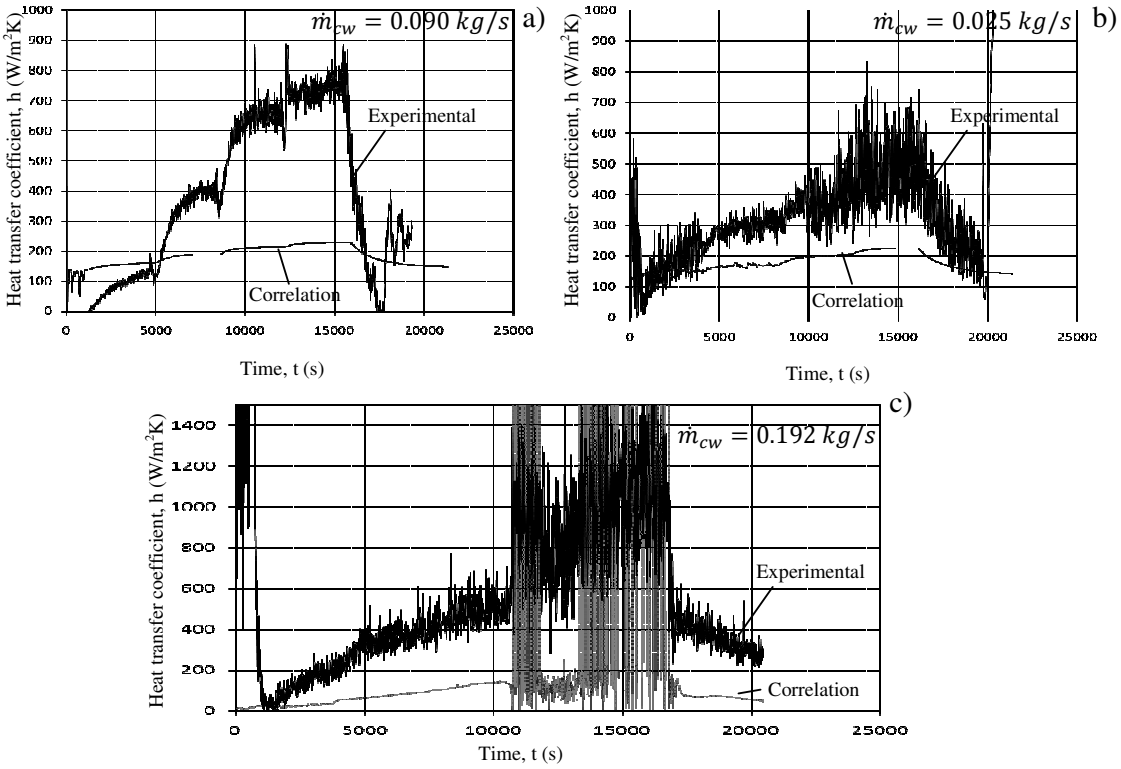

Figure 5-15: Comparison of inside-pipe condenser heat transfer coefficient for (a) single phase operating mode with high cooling water mass flow rate, for HE_7, (b) single phase operating mode with low cooling water mass flow rate, for HE_7, and (c) single to two-phase operating mode, for HE_7

The comparison of results confirms the need for the development of new inside-pipe heat transfer coefficient correlations, specific to this experiment.

6 HEAT TRANSFER CORRELATION GENERATION

In order to correlate the heat transfer coefficients determined from experimental data (as shown in Section 5.1.3), the following assumptions are made:

a) The average heat flux, $\bar{q}$, can be described by a functional dependence on certain fluid properties
b) The average heat flux is a function of the heat transfer coefficient, in the form $\bar{q} = h_{ci}(T_w - T_b)$
c) The heat transfer coefficient is a function of the Nusselt number, in the form $h = \frac{Nu_D k}{D}$

Mills (1999), suggests the following functional dependence for the average heat flux:

$$\bar{q} = f(h_{ci}) = f(Nu) = f(\Delta T, \beta, g, \rho, \mu, k, c_p, D) \quad (6\text{-}1)$$

In equation 6-1, ΔT refers to the difference between bulk fluid and wall temperatures (Mills, 1999).

Dimensional analysis of equation 6-1 identifies three independent dimensionless groups which characterize convective heat transfer (Mills, 1999):

$$Re_q = \frac{4\dot{Q}/h_{fg}}{\pi d\mu} \quad (6\text{-}2)$$

$$Pr = \frac{c_p \mu}{k} \quad (6\text{-}3)$$

$$Gr = \frac{\beta \Delta T g \rho^2 L^3}{\mu^2} \quad (6\text{-}4)$$

Fluid properties are calculated from temperature dependent functions (detailed in Appendix A). In convective heat transfer, there is a definite difference between bulk fluid and surface temperatures, creating a difficulty in selecting at which temperature the fluid properties should be calculated (Whalley, 1987; Mills, 1999). The effect of variable properties is approximately accounted for by making use of a viscosity ratio (Mills, 1999):

$$\frac{Nu}{Nu_b} = \left(\frac{\mu_s}{\mu_b}\right)^n \quad (6\text{-}5)$$

In equation 6-5, n = -0.11 for heating and cooling in laminar flow (Mills, 1999). The Nusselt numbers for the evaporator and condenser sections can thus be evaluated by calculating a Nusselt number from bulk fluid properties and adjusting it according to equation 6-5.

The Oakdale Engineering software DataFit version 8.2.79 was used to search for the correlation coefficients.

6.1 Evaporator

The evaporator heat transfer coefficients were correlated using multi-linear regression and assuming three power-law dependencies:

$$Nu_b = aRe_q^b \quad (6\text{-}6)$$

$$Nu_b = aRe_q^b Pr^c \quad (6\text{-}7)$$

$$Nu_b = aRe_q^b Pr^c Gr^d \quad (6\text{-}8)$$

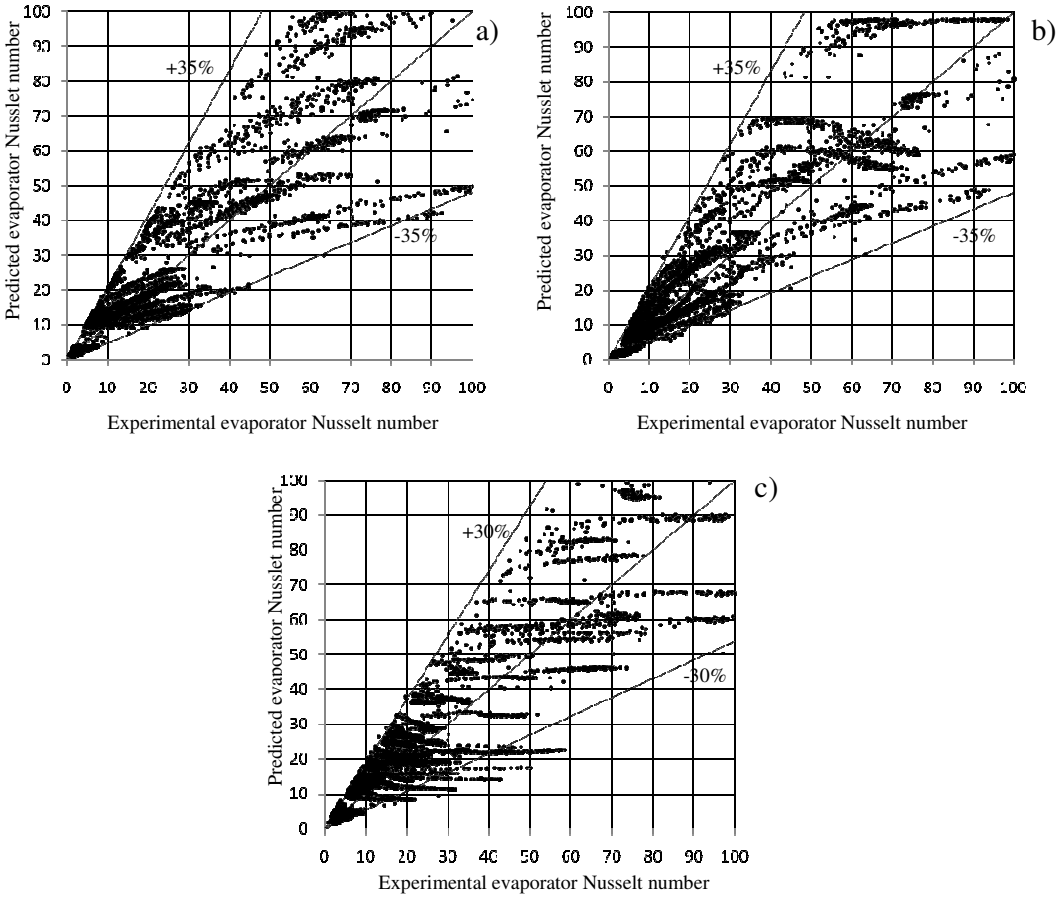

Figure 6-1: Predicted evaporator Nusselt number as a function of experimentally determined Nusselt Numbers for Single Phase Operating Mode, Equation 6-6 (a), Equation 6-7 (b) and Equation 6-8 (c)

Table 6-1: Single phase regression coefficients (evaporator)

	R^2	A	b	c	D
$Nu_b = aRe_q^b$	0.781	0.28	1.174		
$Nu_b = aRe_q^b Pr^c$	0.806	153.773	0.914	-2.813	
$Nu_b = aRe_q^b Pr^c Gr^d$	0.853	1.3×10^8	1.954	0.34	-0.835

The dimensionless groups were averaged over 60 seconds, to decrease the oscillatory peaks, yielding 5783 separate data points to which equations 6-6 to 6-8 were correlated to 99% confidence intervals. Table 6-1 shows the resulting single phase regression coefficients and correlation coefficients.

The experimental Nusselt numbers were calculated from experimentally determined evaporator heat transfer coefficients (as detailed in section 5.1.3.1), using equation 6-9. Figure 6-1 shows the predicted condenser Nusselt numbers (evaluated using equations 6-6 to 6-8) as a function of the experimentally determined Nusselt numbers. Figure 6-1(a) shows equation 6-6, $Nu_b = aRe_q^b$, as a function of experimental values. 56.73 % of the data falls within ± 35% deviation levels. The average error, for this correlation is 34.92 %. Figure 6-1(b) shows that, using equation 6-7, $Nu_b = aRe_q^b Pr^c$only 54.03 % of the data falls within ± 35% deviation levels. The average error, for this correlation, is 34.83 %. Although the correlation coefficient is higher and the average error is lower than those obtained using equation 6-6, this correlation is considered a less suitable fit because of the larger scatter in the error percentages. Figure 6-1(c) shows that equation 6-8, $Nu_b = aRe_q^b Pr^c Gr^d$, corresponds reasonably well to experimental values. 61.26 % of the data falls within ± 30% deviation levels. The average error, for this correlation, is 31.76 %. The combination of high correlation coefficient, low average error and low error scatter make this correlation the most suitable fit.

6.2 Condenser

Table 6-2: Single phase regression coefficients (condenser)

	R^2	a	b	C	d
$Nu_b = aRe_q^b$	0.877	5.417	0.481		
$Nu_b = aRe_q^b Pr^c$	0.902	0.579	0.538	1.094	
$Nu_b = aRe_q^b Pr^c Gr^d$	0.893	1.253	0.576	1.187	-0.042

The dimensionless groups were averaged over 60 seconds, to decrease the oscillatory peaks, yielding 9215 separate data points to which equations 6-6 to 6-8 were correlated to 99% confidence intervals. Table 6-2 shows the resulting single phase regression coefficients and correlation coefficients. The experimental Nusselt numbers were calculated from experimentally determined condenser heat transfer coefficients (as detailed in section 5.1.3.2), using equation 6-10. Figure 6-2 shows the predicted condenser Nusselt numbers (evaluated using equations 6-6 to 6-8) as a function of the experimentally determined Nusselt numbers. Figure 6-2(a) shows that equation 6-6, $\boldsymbol{Nu_b = aRe_q^b}$, corresponds reasonably well to experimental values. 64.23 % of the data falls within ± 20% deviation levels and a further 17 % falls within ± 30% deviation levels. The average error, for this correlation, is 16.95 %. Figure 6-2(b) shows that equation 6-7, $\boldsymbol{Nu_b = aRe_q^b Pr^c}$, corresponds slightly better to experimental values. 64.85 % of the data falls within ± 20% deviation levels and a further 18.15 % falls within ± 30% deviation levels. The average error, for this correlation, is 16.95 %. Figure 6-2(c) shows that

equation 6-8, $\boldsymbol{Nu_b = aRe_q^b Pr^c Gr^d}$, corresponds reasonably well to experimental values. 67.16 % of the data falls within ± 20% deviation levels and a further 17.5 % falls within ± 30% deviation levels. The average error, for this correlation, is 16.77 %. The difference between the three correlations is negligible, the decision about which to use is thus made based on the correlation coefficient (R^2) values.

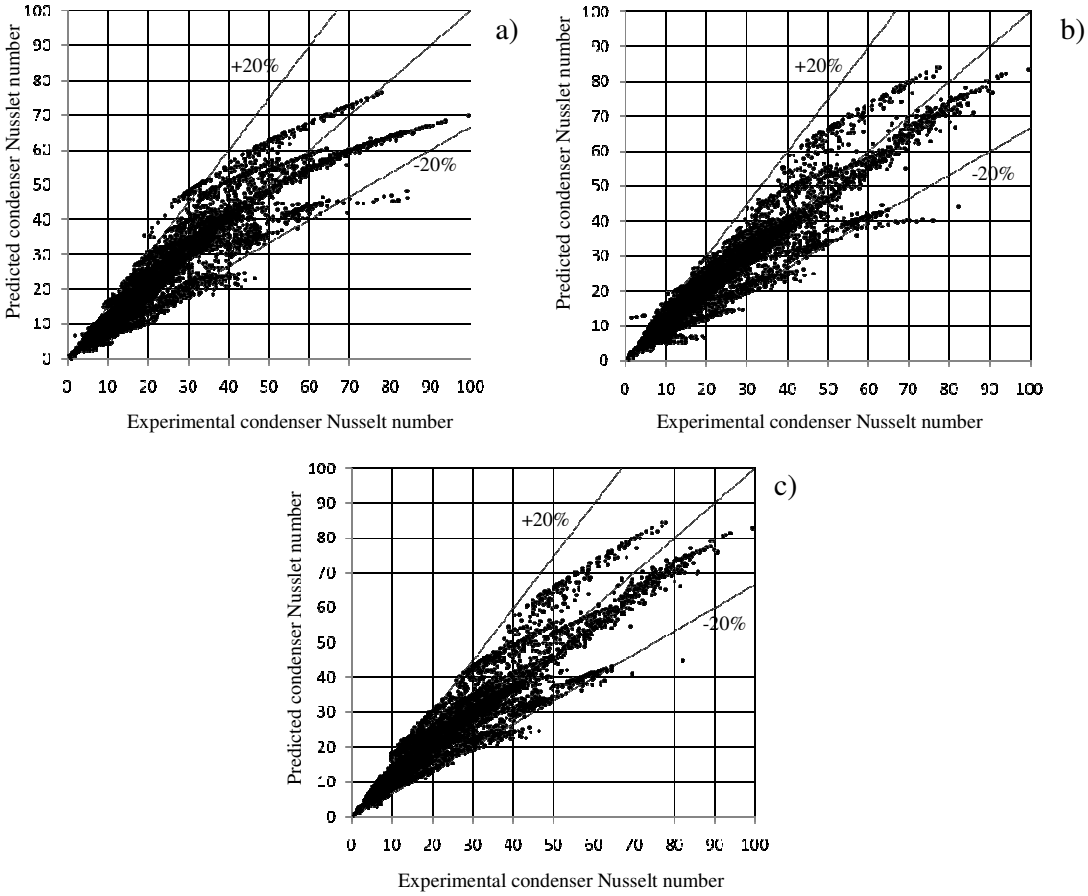

Figure 6-2: Predicted condenser Nusselt number as a function of experimentally determined Nusselt Numbers for Single Phase Operating Mode, Equation 6-6 (a), Equation 6-7 (b) and Equation 6-8 (c)

6.3 Summary

This section gives a summary of the correlations used to simulate single and two-phase inside-pipe heat transfer coefficients. For single phase flow in the evaporator section, the power law correlation, generated using 5783 experimental data points, is used to calculate the bulk Nusselt number:

$$Nu_b = 1.3\text{x}10^{8} Re_q^{1.954} Pr^{0.340} Gr^{-0.835} \quad (6\text{-}8)$$

The average single phase Nusselt number is calculated from adjusting equation 6-8 using the viscosity ratio:

$$\frac{Nu}{Nu_b} = \left(\frac{\mu_s}{\mu_b}\right)^{-0.11} \quad (6\text{-}5)$$

The single phase inside-pipe evaporator heat transfer coefficient is then calculated using:

$$h_{e,i} = \frac{Nu\, k_l}{D} \quad (2\text{-}40)$$

For two-phase boiling, Chen's correlation (as given by Whalley, 1987) is used:

$$h = h_{NB} + h_{FC} = Sh_{FZ} + Fh_l \quad (6\text{-}11)$$

In equation 3-34, h_l is the researcher's generated single phase inside-pipe evaporator heat transfer coefficient.

For single phase flow in the condenser section, the power law correlation, generated using 9215 experimental data points, will be used to calculate the bulk Nusselt number:

$$Nu_b = 0.579 Re_q^{0.538} Pr^{1.094} \quad (6\text{-}7)$$

The single phase inside-pipe condenser heat transfer coefficient is calculated using:

$$h_{c,i} = \frac{Nu\, k_l}{D} \quad (2\text{-}40)$$

In equation 2-40, *Nu* is the average fluid Nusselt number calculated from bulk fluid Nusselt number (equation 6-7) adjusted with the viscosity ratio.

For two-phase condensation, the correlation proposed by Shah (1989) is used:

$$\frac{h}{h_{lo}} = (1-x)^{0.8} + \frac{3.8 \cdot x^{0.76} \cdot (1-x)^{0.04}}{P_r^{0.38}} \quad (2\text{-}83)$$

In equation 2-83, h_{lo} is the researcher's generated single phase inside-pipe condenser heat transfer coefficient.

6.4 Comparison to Experimental Results

The correlations identified in the previous section, were used in the mathematical model detailed in section 3, with the experimental temperatures and mass flow rates used as input variables. The resulting heat transfer coefficient profiles are compared to experimental profiles (as detailed in section 5.1.3) in this section.

Figure 6-3 shows the inside-pipe heat transfer coefficients for the evaporator section for single phase flow operating mode with a high cooling water mass flow rate, Figure 6-3(a), single phase flow operating mode with a low cooling water mass flow rate, Figure 6-3(b) and single to two-phase flow operating mode, Figure 6-3(c).

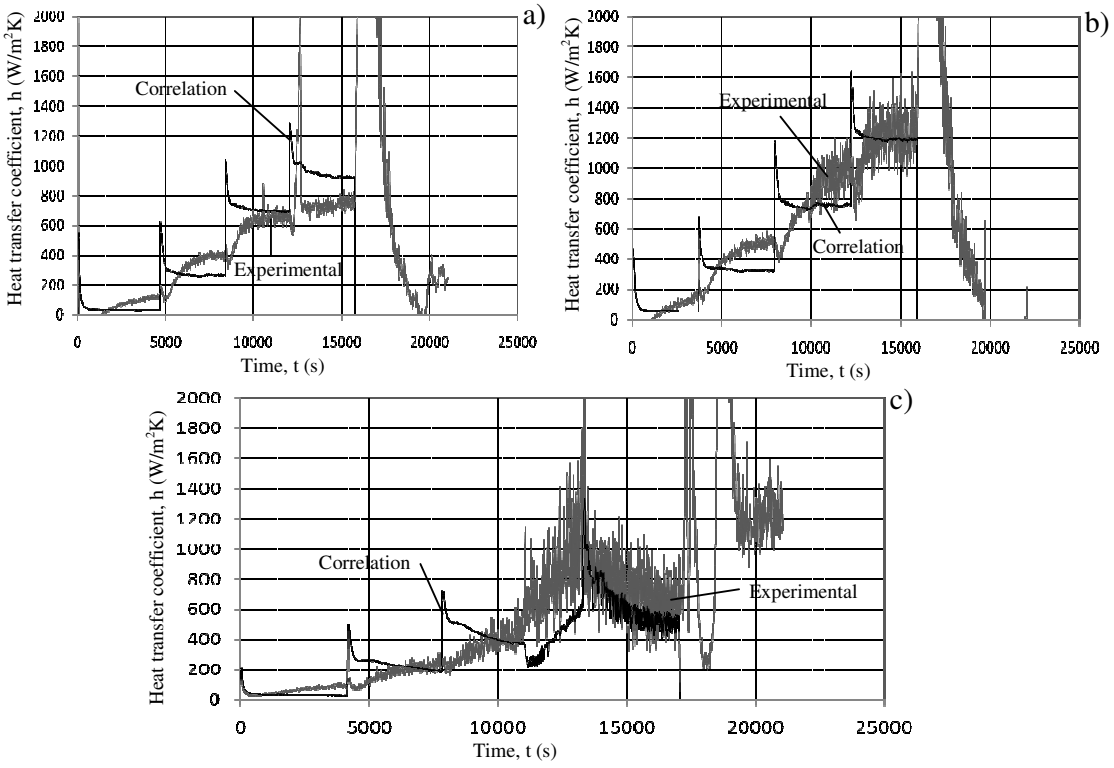

Figure 6-3: Comparison of inside-pipe evaporator heat transfer coefficient for (a) single phase operating mode with high cooling water mass flow rate, for H3, (b) single phase operating mode with low cooling water mass flow rate, for H3, and (c) single to two-phase operating mode, for H3

Figure 6-3 shows that the inside-pipe evaporator heat transfer coefficient correlations, in the single phase region, rise in distinct steps corresponding to the increases in power input. Contrary to the experimental results, these steps show an initial peak in heat transfer coefficient value, which decreases steadily until a plateau is neared as the system approaches thermal equilibrium. This behaviour can be explained by the use of electrical input power, as opposed to thermal energy transferred from the heating elements to the working fluid, in the Reynolds number (Re_q in equation 6-8). The thermal energy transferred to the working fluid increases steadily from the previous constant electrical power input level, until it approaches a plateau value equal to the current electrical power level (less minor losses to the environment) as the system reaches thermal equilibrium. This corresponds to the trend in the experimentally determined heat transfer coefficients and would thus (if used in the Reynolds number) yield a correlation which also corresponds to the same trend. Using the thermal heat transferred, in this case, is impossible as it is not measured independently and thus must be calculated using the inside-pipe evaporator heat transfer coefficient. Despite this disadvantage of the correlation, the plateau values correspond closely to those of the experimentally determined heat transfer coefficients.

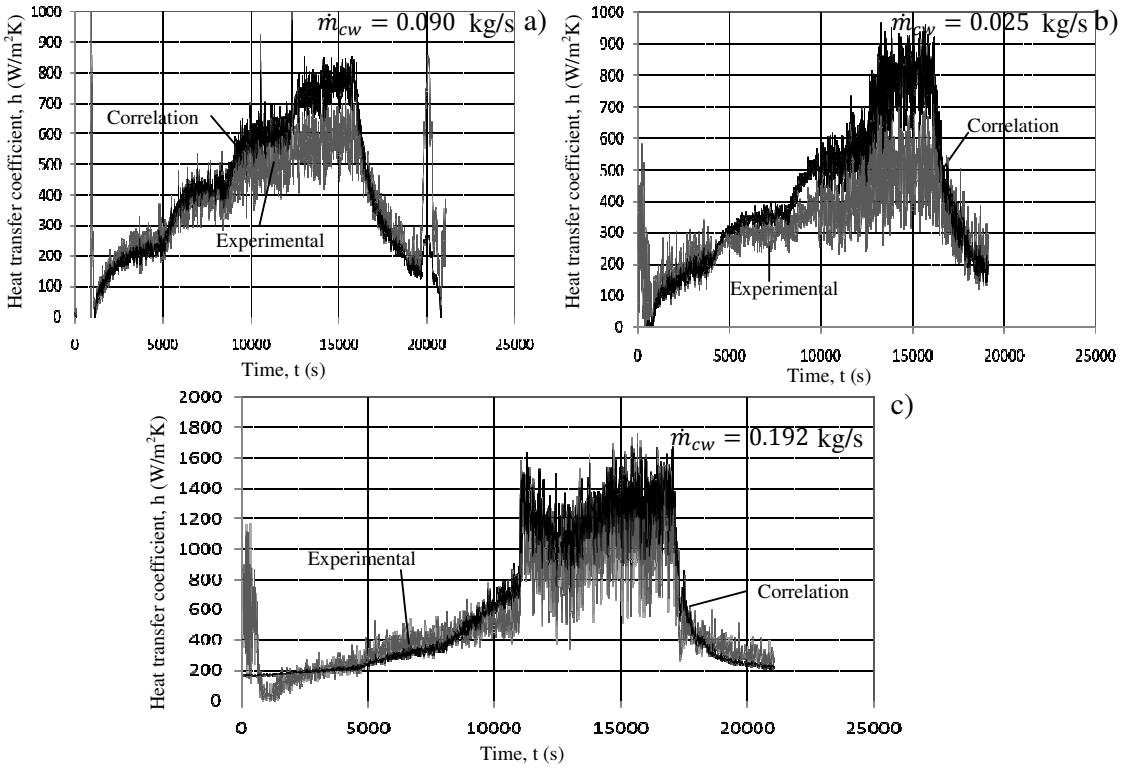

Figure 6-4: Comparison of inside-pipe condenser heat transfer coefficient for (a) single phase operating mode with high cooling water mass flow rate, for HE_7, (b) single phase operating mode with low cooling water mass flow rate, for HE_7, and (c) single to two-phase operating mode, for HE_7

The inside-pipe condenser heat transfer coefficient correlation depicts trends almost identical to those exhibited by the experimental data. During single phase operation, slight discrepancies in maximum values occur at high power input levels and low cooling water mass flow rates, as seen in Figure 6-4(a) and (b). After the onset of nucleate boiling in Figure 6-4(c), the correlation oscillates with a frequency and magnitude very closely resembling the experimental values.

The comparisons show that the generated single phase correlations, in conjunction with established two-phase heat transfer coefficient correlations, more accurately predict inside-pipe heat transfer coefficients than single phase correlations obtained from literature.

7 DISCUSSION AND CONCLUSIONS

A literature review identified several Generation IV nuclear reactors which employ passive safety systems. All the Generation IV reactors currently under development implement a passive containment heat removal system and use gravity drain tanks as well as isolation condensers to maintain core and fuel integrity during LOCA conditions. In comparison, the nature of the TRISO particle in the PBMR design allows very high temperature operation without loss in fuel integrity and the RCCS aids in the removal of core decay heat from the cavity between the reactor pressure vessel and the reactor containment. This eliminates the need for the gravity drain tanks and associated passive safety systems used in other Generation IV nuclear reactors.

The comparative technology literature review shows the widespread use of natural circulation in passive safety systems. The general one-dimensional two-fluid conservation equations that serve as the basis for the numerical modelling of these natural circulation loops were identified. Assumptions made include that the density within each phase and the cross-sectional area are constant. Several simplified models for two-phase flow were discussed, with specific reference to the restrictions placed on the model in order to limit the constitutive laws required, the constitutive laws required to solve the equations and the parameters calculated upon solving. A thorough understanding was attained of models used to mathematically describe natural circulation in nuclear applications, as well as highlighting the difficulties and limitations associated with each model. The separated flow model, which assumes that the gas and liquid phases flow separately, is widely used to model two-phase flow. It is not considered in this thesis as it is a 5-equation model and not often used in the nuclear industry.

The most widely used two-phase flow models in the nuclear industry are the 3-equation models. The drift flux model, developed by Zuber and Finlay (1965), was considered too complicated for this thesis. The homogenous equilibrium model, which assumes that the two fluid phases behave as a flowing mixture, was selected for the numerical simulation model.

The literature review also discussed available heat transfer coefficient correlations. The conclusion is that heat transfer coefficient correlations for natural circulation are a much contended subject. Correlations developed vary greatly and make selection of one specifically suitable for a researcher's experimental conditions difficult. This is especially true since most selections depend on the working fluid mass flow rate. Not only do heat transfer coefficients vary depending on whether the flow is laminar or turbulent, but most heat transfer coefficients are only valid in a specific mass flow rate range. Little or no heat transfer coefficient correlations exist, in available literature, for single phase flow in water at very low mass flow rates. Mills (1999) shows, graphically, that large deviations occur at low flow rates ($G < 10$ kg/m^{2}s). The correlations presented in the text show a 12.9% deviation from experimentally obtained data at flow rates

greater than 50 kg/m^{2}s. Shah (1989) stated that the correlations he developed were only tested over the flow rate range of 11 kg/m^{2}s < G < 211 kg/m^{2}s, and their accuracy beyond that range are unknown. In many cases, when simulating natural circulation, a selection of heat transfer coefficient correlation is made and, once the experimental data is available, is adapted to more accurately represent the experimental results. Examples of this trend are plentiful in literature and are also considered common practice. Mills (1999) states that, "*Heat transfer formulas for engineering use are based on crude physical models and dimensionless analysis, with adjustments made by curve fitting experimental data."* The conclusions drawn from this are that, given the low expected working fluid mass flow rate, single phase heat transfer coefficients available in literature would not accurately predict experimental data for closed loop thermosyphons suitable for the RCCS and correlations should be developed, specifically tailored to experimental conditions.

One of the objectives of this project was to design and build a one-third-height-scale model of the RCCS. Copper piping was used, eliminating material and surface property uncertainties identified during previous projects involving experimental RCCS models which affected the accuracy of theoretical models. Several sight glasses were incorporated in the model, allowing for the visual identification of two-phase flow regimes. An orifice plate was used to measure working fluid mass flow rate, addressing a shortcoming identified by Ruppersburg (2007), allowing for forward and reverse flow measurement. The orifice plate, thermocouples and pipe-in-pipe heat exchangers were calibrated in-situ to minimize experimental error and aid repeatability.

Twelve experiments, lasting at least 5 hours each, were performed with data logging occurring every ten seconds. The results presented were limited to selected experimental results for single and two-phase flow operating modes due to the large number of data points obtained. Error analyses and repeatability of experimental measurements for single and two-phase operating modes as well as cooling water mass flow rates were performed, showing that the experimental results are well repeated.

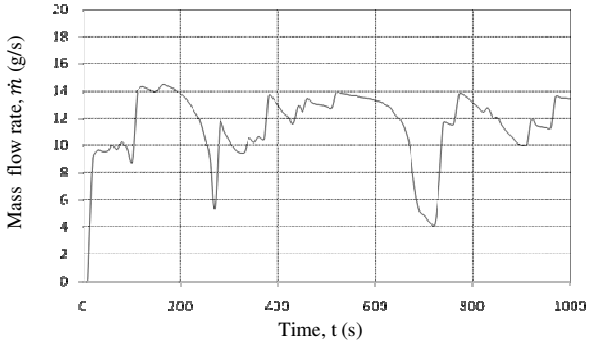

Figure 7-1: Single phase flow operating mode working fluid mass flow rate

During single phase experimentation, start-up oscillations in the working fluid mass flow rate were identified. Figure 7-1 shows an enlargement of Figure 5-1(d) from 0 to 1000 s. These oscillations, typical of natural circulation loop start-up, are caused by the working fluid buoyancy force overcoming the static friction forces and gradually stabilize. The oscillations are considered instabilities in the system and could cause the working fluid to overheat on reactor start-up. To prevent this possibility, the reactor should be sequentially started up.

The experimental results were used to mathematically determine the experimental inside-pipe heat transfer coefficients for both the evaporator and condenser sections. Trends were identified and the general behaviour of the profiles was thoroughly explained. The evaporator and condenser heat transfer coefficients follow similar trends, which is to be expected. The condenser heat transfer coefficients have slightly lower plateau values in the single phase region with a higher oscillatory amplitude. This is due to the coefficients' dependence on the cooling water temperatures which oscillate with relatively large amplitude. In the two-phase region, where nucleate boiling is fully saturated, the condenser heat transfer coefficients are much higher than those of the evaporator section. This can be explained by the dependency of the evaporator heat transfer coefficient on the temperature difference between the tube wall and the bulk fluid. As boiling becomes saturated, this temperature difference becomes very small, resulting in a lower heat transfer coefficient value.

The RCCS was modelled as a one-dimensional system, making several assumptions: the thermodynamic process is quasi-static; compressibility effects due to heating or cooling of the liquid and vapour phases are negligible; and the flow is one-dimensional. Correlations for the friction factor, heat transfer coefficient, void fraction and two-phase frictional multiplier were identified. Due to the lack of relevant natural flow correlations, most of the correlations used are for forced flow. This introduces room for over- or under- prediction of the model as the working fluid flow might not be fully developed at all times.

The theoretical heat transfer coefficients were calculated using natural circulation mathematical modelling theory and heat transfer coefficient correlations identified as viable in the literature review. Fluid parameters were evaluated using experimentally determined temperatures and mass flow rates. The resulting heat transfer coefficient profiles were compared to experimentally determined profiles, showing that single phase heat transfer coefficient correlations identified in available literature, do not accurately predict experimental values and reaffirming the need to develop experiment specific heat transfer coefficient correlations.

In order to correlate the heat transfer coefficients determined from experimental data, it was assumed that the average heat flux can be described by a functional dependence on certain fluid properties, the average heat flux is directly proportional to the heat transfer coefficient and that the heat transfer coefficient is

a function of the Nusselt number. The Nusselt numbers for the evaporator and condenser sections were evaluated by calculating a Nusselt number correlation from bulk fluid properties and adjusting it with a viscosity ratio.

The heat transfer coefficients were correlated using multi-linear regression and assuming three power-law dependencies. The dimensionless groups were averaged over 60 seconds, to decrease the oscillatory peaks, yielding 5783 separate data points for the evaporator and 9215 for the condenser section. The three power-law dependencies were correlated to 99% confidence intervals yielding correlations for the single phase inside-pipe heat transfer coefficient for both the condenser and evaporator sections with an average error of less than 30% and a regression coefficients higher than 0.9.

The generated correlations, along with identified and established two-phase heat transfer coefficient correlations, were used in a mathematical model, with experimental mass flow rates and temperatures used as input variables, to generate theoretical heat transfer coefficient profiles. These were compared to the experimentally determined heat transfer coefficients. The generated correlations offer a more accurate prediction of the experimental heat transfer coefficients. It must be noted that the generated single phase inside-pipe heat transfer coefficient correlations are only valid for the specific conditions under which they were developed i.e.: $\dot{m}_{cw,1} \leq 0.085$ kg/s, $\dot{m}_{cw,2} \leq 0.106$ kg/s, $\dot{m}_{cw,3} \leq 0.093$ kg/s, $\dot{m}_{cw,4} \leq 0.113$ kg/s, $\dot{m}_{cw,5} \leq 0.116$ kg/s, $\dot{m}_{cw,6} \leq 0.089$ kg/s, $\dot{m}_{cw,7} \leq 0.195$ kg/s, $\dot{m} \leq 14$ g/s. If testing of the experimental system is required beyond this range, the researcher suggests that the heat transfer coefficients should be re-generated for the new conditions.

The generated heat transfer coefficient correlations, when used in the theoretical model, allow for a close approximation of the experimental working fluid mass flow rate as depicted in figure 7-2.

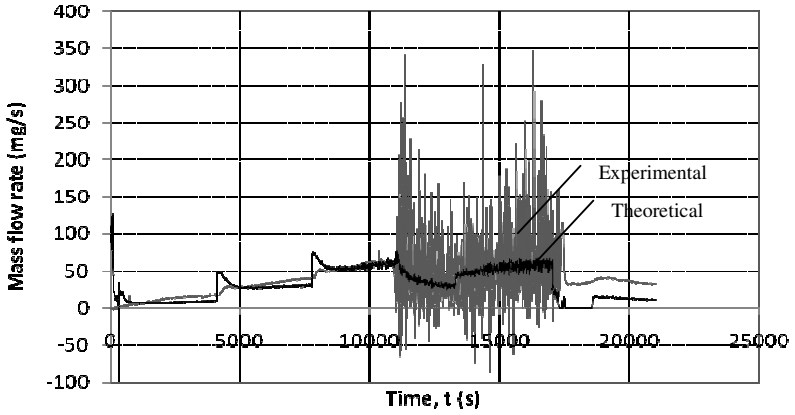

Figure 7-2: Comparison of experimentally and theoretically determined working fluid mass flow rate for single to two-phase operation case

The discrepancy in single phase trends, found at the start of each power increase step, is explained by the single phase inside-pipe evaporator heat transfer coefficients being dependent on the electrical input and thus yielding an incorrect initial trend as discussed in section 6.4. Although large differences between experimentally and theoretically determined mass flow rates occur during two-phase operation, figure 7-2 clearly shows that the theoretical profile closely approximates the average experimental data in this region. The conclusion is that the theoretical model, in conjunction with the generated heat transfer coefficient correlations, is capable of closely predicting the experimental model behaviour.

The generated theoretical model is easily adaptable to simulating a full scale model of the RCCS as the mathematical principles are identical (assuming the full scale model also consists of constant, circular diameter piping). In order to adapt the model, the geometric properties of the simulation must be updated to correspond to the full scale model. The process followed to generate heat transfer coefficient correlations should also be followed when testing a full scale RCCS model.

Shortcomings identified in the theoretical model are:

- Using the electrical power input in Re_q in the generated evaporator heat transfer coefficient correlations yields an inaccurate trend in the results.
- General frictional loss coefficient correlations were used rather than correlations specific to the various flow patterns.
- The vast amount of variables and temperature dependant functions used limited the choice of programming language for a computer model. QuickBasic allowed for acceptable processing speed without simplifying these functions.
- One-dimensional analysis was used. Though analysis in more dimensions could offer more accurate results, the trade off is more complicated correlations, more assumptions, more restrictions and constitutive laws required etc. Not only would this exponentially increase the processing time, it also increases the room for error. The vast amount of literature available and thorough understanding of one-dimensional analysis allows the researcher to focus on heat transfer coefficient correlations in the theoretical modelling.

Shortcoming identified in the experimental setup:

- It was not possible to accurately measure the heat transferred from the fin to the working fluid.
- Data was logged every 10 seconds. Though this is adequate for single phase flow, transient behaviour and oscillations are not adequately captured during two-phase flow.
- The effect of inferior or lower grade materials was not initially taken into account. Much time was lost in testing individual copper sections of the experimental loop to identify micro-cracks and pores, marking them and welding or soldering them closed. This time could have been saved in ensuring the correct grade of copper was used.

- The current position of the feedwater tap for the condenser section is on the solar lab roof. This is due to water pressure and general plumbing problems discovered in the laboratory where the experiment is situated. The system works adequately, but it is inconvenient to leave the experiment unattended to open and close the feedwater tap. This problem was addressed by placing a valve at the outlet of each pipe-in-pipe heat exchanger outer pipe, to control the cooling water mass flow rate independently and on location. This limited the need to leave the laboratory during experimentation, but ideally the feedwater tap should be moved to on location.
- The use of glass in the heat exchangers presented several difficulties. Because the glass is hand-made to specific dimensions, the inlets and outlets are not perfectly circular. This resulted in problems with attaining an air- and water-tight seal with the copper pipe which was later addressed by using larger diameter silicon o-rings and vacuum grease. Problems also arose with consistency in pipe diameter, making it difficult to insert connectors and O-rings and attach glass pipes to copper pipes without breaking or cracking the glass. At high temperatures and low cooling water mass flow rates, the cyclic thermal expansion and contraction of the glass caused several cracks.
- The temperature of the working fluid was only measured at the four corners of the experimental model. Though this was considered enough at the time of design, during theoretical analysis assumptions have to be made about the temperature distribution along the length of the thermosyphon which cannot be verified.
- Heat pipe mode was not addressed at all in this thesis. The air release valve at the top of the experimental loop failed under vacuum and several small leaks were identified which, due to time constraints, were not fully attended to.

In conclusion the generated correlations can predict the single phase inside-pipe heat transfer coefficients fairly well. Although heat pipe mode was not investigated, the experimental results show that, in single phase operating mode, the experimental model can remove 7311.2 kW at full input power. In single to two-phase operating mode, the experimental model removes a maximum of 9306.1 kW. Although the single to two-phase operating mode removes more heat, the single phase operating mode is more than capable of keeping the lower leg of the thermosyphon below the specified 65 °C and there are far fewer instabilities and uncertainties associated with single phase flow. The results make a strong argument for the use of single phase natural circulation thermosyphons in the RCCS.

8 RECOMMENDATIONS

8.1 Heat Exchangers

The initial choice of glass for the outer pipe of the heat exchanger was made in order to facilitate visual identification and confirmation, amongst others: that the heat exchanger wetted length, that adequate turbulence in the cooling water, that no air bubbles exist in the cooling water and that boiling does not occur. The advantages of glass pipes are far outweighed by the machining, manufacturing, assembly and handling difficulties experienced. For this specific experiment, it is recommended that the glass pipes be replaced by stainless steel heat exchangers which can be welded in place, eliminating the need for o-rings, seals and vacuum grease. Whether air bubbles are present in the cooling water can still be visually determined as the connecting polyurethane piping is transparent.

The current position of the feedwater tap for the condenser section should be re-evaluated. If it is impossible to obtain the necessary water pressure inside the laboratory, the option of using a recirculation pump (operated from within the laboratory) should be investigated.

8.2 Mass Flow Rate Measurement

Experimental data was only logged once every 10 seconds. It should be investigated whether an add-on program exists (or could be developed) for the Agilent benchlogger software which allows the sampling rate to be altered mid-experiment.

8.3 Temperature Measurement

In order to fully describe the temperature profile along the length of the thermosyphon, more thermocouples should be placed in a position to measure bulk fluid temperature. The addition of more thermocouples would require the purchase of another data card for the data logger as well as compound the existing electrical interference which causes oscillations in some of the measurements. A careful analysis should be made of how many thermocouples would adequately describe the temperature profile whilst keeping the electrical interference to a minimum. The possibility of electrically shielding thermocouples should also be investigated.

8.4 Experimentation

Heat pipe operation mode, fill ratios and associated instabilities should be fully addressed. An attempt must be made to gauge the effect of tube diameter, tube shape, loop height, loop width, ratio of tube length to diameter, type of working fluid, working fluid fill ratio and fin size on the inside-pipe heat transfer coefficient.

8.5 Mathematical Model

Placing more thermocouples along the length of the thermosyphon would allow for a more accurate measurement of heat lost to the environment. An energy balance could then be performed, allowing for the relatively accurate prediction of thermal energy transferred from the electrical heating elements to the bulk working fluid, based on the heat removed in the condenser section and heat lost to the environment. This calculated thermal energy transferred to the working fluid could then be used in the correlations in Re_q, which would yield trends in the correlations profile similar to those obtained in the experimental evaporator inside-pipe heat transfer coefficients.

The possible use of flow pattern specific frictional loss coefficients should be investigated.

There is much difficulty associated with programming this type of mathematical modelling and the vast amount of variables and temperature dependant functions required to generate a mathematical model. The development (or purchase) of a platform software (similar to RELAP5), allowing user selection or input of e.g. heat transfer coefficient correlations, thermal heat input profiles, number of heat exchangers, frictional loss coefficients, solution method etc. should seriously be considered. A lot of time is wasted on developing computer models from first principles by each researcher working on a similar experimental model.

The possibility of using CFD software to analyse the flow inside the thermosyphon should be investigated.

8.6 Heat Transfer Coefficient Correlations

It is recommended that instead of selecting existing heat transfer coefficient correlations from literature, researchers should generate correlations specific to their experimental systems.

9 REFERENCES

Beckwoth, T., Maragoni, R., & Lienhard, J. (1993). *Mechanical Measurements, Fifth edition.* Addison-Wesley Publishing Company.

Brennen, C. (2005). *Fundamentals of Multiphase Flow.* Cambridge University Press.

BSI. (1981). *BS 1042: Measurement of Flow in Closed Conduits, Part 1: Pressure Differential Devices.* British Standards Institution .

Carey, V. (1992). *Liquid-Vapour Phase Change Phenomena: An Introduction to the Thermodynamics of Vaporization and Condensation Processes in Heat Transfer Equipment.* Washington: Hemisphere Publishing Corperation.

Çengel, Y. (2003). *Heat Transfer A Practical Approach Second Edition.* New York: McGraw-Hill Companies, Inc.

Cengel, Y. and Boles, M. (2002). *Thermodynamics, An Engineering Approach 4th Edition.* Singapore: McGraw Hill.

Chan, P. and Nakayama, P. (1990). A Two-Dimensional Analysis of In-Vessel Buoancy Driven Flows During a Degraded Core Scenario. *Nuclear Engineering and Design Volume 122 Issues 1-3* , 273-286.

Chen, S., Gerner, F., & Tien, C. (1987). General Film Condensation cCorrelations. *Experimental Heat Transfer, Vol. 1* , 93-107.

Collier, J., and Thome, J. (1994). *Convective Boiling and Bondensation, 3rd ed.* Oxford: Clarendon Press.

Crowe, C., Elger, D., & Roberson, J. (2001). *Engineering Fluid Mechanics 7th Edition.* New York: John Wiley & Sons. Inc.

Dobson, R., and Ruppersburg, J. (2006). Experimental Evaluation of the Flow and Heat Transfer in a Closed Loop Thermosyphon. *JESA* .

Dube, V., Akbarzadeh, A., & Andrews, J. (2004). The Effect of Non-Condensable Gases on the Performance of Loop Thermosyphon Heat Exchangers. *Applied Thermal Engineering Vol 24* , 2439-2451.

Dulera, I., and Sinha, R. (2008). High Temperature Reactors. *Journal of Nuclear Materials 383* , 183-188.

Eskom. (2008). *Nuclear Power- Pebble Bed Reactor Technology.* Retrieved January 2008, from Eskom:

http://www.eskom.co.za/nuclear_energy/pebble_bed/pebble_bed.html

Farlow, S. J. (1993). *Partial Differential Equations for Scientists and Engineers.* New York: Dover Publications Inc.

Fennern, L. (2006, September 16). *ESBWR Seminar - Reactor, Core & Neutronics.* Retrieved February 2010, from U.S. Department of Energy: http://www.ne.doe.gov/

Framatome ANP GmbH. (2002). *SWR 1000 The Boiling Water Reactor with a New Safety Concept.* Retrieved 2009, from Areva: http://www.areva.com

General Electric Hitachi Nuclear Energy. (2008). *GEA-14429G: General Electric - ESBWR Technology Fact Sheet.* General Electric Company.

Greif, R. (1988). Natural Circulation Loops. *Journal of Heat Transfer Vol 110*, 1243-1258.

Handra. (2008). *Application and Economic Feasibility of Functionally Graded Composite for Lead-Bismoth Service.* Massachusetts Institute of Technology.

Hibiki, T. and Ishii, M. (2003). One-Dimensional Drift-Flux Model and the Constitutive Equations for Relative Motion Between the Phases in Various Two-Phase Reqions. *International Journal of Heat and Mass Transfer vol 46* , 4935-4948.

International Atomic Energy Agency. (2000). *IAEA-TECDOC-1281: Natural Circulation Data and Methods for Advanced Water Cooled Nuclear Power Plant Designs.* Vienna: IAEA.

International Atomic Energy Agency. (1991). *IAEA-TECDOC-626: Safety Related Terms for Advanced Nuclear Plants.* Vienna: IAEA.

International Atomic Energy Agency. (1996). *IAEA-TECDOC-872: Progress in Design, Research and Development, and Testing of Safety Systems for Advanced Water Cooled Reactors.* Vienna: IAEA.

International Atomic Energy Agency. (2006). *IAEA-TECDOC-DRAFT: Description of Natural Circulation and Passive Safety Systems in Water Cooled Nuclear Power Plants - CRP on Natural Circulation Phenomena, Modeling and Reliability of Passive Systems that Utilize Natural Circulation.* IAEA.

International Atomic Energy Agency. (2005). *Natural Circulation in Water Cooled Power Plants: Phenomena, Models, and Methodology for System Reliability Assessments.* Vienna: IAEA.

ISO. (1988). *ISO 7005-3: Metallic Flanges -- Part 3: Copper Alloy and Composite Flanges.* International Organization for Standardization.

Khatib-Rahbar, M. E. (2003). A Small Modular Advanced Reactor Technology (SMART). *Proceedings of the 2003 International Congress on Advances in Nuclear Power Plants.* Cordoba, Spain: ICAPP.

Liu, Z. and Winterton, R. (1991). A General Correlation for Saturated and Subcooled Flow Boiling in Tubes and Annuli, Based on a Nucleate Pool Boiling Equation. *International Journal of Heat and Mass Transfer, Vol. 34* , 2759-2766.

Loubser, J. (2008, April). Electronic Techinician for Unitemp cc. johanl@unitemp.com, cell 083-225-4740.

Matzner, D. (2004). PBMR Existing and Future R&D Test Facilities. *2nd International Topical Meeting on High Temperature Reactor Technology* , pp. 1-26, Beijing.

Mills, A. (1999). *Heat Transfer, 2nd ed.* Upper Saddle River: Prentice Hall.

Mitstemubishi Heavy Industries LTD. (2010). *APWR Configuration of Basic System*. Retrieved 2009, from Mitsubishi Heavy Industries: http://www.mhi.co.jp

Modro, S., Fisher, J., Weaver, K., Babka, P., Reyes, J., Groome, J., et al. (2002). Generation-IV Multi-Application Small Light Water Reactor (MASLWR). *Tenth International Conference on Nuclear Energy.* Arlington Virginia, USA.

Nayak, A., Vijayan, P., Saha, D., Cenkat Rap, V., & Aritomi, M. (1998). Linear Analysis of Thermo-Hydraulic Instabilitied of the Advanced Heavy Water Reactor (AHWR). *Journal of Nuclear Science and Technology vol 35* , 768-778.

Ohashi, K., Hayakawa, H., Yamada, M., Hayashi, T., & Ishii, T. (1998). Preliminary Study on the Application of the Heat Pipe to the Passive Decay Heat Removal System of the Modular HTR. *Progress in Nuclear Energy, Vol. 32, No. 3-4* , 587-594.

Organisation for Economic Cooperation and Development and Nuclear Energy Agency. (2010). *The PBMR-400 Core Design*. Retrieved 2010, from OECD/NEA PBMR Coupled Neutronics/Thermal-Hydraulics Transients Benchmark : htt[://www.nea.fr/

PBMR (Pty) Ltd. (2009). *Technology*. Retrieved January 2009, from Pebble Bed Modular Reactor: http://www.pbmr.co.za

Reyes, J. (2007). *Governing Equations in Two-Phase Fluid Natural Circulation.* Vienna: International Atomic Energy Agency.

Ruppersberg, J. (2007). *MScEng Thesis: Transient and Scaling Effects in Single and Two Phase Natural Circulation Thermosyphon Loops Suitable for the Reactor Cavity Cooling of a Pebble Bed Modular Reactor.* University of Stellenbosch.

Saha, D. (June 2009). Local Phenomena Associated With Natural Circulation. *IAEA-UNIPI Training Course on Natural Circulation Phenomena and Modelling in Water Cooled Nuclear Power Plants*, (p. Lecture Notes T4 and T5). Pisa.

Schultz, T. (2006). Westinghouse AP1000 Advanced Passive Plant. *Nuclear Engineering and Design 236* , 1547-1557.

Shah, M. (1989). A General Correlation for Heat Transfer During Film Condensation Inside Pipes. *International Journal of Heat and Mass Transfer, Vol. 22* , 547-556.

Sinha, R. and Kakodkar, A. (2005). Design and Development of the AHWR - the Indian Thorium Fuelled Innovative Nuclear Reactor. *Proceedings of GLOBAL* (p. Paper No. 15). Tsubaka, Japan: GLOBAL.

Smith, G.D. (1965). Numerical Solution of Partial Differential Equations, Oxfrod University Press.

Soliman, M., Schuster, J., & Berenson, P. (1968). A General Heat Transfer Correlation for Annular Flow Condensation. *Journal of Heat Transfer, Vol. 90* , 267-276.

Steiner, D. and Taborek, J. (1992). Flow Boiling Heat Transfer in Vertical Tubes Correlated by an Asymptotic Model. *Heat Transfer Engineering, Vol. 13, No. 2*, 43-68.

Stewart, J. (1999). *Calculus Fourth Edition.* Brooks/Cole Publishing Company.
Stosic, Z. e. (2008). Boiling Water Reactor with Innovative Safety Concept: The Generation III+ SWR-1000. *Nuclear Engineering and Design 238*, 1863-1901.

Thermal Ceramics Pty Ltd. (n.d.). *Thermal Ceramics Product Information.* Retrieved March 2009, from Thermal Ceramics: http://www.thermalceramics.com

Traviss, D., Rohsenow, W., & Baron, A. (1973). Forced Convection Condensation in Tubes: A Heat Transfer Correlation for Condenser Design. *SHRAE Transactions Vol. 79, Part 1* , 157-165.

Tujikura, Y. E. (2000). Development of Passive Safety Systems for the Next Generation PWR in Japan. *Nuclear Engineering and Design 201*, 61-70.

United States Nuclear Regulatory Commission. (2008). *Nuclear Reactor Concepts Workshop Manual: Pressurized Water Reactor (PWR) Systems.* Retrieved November 2008, from U.S.NRC: http://www.nrc.gov

van de Graaf, R., and van der Hagen, T. (1994). Two-Phase Flow Scaling Laws for a Simulated BWR Assembly. *Nuclear Engineering and Design volume 148*, 455-462.

van Staden, M. (2001). *Analysis of Effectiveness of the PBMR Cavity Cooling System.* South Africa: PBMR Ltd (Pty).

Verwey, A. (2007). *Mechanical Project 478: Passive Nuclear Reactor Cooling Using a Loop Thermosyphon.* University of Stellenbosch.

Vining, G. (1998). *Statistical Methods for Engineers.* Johannesburg: Duxbury Press.

Westinghouse Electrical Company LLC. (2007). *AP1000.* Westinghouse Graphic Services and Identity Department.

Westinghouse Electrical Company. (n.d.). *Technology Fact Sheet.* Retrieved July 2008, from Westinghouse Electrical Company: www.ap1000.westinghousenuclear.com

Whalley, P. (1987). *Boiling, Condensation and Gas-Liquid Flow.* Oxford: Clarendon Press.

White, F. (2006). *Viscous Fluid Flow 3rd Edition.* McGraw-Hill.

Wolverine Tube, Inc. (2007). *Engineering Data Book III: Chapter 12 - Two Phase Flow Patterns.* Wolverine Tube Inc.

Xinian, Z., Weijun, G., Bing, H., & Shifei, S. (2001). Transient Analyses of the Passive Residual Heat Removal System. *Nuclear Engineering and Design volume 206*, 105-111.

Yang, R., Liu, R., Zhong, Y., & Liu, T. (2006). Experimental Study on Convective Heat Transfer of Water Flow in a Heated Tube Under Natural Circulation. *Nuclear Engineering and Design, Vol. 236*, 1902-1908.

Zill, D. and Cullen, M. (2000). *Advanced Engineering Mathematics Second Edition.* Jones and Bartlett.

Zuber, N. and Findlay, J. (1965). Average Volumetric Concentration in Two-Phase Flow Systems. *Journal of Heat Transfer 87*, 453-468.

APPENDIX A: THERMOPHYSICAL PROPERTIES OF MATERIALS

A.1 Properties of Water

Thermo-physical properties of saturated water from 273.15 K to 380 K, Kröger (1998)

$$\mathbf{c_{p,v} = 1.3605 \times 10^{3} + 2.31334T - 2.46784 \times 10^{-10}T^{5} + 5.91332 \times 10^{-13}T^{6}} \quad \text{(A-1)}$$

$$\mu_v = 2.562435 \times 10^{-6} + 1.816683 \times 10^{-8}T + 2.579066 \times 10^{-11}T^2 - 1.067299 \times 10^{-14}T^3 \quad \text{(A-2)}$$

$$k_v = 1.3046 \times 10^{-2} - 3.756191 \times 10^{-5}T + 2.217964 \times 10^{-7}T^2 - 1.111562 \times 10^{-10}T^3 \quad \text{(A-3)}$$

$$\rho_v = -4.06239056 + 0.10277044T - 9.76300388 \times 10^{-4}T^2 + 4.475240795 \times 10^{-6}T^3 - 1.004596894 \times 10^{-8}T^4 + 8.9154895 \times 10^{-12}T^5 \quad \text{(A-4)}$$

$$c_{p,l} = 8.15599 \times 10^{3} - 28.0627T + 5.11283 \times 10^{-2}T^2 - 2.17582 \times 10^{-13}T^6 \quad \text{(A-5)}$$

$$\mathbf{\mu_l = 2.414 \times 10^{-5} \times 10^{247.8/(T-140)}} \quad \text{(A-6)}$$

$$k_v = -6.14255 \times 10^{-3} + 6.9962 \times 10^{-3}T - 1.01075 \times 10^{-5}T^2 + 4.74737 \times 10^{-12}T^4 \quad \text{(A-7)}$$

$$\rho_l = (1.49343 \times 10^{-3} - 3.7164 \times 10^{-6}T + 7.09782 \times 10^{-9}T^2 - 1.9032 \times 10^{-20}T^6)^{-1} \quad \text{(A-8)}$$

$$h_{fg} = 3.4831814 \times 10^{6} - 5.8627703 \times 10^{3}T + 12.139568T^2 - 1.4029043 \times 10^{-2}T^3 \quad \text{(A-9)}$$

$$T = 164.630366 + 1.832295 \times 10^{-3}P + 4.27215 \times 10^{-10}P^2 + 3.738954 \times 10^{3}P^{-1} - 7.01204 \times 10^{-5}P^{-2} + 16.161488\ln(P) - 1.437169 \times 10^{-4}P\ln(P) \quad \text{(A-10)}$$

$$\beta = -3.7603969 \times 10^{-15}T^6 + 7.2376848 \times 10^{-12}T^5 - 5.8005101 \times 10^{-9}T^4 + 2.4783008 \times 10^{-6}T^3 - 5.9555955 \times 10^{-4}T^2 + 0.07635924T - 4.0833703 \quad \text{(A-11)}$$

$$Pr_{wall} = 2.6244157 \times 10^{-12}T^6 - 6.3680073 \times 10^{-9}T^5 + 6.4093506 \times 10^{-6}T^4 - 0.0034260841T^3 + 1.0262977T^2 - 163.46148T + 10827.083 \quad \text{(A-12)}$$

A.2 Properties of Heating Elements

6 0.025 x 1.9 m Heating Elements:
Resistance = 35 Ω Rated Power Capability = 1.5 kW
2 25 x 850 mm Heating Element:
Resistance = 105 Ω Rated Power Capability = 500 W

A.3 Properties of Insulation Material

Values for density, thermal conductivity and specific heat capacity of the B64-25 Ceramic Fibre were provided by the manufacturer, Thermal Ceramics UK Ltd, through a South African distributer, Cape Refractory Industries. Emissivity values for insulation material are found in Mills (1999).

ρ = 64 kg/m^3 c = 1.13 kJ/kg.K
k = 0.07 W/m.K ε = 0.9

A.4 Properties of Copper

Values obtained for pure copper at 300K from Mills (1999)
ρ = 8933 kg/m^3 c = 0.385 kJ/kg.K
k = 401 W/m.K

A.5 Properties of Clear Polycarbonate

ρ = 64 kg/m^3 c = 1.13 kJ/kg.K
k = 0.07 W/m.K ε = 0.9

A.6 Properties of Glass

Values obtained for fused silica glass from Mills (1999)
ρ = 2220 kg/m^3 c = 0.745 kJ/kg.K
k = 1.38 W/m.K

APPENDIX B: CALIBRATION OF EXPERIMENTAL APPARATUS

B.1 Thermocouple Tests

The accuracy of the thermocouples used in the experiments was verified by comparison with a calibrated ISOTECH platinum resistance thermometer (PRT). The PRT model number is 935-14-72, with serial number 191069 and was calibrated by CSIR National Metrology Laboratory during the period of 25-27 May 2002 using the NML-TH\RT-0002 calibration procedure.

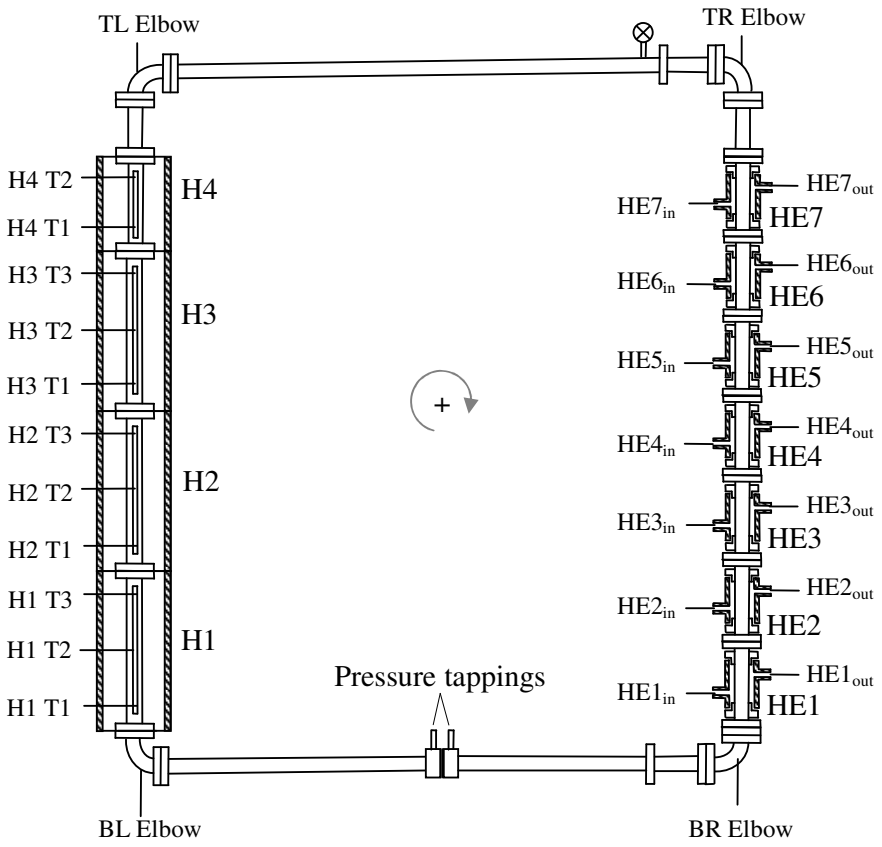

Figure B-1: Schematic layout of thermocouples used in experiment

Figure B-1 shows a schematic layout of the thermocouples used in the experiment. Four K-type thermocouples were used to measure the working fluid temperatures at the evaporator and condenser section inlets and outlets. These are labelled: BL (bottom left) elbow, BR (bottom right) elbow, TL (top left) elbow and TR (top right) elbow. Eleven K-type thermocouples were used to measure the cooling fluid in the pipe-within-pipe heat exchangers and are labelled HE (heat exchanger) 1 to 4 (where 1 is the bottom heat exchanger and 4 the top) and in, mid or out representing the inlet, midway and outlet temperatures. Eleven K-Type

thermocouples were used to measure the copper fin temperatures and are labelled H (heater) 1 to 4 (where 1 is the bottom heating section and 4 the top).

Table B-1 shows the variation of the thermocouples used to measure the working fluid temperature from the PRT. Table B-2 shows the comparison for the thermocouples used to measure the temperatures of the cooling fluid in the pipe-within-pipe heat exchangers. Table B-3 shows the comparison for thermocouples used to measure the temperatures of the copper fins.

For the fifteen K-type thermocouples (all water temperatures) measured on card 1 (Agilent 34903A General-Purpose 20-Channel Multiplexer Module serial number MY41105855) of the Agilent data acquisition/switch unit (34970A serial number MY44045582), the standard deviation at each of the measured points lies between 0.0687 and 0.255, with a maximum error of 3.19 %. For the eleven K-type thermocouples (copper fin temperatures) measured on card 2 (serial number MY41087111) of the data logger, the standard deviation at each of the measured points lies between 0.031 and 0.371, with a maximum error of 0.235 %.

As the calibration data contains over 2000 samples, the tables given below contain only a sample of the measured values. The sample chosen shows the temperatures of the thermocouples at a reference temperature of 20 – 80 °C with increments of 5 °C. The maximum standard deviations and error values are for the entire data set. All thermocouples were calibrated in specific channels (as laid out in APPENDIX C) and were kept in the calibrated channels for the duration of the experiments.

Table B-1: Working fluid temperature measurement

	Temperature in °C					% Error			
PRT	(1) BR Elbow	(2) BL Elbow	(3) TL Elbow	(4) TR Elbow	SD	(1) BR Elbow	(2) BL Elbow	(3) TL Elbow	(4) TR Elbow
20.002	20.254	20.262	20.215	20.164	0.1064	-1.25987	-1.29987	-1.06489	-0.80992
25.016	25.611	25.593	25.495	25.498	0.2443	-2.37848	-2.30652	-1.91477	-1.92677
30.003	30.4	30.409	30.279	30.286	0.1640	-1.3232	-1.3532	-0.91991	-0.94324
35.02	35.164	35.279	35.132	35.131	0.0926	-0.41119	-0.73958	-0.31982	-0.31696
40.01	39.924	40.246	40.08	40.074	0.1182	0.214946	-0.58985	-0.17496	-0.15996
45.012	45.052	45.094	44.932	45.016	0.0598	-0.08887	-0.18217	0.17773	-0.00889
50.031	49.927	50.004	49.81	49.891	0.0888	0.207871	0.053967	0.441726	0.279827
55.013	54.855	54.957	54.688	54.809	0.1274	0.287205	0.101794	0.590769	0.370821
60.025	59.84	59.921	59.625	59.758	0.1529	0.308205	0.173261	0.666389	0.444815
65.016	64.513	64.765	64.49	64.605	0.2177	0.773656	0.386059	0.809032	0.632152
70.065	69.839	70.032	69.81	69.885	0.1153	0.322558	0.047099	0.363948	0.256904
75.054	74.776	74.972	74.617	74.798	0.1723	0.3704	0.109255	0.582247	0.341088
80.052	79.718	79.89	79.504	79.73	0.2053	0.417229	0.202368	0.684555	0.402239
				Max	0.2966	0.906664	2.223626	2.553084	2.950095

Table B-2: Cooling fluid temperature measurement

	Temperature in °C								
PRT	(1) HE4 in	(2) HE4 out	(3) HE3 in	(4) HE3 mid	(5) HE3 out	(6) HE2 in	(7) HE2 mid	(8) HE2 out	(9) HE1 in
20.002	20.365	20.225	20.292	20.274	20.256	20.228	20.251	20.226	20.167
25.016	25.794	25.636	25.598	25.627	25.629	25.568	25.563	25.536	25.451
30.003	30.377	30.246	30.42	30.429	30.416	30.36	30.391	30.313	30.264
35.02	35.128	35.052	35.257	35.298	35.272	35.216	35.282	35.136	35.12
40.01	39.916	39.915	40.211	40.25	40.17	40.174	40.272	40.091	40.047
45.012	44.91	44.798	45.06	45.108	45.08	45.017	45.108	44.925	44.975
50.031	49.809	49.688	50.042	50.061	50.021	49.936	50.079	49.793	49.856
55.013	54.735	54.602	54.869	54.902	54.912	54.795	54.945	54.726	54.769
60.025	59.707	59.599	59.863	59.909	59.84	59.743	59.94	59.698	59.707
65.016	64.507	64.39	64.752	64.817	64.705	64.653	64.845	64.481	64.546
70.065	69.329	69.299	70.051	70.081	69.919	69.933	70.173	69.724	69.819
75.054	74.494	74.451	74.927	74.991	74.977	74.849	75.072	74.653	74.724
80.052	79.418	79.351	79.867	79.913	79.936	79.767	80.039	79.577	79.669

Table B-2: Cooling fluid temperature measurement continued

Temperature in °C			Error %										
(10) HE1 mid	(11) HE1 out	SD	(1) HE4 in	(2) HE4 out	(3) HE3 in	(4) HE3 mid	(5) HE3 out	(6) HE2 in	(7) HE2 mid	(8) HE2 out	(9) HE1 in	(10) HE1 mid	(11) HE1 out
20.2	20.2	0.09	-1.81	-1.11	-1.45	-1.36	-1.27	-1.13	-1.24	-1.11	-0.82	-0.88	-0.95
25.5	25.5	0.19	-3.11	-2.48	-2.33	-2.44	-2.45	-2.21	-2.18	-2.07	-1.73	-1.77	-1.97
30.3	30.3	0.12	-1.25	-0.81	-1.39	-1.42	-1.38	-1.19	-1.29	-1.03	-0.86	-0.83	-1.02
35.2	35.7	0.09	-0.30	-0.09	-0.68	-0.79	-0.72	-0.56	-0.74	-0.33	-0.28	-0.38	-0.42
40.1	40.1	0.12	0.23	0.24	-0.50	-0.60	-0.40	-0.41	-0.65	-0.20	-0.09	-0.17	-0.24
45.0	45.1	0.09	0.23	0.48	-0.11	-0.21	-0.15	-0.01	-0.21	0.19	0.08	0.01	-0.16
49.9	49.9	0.12	0.44	0.69	-0.02	-0.06	0.02	0.19	-0.09	0.47	0.34	0.22	0.08
54.8	54.9	0.11	0.51	0.75	0.26	0.20	0.18	0.40	0.12	0.52	0.44	0.40	0.25
59.7	59.8	0.12	0.53	0.71	0.27	0.19	0.31	0.47	0.14	0.54	0.52	0.52	0.31
64.7	64.7	0.18	0.78	0.96	0.41	0.31	0.48	0.56	0.26	0.84	0.72	0.49	0.41
70.1	70.1	0.29	1.05	1.09	0.02	-0.02	0.21	0.19	-0.15	0.48	0.35	-0.02	-0.03
74.9	75.0	0.21	0.75	0.80	0.17	0.08	0.10	0.27	-0.02	0.53	0.43	0.27	0.09
79.7	79.9	0.23	0.79	0.88	0.23	0.17	0.14	0.36	0.01	0.59	0.47	0.39	0.18
	Max	0.29	1.40	1.54	1.56	1.81	1.99	2.16	2.40	2.50	2.91	2.98	3.195

Table B-3: Copper fin temperature measurement

	Temperature in °C								
PRT	(1) H1 T1	(2) H1 T2	(3) H1 T3	(4) H2 T1	(5) H2 T2	(6) H2 T3	(7) H3 T1	(8) H3 T2	(9) H3 T4
24.277	24.332	24.403	24.353	24.353	24.354	24.346	24.348	24.367	24.34
25	25.471	25.374	25.398	25.449	25.447	25.443	25.445	25.41	25.431
30.016	31.097	30.804	30.883	30.947	30.96	30.806	30.79	30.735	30.782
35.02	36.041	35.71	35.789	35.825	35.884	35.736	35.75	35.697	35.662
40.016	41.027	40.577	40.744	40.699	40.799	40.601	40.636	40.495	40.535
45.031	46.198	45.667	45.856	45.72	45.877	45.683	45.706	45.502	45.579
50.014	51.152	50.539	50.811	50.764	50.87	50.571	50.617	50.433	50.53
55.016	56.199	55.612	55.836	55.797	55.877	55.604	55.611	55.421	55.518
60.014	61.19	60.6	60.843	60.778	60.863	60.628	60.669	60.471	60.519
65.019	66.142	65.354	65.802	65.703	65.78	65.475	65.552	65.232	65.429
70.036	71.085	70.238	70.71	70.628	70.695	70.376	70.447	70.251	70.402
75.054	74.494	74.451	74.927	74.991	74.977	74.849	75.072	74.653	74.724
80.052	79.418	79.351	79.867	79.913	79.936	79.767	80.039	79.577	79.669

Temperature in °C			Error %										
(10) H4 T1	(11) H4 T2	SD	(1) H1 T1	(2) H1 T2	(3) H1 T3	(4) H2 T1	(5) H2 T2	(6) H2 T3	(7) H3 T1	(8) H3 T2	(9) H3 T4	(10) H4 T1	(11) H4 T2
24.34	24.39	0.03	-0.226	-0.519	-0.31	-0.31	-0.31	-0.28	-0.29	-0.37	-0.25	-0.28	-0.46
25.48	25.477	0.13	-1.884	-1.496	-1.59	-1.79	-1.78	-1.77	-1.78	-1.64	-1.72	-1.94	-1.90
30.87	30.736	0.26	-3.601	-2.625	-2.88	-3.10	-3.14	-2.63	-2.57	-2.39	-2.55	-2.86	-2.39
35.84	35.684	0.24	-2.915	-1.970	-2.19	-2.29	-2.46	-2.04	-2.08	-1.93	-1.83	-2.34	-1.89
40.66	40.505	0.23	-2.526	-1.401	-1.81	-1.70	-1.95	-1.46	-1.54	-1.19	-1.29	-1.62	-1.22
45.69	45.497	0.27	-2.591	-1.412	-1.83	-1.53	-1.87	-1.44	-1.49	-1.04	-1.21	-1.48	-1.03
50.66	50.408	0.28	-2.275	-1.049	-1.59	-1.49	-1.71	-1.11	-1.20	-0.83	-1.03	-1.29	-0.78
55.61	55.393	0.29	-2.150	-1.083	-1.49	-1.41	-1.56	-1.06	-1.08	-0.73	-0.91	-1.09	-0.68
60.64	60.431	0.28	-1.959	-0.976	-1.38	-1.27	-1.41	-1.02	-1.09	-0.76	-0.84	-1.05	-0.69
65.53	65.132	0.31	-1.727	-0.515	-1.20	-1.05	-1.17	-0.70	-0.81	-0.32	-0.63	-0.78	-0.17
70.46	70.155	0.28	-1.497	-0.288	-0.96	-0.84	-0.94	-0.48	-0.58	-0.36	-0.52	-0.61	-0.16
74.85	74.984	0.21	0.746	0.803	0.16	0.08	0.10	0.27	-0.02	0.53	0.43	0.27	0.09
79.73	79.905	0.22	0.791	0.875	0.23	0.17	0.14	0.35	0.01	0.59	0.47	0.39	0.18
	Max	0.29	1.404	1.543	1.56	1.80	1.99	2.15	2.40	2.50	2.91	2.98	3.195

B.2 Orifice Plate Calibration

The orifice plate was calibrated in place in the experimental assembly. The flow rate of the water through the pipe was measured by means of a 5 litre bucket, a stop watch and a 30kg NAGATA counting scale (EVA asset number 327889) capable of measuring in 0.02 kg increments. A total of six sets of calibration data were obtained using the Endress and Hauser DeltabarS differential pressure

transducer (serial number A8069B0109D) capable of measuring 0-500 mbar pressure differences in both the forward and reverse directions.

A curve was fitted through the data using the computer software DataFit Nonlinear Regression version 8.2.79 (Copyright (c) 1995-2006 Oakdale engineering) with 99% confidence intervals. The software applies regression methods through observation and presents a selection of the most appropriate of the 250 models in its database.

After 415 observations and 15 nonlinear iterations, an eighth order polynomial was fitted to the experimentally obtained data for forward flow.

$$y = ax^8 + bx^7 + cx^6 + dx^5 + ex^4 + fx^3 + gx^2 + hx + i \quad \text{(B-1)}$$

Where:

y = $\dot{m}$ (in kg/s)
x = ΔP (in Pa)
a = -8.44825834440864E-28
b = 1.37000491965785E-23
c = -9.24069227056674E-20
d = 3.36894961741779E-16
e = -7.24603718700376E-13
f = 9.46127389069242E-10
g = -7.49938923231085E-07
h = 0.000391136808117516
i = -0.000532314400249022

Figure B-2 shows the resulting calibration curve. The proportion of variance explained by this curve is 99.578% and the standard error of the estimate is 0.0034.

For reverse flow, after 40 observations and 12 nonlinear iterations, a curve was fitted to the experimentally obtained data in the form of:

$$y = \frac{ax}{b+x} \quad \text{(B-2)}$$

Where:

y = $\dot{m}$ (in kg/s)
x = ΔP (in Pa)
a = -0.166543176269312
b = -670.272687959592

Figure B-3 shows the resulting calibration curve. The proportion of variance explained by this curve is 96.859% and the standard error of the estimate is 0.00777

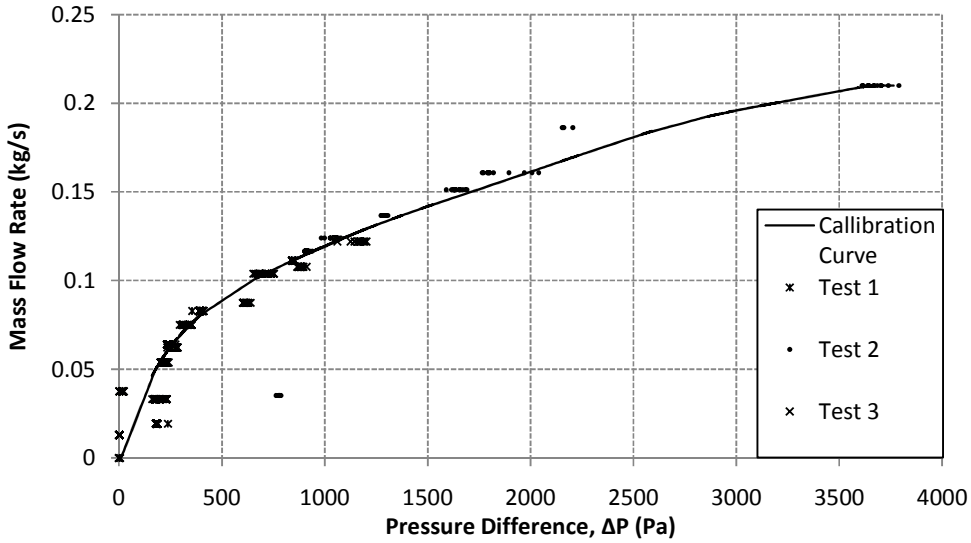

Figure B-2: Polynomial curve fit to forward flow data

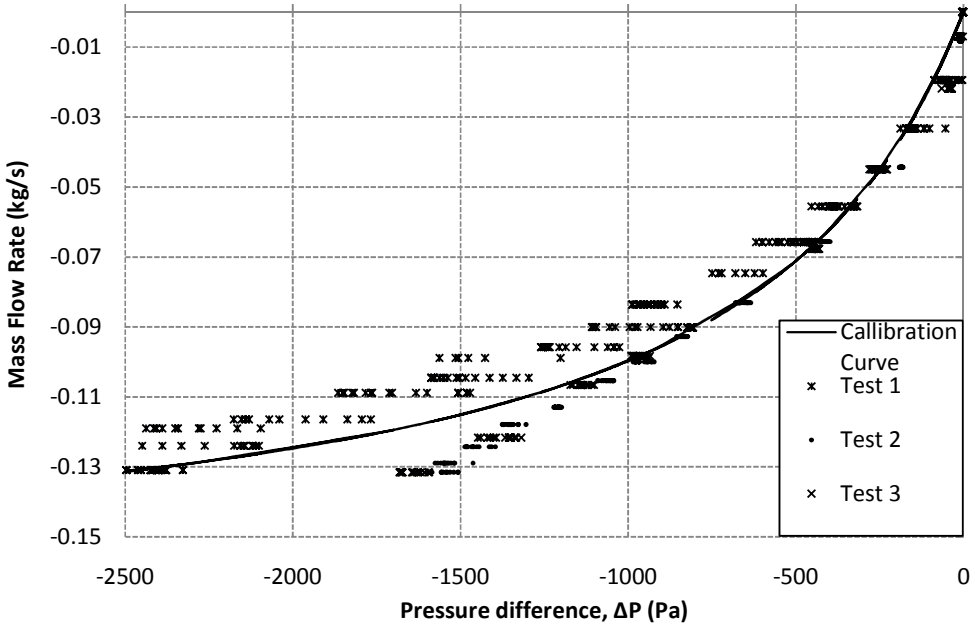

Figure B-3: Polynomial curve fit to reverse flow data

B.3 Heat Exchanger Calibration

The validity of using the Gnielinski correlation to calculate the forced convection heat transfer coefficient was tested by calibrating one of the pipe-in-pipe heat exchangers. In order to calibrate the heat exchanger, one 2 m section of the

condenser section was connected to a geyser capable of incrementally heating water from room temperature to a maximum of 100 °C. The heated water was pumped through the inside copper pipe, with the inlet at the top of the condenser section, and the outlet at the bottom. The mass flow rate of the hot water was measured using a bypass valve, visual water level measurement and a stopwatch. The cooling water was tap fed from the bottom of the outer glass pipe and flow rate was measured using a 5 L bucket, stopwatch and 30kg NAGATA counting scale (EVA asset number 327889) capable of measuring in 0.02 kg increments.

The heat exchanger was calibrated at six different hot water temperatures, 30 – 70 °C with 10 °C increments. For each temperature, three hot water mass flow rates were used (low, medium and high) and for each hot water flow rate, the cooling water mass flow rate was also varied (low, medium and high). Eight K-type thermocouples were used to measure the inlet and outlet temperatures of the hot and cold water. The data was logged on an Agilent data logger once every ten seconds resulting in 3240 data points.

The heat transferred from the hot water to the cold water can be calculated using (Mills, 1999): $\dot{Q} = \dot{m} c_p \Delta T$ (B-3)

The resulting energy balance is shown in Table B-4. The average difference between $\dot{Q}_{cw}$ and $\dot{Q}_H$is 7.73 %. The discrepancy can be explained by the heat lost to the environment.

The forced convective heat transfer coefficients were calculated from experimental data using (Mills, 1999):

$$h_{c,o} = \frac{\dot{Q}_{cw}}{A_{zod} \Delta T} \quad \text{(B-4)}$$

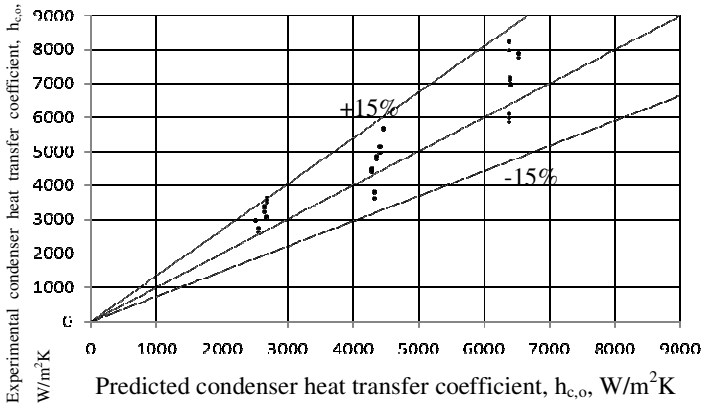

Figure B-4: Predicted condenser heat transfer coefficient as a function of experimentally determined heat transfer coefficient

The Gnielinski correlation was evaluated at experimental temperatures and mass flow rates:

$$Nu_{cw} = \frac{(f/8)\cdot(Re_{cw}-1000)\cdot Pr_{cw}}{1+12.7\cdot(f/8)^{0.5}\cdot({Pr_{cw}}^{2/3}-1)} \qquad 3000 \leq Re_{cw} \leq 10^6 \qquad (9\text{-}1)$$

Theoretical heat transfer coefficients were generated using equation 2-40:

$$h_{c,o} = \frac{Nu_{cw}k_{cw}}{D_{eq}} \qquad (9\text{-}2)$$

Figure B-4 shows the comparison between experimental and theoretical heat transfer coefficients. Figure B-4 shows clearly that the predicted condenser heat transfer coefficients do not deviate more than 15 % from experimentally determined values. This validates the use of the Gnielinski correlation for forced convection heat transfer coefficients in the condenser section, $h_{c,o}$.

Table B-4: Heat exchanger energy balance

Temperature	$\dot{m}_{cw}$	$\dot{m}_H$	$\dot{Q}_{cw}$	$\dot{Q}_H$	**Error %**
30 °C	High – 0.211 kg/s	Low – 1.444 kg/s	3995.791	4546.97	12.12
		Medium – 1.827 kg/s	4248.547	4948.552	14.15
		High – 2.006 kg/s	4214.503	4719.822	10.71
	Medium - 0.147 kg/s	Low – 1.444 kg/s	3246.365	3136.864	-3.49
		Medium – 1.989 kg/s	3501.146	3496.185	-0.14
		High – 2.025 kg/s	3514.34	3493.481	-0.60
	Low – 0.0827 kg/s	Low – 1.056 kg/s	2665.909	1877.791	-41.97
		Medium – 1.866 kg/s	2759.554	1969.301	-40.13
		High – 2.045 kg/s	2779.973	1976.604	-40.64
40 °C	High – 0.211 kg/s	Low – 0.708 kg/s	5361.186	5666.333	5.39
		Medium – 1.766 kg/s	5647.064	6096.84	7.38
		High – 2.045 kg/s	5817.754	6140.064	5.25
	Medium – 0.141 kg/s	Low – 1.155 kg/s	4383.538	4606.568	4.84
		Medium – 1.987 kg/s	4662.321	4830.586	3.48
		High – 2.045 kg/s	4736.344	4763.248	0.56
	Low – 0.088 kg/s	Low – 1.155 kg/s	3311.709	3665.151	9.64
		Medium – 1.885 kg/s	3466.016	3888.29	10.86
		High – 2.035 kg/s	3515.325	3770.59	6.77
50 °C	High – 0.215 kg/s	Low – 1.634 kg/s	8109.065	8359.876	3.00
		Medium – 1.927 kg/s	8617.376	9148.981	5.81
		High – 2.070 kg/s	8873.083	9334.514	4.94
	Medium – 0.144 kg/s	Low – 1.381 kg/s	6036.152	6998.655	13.75
		Medium – 1.957 kg/s	6533.904	7645.833	14.54
		High – 2.070 kg/s	6533.904	7645.833	14.54
	Low – 0.087 kg/s	Low – 0.560 kg/s	6663.952	7914.672	15.80
		Medium – 1.804 kg/s	4335.227	5843.878	25.82
		High – 2.047 kg/s	4635.082	6332.283	26.80
60 °C	High – 0.210 kg/s	Low – 1.337 kg/s	10401.04	13447.57	22.65
		Medium – 1.870 kg/s	11505.7	12214.1	5.80
		High – 2.045 kg/s	11782.11	12374.99	4.79
	Medium – 0.146 kg/s	Low – 1.405 kg/s	8266.72	11013.84	24.94
		Medium – 1.944 kg/s	9173.598	9986.277	8.14
		High – 2.043 kg/s	9242.124	10405.67	11.18
	Low – 0.088 kg/s	Low – 1.405 kg/s	6006.104	9219.395	34.85
		Medium – 1.883 kg/s	6539.43	9014.189	27.45
		High – 2.018 kg/s	6726.62	8487.742	20.75
70 °C	High – 0.210 kg/s	Low – 1.545 kg/s	13837.37	13715.8	-0.89
		Medium – 1.924 kg/s	14750.11	14997.1	1.65
		High – 2.007 kg/s	15253.18	15305.97	0.34
	Medium – 0.143 kg/s	Low – 1.026 kg/s	10070.31	10775.72	6.55
		Medium – 1.930 kg/s	11613.76	12180.27	4.65
		High – 2.007 kg/s	11745.18	12959.98	9.37
	Low – 0.084 kg/s	Low – 1.208 kg/s	7073.872	9306.611	23.99
		Medium – 1.838 kg/s	7984.741	10760.47	25.80
		High – 1.982 kg/s	8294.264	11336.94	26.84

APPENDIX C: ERROR ANALYSIS

C.1 Single to Two-Phase Flow

Three single to two-phase operating mode experiments were performed on consecutive days (7, 8 and 9 July 2010). The initial conditions were assessed for consistency by calculating the sample mean using the following equation (Vining, 1998):

$$\bar{x} = \sum_{i=1}^{n} \frac{x_i}{n} \quad \text{(C-3)}$$

The sample standard deviation is calculated as follows (Beckwoth, Maragoni, & Lienhard, 1993):

$$S_x = \sqrt{\frac{n\sum_{i=1}^{n} y_i^2 - \left(\sum_{i=1}^{n} y_i\right)^2}{n(n-1)}} \quad \text{(C-4)}$$

In order to measure the deviation of the initial conditions, the percentage of variation was calculated by dividing the standard deviation by the statistical average. This value gives an indication of how well the average values represent the actual experimental data. The results are shown in Table C-1.

Table C-1: Experimental conditions and standard deviation for single to two-phase flow

		Test 1	**Test 2**	**Test 3**	$\bar{x}$	S_x	**Error %**
	$\dot{m}_{cw}$	0.191 kg/s	0.184 kg/s	0.192 kg/s	0.189 kg/s	0.004 kg/s	2.15
	T_e	12.932 °C	12.658 °C	14.792 °C	13.461 °C	1.161 °C	8.63
Power Variation Time, s	50 %	3670 s	3710 s	4150 s	3843.33 s	266.33 s	6.93
	70 %	7330 s	7400 s	7810 s	7513.33 s	259.29 s	3.45
	100 %	11170 s	12980 s	13300 s	12483.33 s	1148.58 s	9.20
	0 %	13020 s	16720 s	17050 s	15596.67 s	2237.55 s	14.35
Power Variation, W	30 %	1180.2 W	1230.78 W	1202.6 W	1204.53 W	25.34 W	2.10
	50 %	3749.38 W	3746.92 W	3747.98 W	3748.09 W	1.23 W	0.03
	70 %	6842.68 W	6692.18 W	6691.48 W	6742.11 W	87.09 W	1.29
	100 %	9710.4 W	9262.4 W	9439.15 W	9470.65 W	225.66 W	2.38

The table shows a 2.15% variation between the actual cooling water mass flow rate and the statistical average value. The environmental temperature varies by 8.6%, which is due to the relatively high temperature in Test 3. The time that the system was maintained at each power setting has a maximum variation of 14.3%, which occurs at switch off. This is due to the first test being switched off at a much earlier time than the other two tests. The wattage measured at each power setting varies very little, with a maximum variation of 2.4%. These values, with the exception of the time to shut down, all fall below 10%. This shows that the tests have nearly identical experimental circumstances and environmental conditions.

The single to two-phase operating mode experiments have a sample number n = 3, deeming the t-distribution (appropriate for sample numbers less than 30) applicable for error analysis (Beckwoth, Maragoni, & Lienhard, 1993). Initially, the sample mean and standard deviation are calculated using equations C-1 and C-

2 respectively. The sample mean and standard deviation are used as approximations of the true values for an infinite sample population. The true mean, μ, lies in the interval (Beckwoth, Maragoni, & Lienhard, 1993):

$$\bar{x} - t_{\alpha/2,v}\frac{S_x}{\sqrt{n}} < \mu < \bar{x} + t_{\alpha/2,v}\frac{S_x}{\sqrt{n}} \quad \text{(C-5)}$$

In equation C-3, $\propto = 1 - c$, $v = n - 1$ and c represents the confidence interval. Beckwith et al (1993) provides tables for $t_{\alpha/2,v}$. For the 95% confidence interval:

c = 0.95

α = 0.05

v = 2

$t_{\alpha/2,v} = t_{0.025,2} = 4.303$

The procedure laid out was performed using Microsoft Excel (2007) for each measurement of each data set. Due to the number of data points for each temperature and mass flow rate measured, the 95% confidence interval limits were averaged over the single phase and single to two-phase sections. Graph C-1 shows the results of the sample mean, upper and lower confidence limits for the condenser outlet temperature, to serve as an example. The upper limit corresponds to $\bar{x} + t_{\alpha/2,v}\frac{S_x}{\sqrt{n}}$ and the lower limit to $\bar{x} - t_{\alpha/2,v}\frac{S_x}{\sqrt{n}}$.

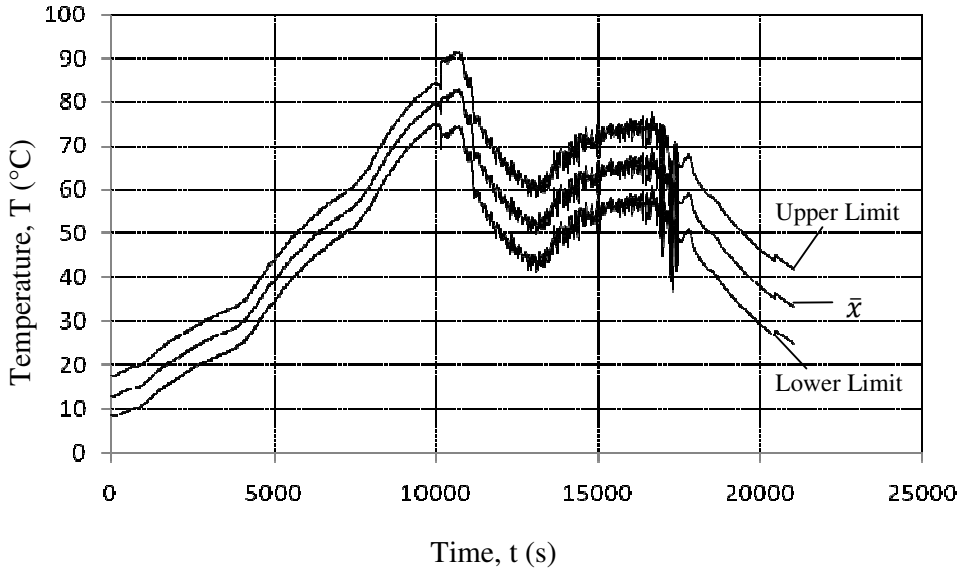

Figure C-1: Sample mean, upper and lower confidence limits for condenser outlet temperature

The graph shows the range, from lower limit to upper limit, within which 95% of the data of an infinite sample population would fall with 95% confidence. The average error (as calculated by dividing the standard deviation by the sample mean) is 4.5% and shows that the data is reasonably well repeated. Table C-2 shows the deviation from mean for a 95 % confidence interval for the

temperatures measured during the single to two-phase operating mode experiments and the error percentage, to indicate how accurately the mean values represent the actual data. As seen in the table, the error ranges from 1.2 % to 4.7 %, which shows that the data is well repeated and that the statistical mean can be used to accurately represent the actual experimental data.

Table C-2: Measured temperatures and standard deviation for single to two-phase flow

		$t_{\alpha/2,v}\frac{S_x}{\sqrt{n}}$		**Error percentage**
		Single Phase	**Boiling**	$S_x/\bar{x}$
Working Fluid Temperatures	Evaporator inlet	4.598637 °C	7.224639 °C	4.679946 %
	Evaporator outlet	6.59963 °C	6.0133 °C	3.331134 %
	Condenser inlet	6.422827 °C	6.873146 °C	3.739216 %
	Condenser outlet	4.676996 °C	8.504696 °C	4.630534 %
Cooling Fluid Temperatures	HE 7 inlet	0.62632 °C	0.431583 °C	1.190696 %
	HE 7 outlet	0.851781 °C	2.592992 °C	3.120619 %
Fin Temperatures	H1 T1	7.768489 °C	6.472652 °C	3.29684 %
	H1 T2	7.565606 °C	6.213418 °C	3.319808 %
	H1 T3	7.283593 °C	6.309471 °C	3.363667 %
	H2 T1	7.026671 °C	6.592543 °C	3.386799 %
	H2 T2	7.098429 °C	8.030568 °C	3.61542 %
	H2 T3	6.60621 °C	8.477123 °C	3.463538 %
	H3 T1	6.324332 °C	7.83174 °C	3.43222 %
	H3 T2	6.218653 °C	7.550142 °C	3.470443 %
	H3 T3	5.890428 °C	7.901015 °C	3.426548 %
	H4 T1	5.44204 °C	7.443728 °C	3.482129 %
	H4 T2	5.500834 °C	8.01067 °C	3.736374 %

C.2 Single Phase Flow

Three single phase operating mode experiments were performed on consecutive weekdays (18, 21 and 22 June 2010). The initial conditions were assessed for consistency by calculating the sample mean and sample standard deviation using equations C-1 and C-2 respectively.

In order to measure the deviation of the initial conditions, the percentage of variation was calculated by dividing the standard deviation by the statistical average. This value gives an indication of how well the average values represent the actual experimental data. The results are shown in Table C-3.

The cooling water mass flow rate is decreased for each consecutive test, which results in a large discrepancy between statistical mean an actual values. The environmental temperature varies by 12.17 %, which is due to the relatively low temperature in Test 1. The time that the system was maintained at each power setting has a maximum variation of 14.61%, which occurs when the system is switched from 30% to 50% of full power input. This is due to the first test being switched over to 50% power at a much later (1000 s) stage than the other two tests. The wattage measured at each power setting varies very little, with a maximum variation of 9.54%, decreasing steadily until full power. The table shows clearly that the only relevant changing variable is the cooling water mass

flow rate for each pipe-within-pipe heat exchanger. The other conditions are relatively well repeated.

Table C-3: Experimental conditions and standard deviation for single phase flow

		Test 1	**Test 2**	**Test 3**	$\bar{x}$	S_x	**Error %**
	$\dot{m}_{cw,1}$	0.085 kg/s	0.057 kg/s	0.006 kg/s	0.071 kg/s	0.020 kg/s	27.47
	$\dot{m}_{cw,2}$	0.106 kg/s	0.0358 kg/s	0.009 kg/s	0.071 kg/s	0.050 kg/s	70.01
	$\dot{m}_{cw,3}$	0.093 kg/s	0.052 kg/s	0.021 kg/s	0.073 kg/s	0.029 kg/s	39.74
	$\dot{m}_{cw,4}$	0.113 kg/s	0.057 kg/s	0.020 kg/s	0.085 kg/s	0.0399 kg/s	46.21
	$\dot{m}_{cw,5}$	0.116 kg/s	0.048 kg/s	0.014 kg/s	0.082 kg/s	0.048 kg/s	58.47
	$\dot{m}_{cw,6}$	0.089 kg/s	0.047 kg/s	0.014 kg/s	0.068 kg/s	0.030 kg/s	43.36
	$\dot{m}_{cw,7}$	0.090kg/s	0.087 kg/s	0.025 kg/s	0.088 kg/s	0.002 kg/s	2.53
	T_e	11.051 °C	14.003 °C	13.401 °C	12.818 °C	1.560 °C	12.17
Power Variation Time	50 %	4710 s	3700 s	3680 s	4030 s	588.98 s	14.61
	70 %	8380 s	7950 s	7380 s	7903.33 s	501.63 s	6.35
	100 %	12050 s	12210 s	11060 s	11773.33 s	622.92 s	5.29
	0 %	15720 s	15890 s	14560 s	15390 s	723.81 s	4.70
Power Variation Wattage	30 %	1219.93 W	1416.98 W	1194.38 W	1277.09 W	121.81 W	9.54
	50 %	3976.18 W	3805.03 W	3778.25 W	3853.15 W	107.38W	2.79
	70 %	6994.93 W	6692.18 W	6842.33 W	6843.14 W	151.38 W	2.21
	100 %	9483.78 W	9483.78 W	9483.78 W	9483.78 W	0 W	0

The single phase operating mode experiments have a sample number n = 3, deeming the t-distribution (appropriate for sample numbers less than 30) applicable for error analysis (Beckwoth, Maragoni, & Lienhard, 1993).

Following the procedure laid out in the previous section, Table C-4 was generated. The table shows the deviation from mean for a 95 % confidence interval for the temperatures measured during the single phase operating mode experiments and the error percentage, to indicate how accurately the mean values represent the actual data. The table shows that the statistical sample mean cannot accurately be used to represent the actual experimental data. Due to the large variation in cooling water mass flow rates, the heat exchanger outlet temperatures vary as much as 22.9 %. The other error percentages are relatively small, with most fin temperatures yielding an error below 10% and the heat exchanger inlet temperatures yielding an error below 5%. When taking the varying cooling water mass flow rate into consideration, the experimental conditions can be considered well repeated.

Table C-4: Measured temperatures and standard deviation for single phase flow

		$t_{\alpha/2,v}\frac{S_x}{\sqrt{n}}$	**Error percentage**
		Single Phase	$S_x/\bar{x}$
Working Fluid Temperatures	Evaporator inlet	10.28394 °C	12.66955 %
	Evaporator outlet	16.69277 °C	10.20515 %
	Condenser inlet	15.40341 °C	9.693324 %
	Condenser outlet	11.03194 °C	12.84809 %
Cooling Fluid Temperatures	HE1,2 inlet	1.487937 °C	3.420654 %
	HE1 outlet	13.25794 °C	22.86931 %
	HE2 outlet	6.062392 °C	11.80103 %
	HE3,4 inlet	1.710294 °C	3.914464 %
	HE3 outlet	7.20861 °C	13.52362 %
	HE4 outlet	7.822343 °C	14.06516 %
	HE5,5 inlet	1.786817 °C	4.081032 %
	HE5 outlet	8.6328 °C	14.43209 %
	HE6 outlet	15.08282 °C	22.06005 %
	HE 7 inlet	1.876642 °C	4.270821 %
	HE 7 outlet	7.18743 °C	12.25127 %
Fin Temperatures	H1 T1	25.15453 °C	11.51668 %
	H1 T2	41.15796 °C	20.73592 %
	H1 T3	18.82052 °C	9.846558 %
	H2 T1	17.62327 °C	9.745135 %
	H2 T2	17.6472 °C	9.87601 %
	H2 T3	16.32862 °C	9.389501 %
	H3 T1	15.34371 °C	9.413344 %
	H3 T2	14.98727 °C	9.478256 %
	H3 T3	14.62676 °C	9.365291 %
	H4 T1	13.00885 °C	9.207782 %
	H4 T2	13.69058 °C	9.733579 %

C.3 Cooling Water Mass Flow Rate

Twelve experiments were performed on separate weekdays, each lasting a minimum 5 hours. The cooling water mass flow rate in each condenser section was measured using a 5 litre bucket, a stopwatch and a 30kg NAGATA counting scale (EVA asset number 327889) capable of measuring in 0.02 kg increments. Measurements were made prior to experimental start-up, at each power increase interval and at shut down, yielding a total of 6 measurements per experiment.

The mass flow rates for each condenser section, within each experimental data set, were assessed for consistency by calculating the sample mean and sample standard deviation using equations C-1 and C-2 respectively.

The single phase operating mode experiments have a sample number n = 6, deeming the t-distribution (appropriate for sample numbers less than 30) applicable for error analysis (Beckwoth, Maragoni, & Lienhard, 1993).

Following the procedure laid out in the previous section, Table C-5 was generated. In equation C-3:
c = 0.95
α = 0.05
v = 6
$t_{\alpha/2,v} = t_{0.025,6} = 4.303$

The table shows the sample mean, deviation from mean for a 95 % confidence interval for the cooling water mass flow rates and the error percentage, to indicate how accurately the mean values represent the actual data. The highest error percentage is 7.006 %, which occurs on the first test date at HE_7. The other error percentages fall far below 10 %, with an average error percentage of 1.55 % and the cooling water mass flow rate measurements are considered well repeated.

Table C-5: Experimental conditions and standard deviation for mass flow rate

		$\bar{x}$	S_x	**Error %**
18 June	$\dot{m}_{cw,1}$	0.084829 kg/s	0.001224 kg/s	1.44333
	$\dot{m}_{cw,2}$	0.106 kg/s	0.002411 kg/s	2.274899
	$\dot{m}_{cw,3}$	0.093 kg/s	0.002104 kg/s	2.262327
	$\dot{m}_{cw,4}$	0.112467 kg/s	0.003073 kg/s	2.732527
	$\dot{m}_{cw,5}$	0.11559 kg/s	0.004969 kg/s	4.298672
	$\dot{m}_{cw,6}$	0.089219 kg/s	0.004526 kg/s	5.073194
	$\dot{m}_{cw,7}$	0.089752 kg/s	0.00667 kg/s	7.006001
21 June	$\dot{m}_{cw,1}$	0.057233 kg/s	0.000896 kg/s	1.564942
	$\dot{m}_{cw,2}$	0.0358 kg/s	0.000189 kg/s	0.526709
	$\dot{m}_{cw,3}$	0.0522 kg/s	0.000943 kg/s	1.806148
	$\dot{m}_{cw,4}$	0.057067 kg/s	0.000566 kg/s	0.991271
	$\dot{m}_{cw,5}$	0.047967 kg/s	0.000236 kg/s	0.491388
	$\dot{m}_{cw,6}$	0.04735 kg/s	2.36E-05 kg/s	0.049779
	$\dot{m}_{cw,7}$	0.0866 kg/s	9.43E-05 kg/s	0.108869
22 June	$\dot{m}_{cw,1}$	0.006133 kg/s	9.43E-05 kg/s	1.537189
	$\dot{m}_{cw,2}$	0.009467 kg/s	0 kg/s	0
	$\dot{m}_{cw,3}$	0.020667 kg/s	0 kg/s	0
	$\dot{m}_{cw,4}$	0.019633 kg/s	4.71E-05 kg/s	0.240104
	$\dot{m}_{cw,5}$	0.013833 kg/s	4.71E-05 kg/s	0.340774
	$\dot{m}_{cw,6}$	0.013867 kg/s	0 kg/s	0
	$\dot{m}_{cw,7}$	0.025367 kg/s	4.71E-05 kg/s	0.185836
23 June	$\dot{m}_{cw,1}$	0.001883 kg/s	2.36E-05 kg/s	1.251516
	$\dot{m}_{cw,2}$	0.001217 kg/s	2.36E-05 kg/s	1.937279
	$\dot{m}_{cw,3}$	0.000767 kg/s	0 kg/s	0
	$\dot{m}_{cw,4}$	0.002583 kg/s	2.36E-05 kg/s	0.912396
	$\dot{m}_{cw,5}$	0.000858 kg/s	1.18E-05 kg/s	1.373023
	$\dot{m}_{cw,6}$	0.011017 kg/s	2.36E-05 kg/s	0.213951
	$\dot{m}_{cw,7}$	0.015717 kg/s	2.36E-05 kg/s	0.14997
29 June	$\dot{m}_{cw,6}$	0.3233 kg/s	0.004477 kg/s	1.384798
	$\dot{m}_{cw,7}$	0.2714 kg/s	0.003878 kg/s	1.42894
30 June	$\dot{m}_{cw,6}$	0.082544 kg/s	0.001246 kg/s	1.509599
	$\dot{m}_{cw,7}$	0.1142 kg/s	0.003063 kg/s	2.6823
1 July	$\dot{m}_{cw,6}$	0.016813 kg/s	0.000578 kg/s	3.438459
	$\dot{m}_{cw,7}$	0.091027 kg/s	0.00037 kg/s	0.406458
5 July	$\dot{m}_{cw,7}$	0.1934 kg/s	0.006197 kg/s	3.204123
7 July	$\dot{m}_{cw,7}$	0.190267 kg/s	0.004092 kg/s	2.150807
8 July	$\dot{m}_{cw,7}$	0.184883 kg/s	0.002166 kg/s	1.171314
9 July	$\dot{m}_{cw,7}$	0.189233 kg/s	0.004919 kg/s	2.599549

C.4 Correlation Sensitivity Analysis

A sensitivity analysis was performed on the generated inside-pipe heat transfer coefficient correlations for both the evaporator and condenser sections. The aim is to assess the effect of variation of each parameter in the correlation on the Nusselt number value. This will show how sensitive the correlations are to errors in parameters.

For the evaporator section, the generated takes the form:

$$Nu_b = \mathrm{a}Re_q^b Pr^c Gr^d \quad (6\text{-}8)$$

The experimental data used to generate the correlation (Re_q, Pr and Gr) were varied incrementally by 10, 25, 50 and 100% to assess the affect of experimental error on the correlation results. The calculated parameters (a, b, c and d) were also varied incrementally to assess the effect of human error on the correlation results. The resulting average error percentages are shown in table C-6.

Table C-6: Evaporator inside-pipe heat transfer coefficient correlation sensitivity analysis

Variation	+10%	+25%	+50%	+100%	-10%	-25%	-50%	-100%
	Average error %							
Re_q	20.44	54.55	120.56	221.04	18.58	42.95	74.14	100
Pr	3.30	7.89	14.80	22.57	3.52	9.33	21.02	100
Gr	7.65	16.99	28.71	39.29	9.19	27.14	78.35	100
A	10	25	50	100	10	25	50	100
b	105.80	546.50	4820.74	153004	49.45	80.24	94.80	99.32
c	6.79	17.86	38.94	80.85	6.36	15.14	27.97	48.08
D	90.45	99.71	99.99	100	960.38	37321	$1.5x10^7$	$2.8x10^{12}$

Table C-6 shows that the fluid parameter in the evaporator heat transfer coefficient correlation that most affects the Nusselt number value is the Reynolds number. The correlation will allow very small errors in Reynolds number but at 25% variation the error becomes unacceptable. The most sensitive calculated parameter, as can be seen in table C-6, is the Reynolds number coefficient (b). This is expected as the Reynolds number has the greatest effect, in this correlation, on the result. The table shows that the correlation is quite sensitive to experimental and human error.

For the condenser section, the generated correlation takes the form:

$$Nu_b = aRe_q^b Pr^c \quad (6\text{-}7)$$

The experimental data used to generate the correlation (Re_q and Pr) were varied incrementally by 10, 25, 50 and 100% to assess the affect of experimental error on the correlation results. The calculated parameters (a, b and c) were also varied incrementally to assess the effect of human error on the correlation results. The resulting average error percentages are shown in table C-7.

Table C-7: Condenser inside-pipe heat transfer coefficient correlation sensitivity analysis

Variation	+10%	+25%	+50%	+100%	-10%	-25%	-50%	-100%
	Average error %							
Re_q	5.26	12.75	24.36	37.90	5.51	14.33	31.11	100
Pr	10.99	27.66	55.85	92.37	10.89	27.01	53.17	100
A	10	25	50	100	10	25	50	100
B	15.13	43.69	113.58	330.57	12.68	28.06	46.67	68.99
C	23.99	71.26	193.84	599.72	19.32	41.51	65.72	88.17

Table C-7 shows that the fluid parameter in the condenser heat transfer coefficient correlation that most affects the Nusselt number value is the Prandtl number. The

correlation will allow very high errors in Reynolds number before the error percentage becomes unacceptable. The most sensitive calculated parameter, as can be seen in table C-6, is the Prandtl number coefficient (c). This is expected as the Prandtl number has the greatest effect, in this correlation, on the result. The table shows that the correlation is quite robust and allows a relatively high degree of experimental and human error.

The evaporator correlation is much more sensitive than the condenser correlation. This is due to the inaccuracy of using the electrical input power to determine the Reynolds number (as explained in detail in Section 6.4).

C.5 Time Step Size Independence of Integration Scheme

A finite-difference integration scheme can be proven to be time step independent if it is convergent at the given time-step size. Convergence implies all solutions in response to initial conditions and excitations converge point-wise to the corresponding solutions of the original differential equation as the step sizes approach zero (Farlow, 1993).

Convergence is established through use of the Lax-Richtmyer equivalence theorem. This theorem states that "a consistent finite-difference scheme for a partial differential equation for which the initial-value problem is well posed is convergent if and only if it is stable."

A finite difference scheme is said to be consistent with the original partial differential equation if, in the limit as the sampling intervals approach zero, the original partial differential equation is obtained from the finite difference scheme, i.e. the local truncation error tends to zero. The forward finite difference approximation is, by definition, consistent. The truncation error, ξ, is proportional to the square of the spatial step size, h, and the time step size, k, (Smith, 1965), i.e.:

$$\xi \triangleq O(k) + O(h^2) \quad \text{(C-6)}$$

$$\lim_{k\to 0, h\to 0} \xi = 0 \quad \text{(C-7)}$$

The stability criterion for this integration method states that (Smith, 1965):

$$0 \leq \frac{k}{h^2} \leq 0.5 \quad \text{(C-8)}$$

In the one dimensional discretised theoretical model, the thermosyphon is divided into 40 discreet control volumes. The control volumes vary in length, to ensure each separate section is wholly encompassed within the control volume boundaries. The control numbers are numbered clock-wise, starting from bottom right. Table C-8 shows the control volume numbers, lengths and associated stability criteria. With a time step of 0.01 s (as used in the computer simulation), the method is at all times stable and consistent. The finite difference scheme is thus convergent with the original partial differential equation (and thus time step independent).

Table C-8: Number of control volume, lengths and stability criteria

		Number	Length (in m)	$\frac{k}{h^2}$
N1		10	0.800	0.016
N2		10		
N2a	Pre evaporator	1	0.225	0.198
N2b	HE1 – HE3	6	0.950	0.011
N2b	HE4	2	0.275	0.132
N2c	Post evaporator	1	0.225	0.198
N3		10	0.800	0.016
N4		10		
N4a	Pre condenser	1	0.475	0.016
N4b	Condenser	1	0.500	0.044
N4c	Post condenser	8	0.753	0.018

C.6 Sample Calculations

In order to verify the theoretical heat transfer coefficient calculations described in section 5.2. this section presents sample calculations performed for one iteration of one case. The specific case presented is single to two-phase operating mode. He "step" numbers refer to steps of the computer program calculation procedure as detailed in section 3.4.

Step 1: Define constants and material properties taken as constants:

$\dot{m}_{cw} = 0.1915\ kg/s$ cooling water mass flow rate

$c_{p,cw} = 4174\ J/kg\ K$ specific heat, constant pressure

$c_{v,cw} = 4174\ J/kg\ K$ specific heat, constant volume

$ID_{cw} = 0.035\ m$ heat exchanger inside pipe outer diameter

$OD_{cw} = 0.54\ m$ heat exchanger outside pipe inner diameter

$A_{x,cw} = \frac{\pi({OD_{cw}}^2 - {ID_{cw}}^2)}{4} = 0.001328$ cross-sectional area of heat exchanger

$D_{eq,cw} = OD_{cw} - ID_{cw} = 0.019\ m$ equivalent diameter of heat exchanger

$t_{wall} = 0.0015\ m$ heat exchanger wall thickness

$k_{wall} = 386\ W/m\ K$ thermal conductivity of copper

$L_{tank} = B_{tank} = 0.3\ m$ length and breadth of expansion tank

$Z_{tank} = 0.05\ m$ height of water in expansion tank

$P_{tank} = 2(L_{tank} + B_{tank}) = 1.2\ m$ tank perimeter

$L_{pipe} = 10\ m$ length of pipe from tank outlet to loop inlet

$D_{pipe} = 0.016\ m$ diameter of pipe

$Z_{pipe} = 10\ m$ height difference between pipe ends

$A_{s,tank} = B_{tank}L_{tank} + P_{tank}Z_{tank} + \pi D_{pipe}L_{pipe}$
$= 0.653\ m^2$ surface area of water

$\Delta t = 0.01\ s$ time step

$T_a = 13.1$ ℃ ambient air temperature

Step 2: Define Geometry: Refer also to figure 3-1

$N_1 = 10$ number of control volumes in pipe section 1 (leg 1)

$D_1 = 0.032\ m$ inside diameter

$L_1 = 8\ m$	length of pipe section
$N_{2a} = 1$	number of control volumes in pipe section 2a (section between elbow and first heating section)
$D_{2a} = 0.032\ m$	inside diameter
$L_{2a} = 0.225\ m$	length of pipe section
$N_{2ca} = 2$	number of control volumes in pipe section 2ca (first heating section)
$D_{2ca} = 0.032\ m$	inside diameter
$L_{2ca} = 1.9\ m$	length of pipe section
$N_{2cb} = 2$	number of control volumes in pipe section 2cb (second heating section)
$D_{2cb} = 0.032\ m$	inside diameter
$L_{2cb} = 1.9\ m$	length of pipe section
$N_{2cc} = 2$	number of control volumes in pipe section 2cc (third heating section)
$D_{2cc} = 0.032\ m$	inside diameter
$L_{2cc} = 1.9\ m$	length of pipe section
$N_{2cd} = 2$	number of control volumes in pipe section 2cd (fourth heating section)
$D_{2cd} = 0.032\ m$	inside diameter
$L_{2cd} = 0.55\ m$	length of pipe section
$N_{2b} = 1$	number of control volumes in pipe section 2b (section between fourth heating section and elbow)
$D_{2b} = 0.032\ m$	inside diameter
$L_{2b} = 0.225\ m$	length of pipe section
$N_3 = 10$	number of control volumes in pipe section 3 (leg 3)
$D_3 = 0.032\ m$	inside diameter
$L_3 = 8\ m$	length of pipe section
$N_{4a} = 1$	number of control volumes in pipe section 4a (section between elbow and first heat exchanger)
$D_{4a} = 0.032\ m$	inside diameter
$L_{4a} = 0.475\ m$	length of pipe section
$N_{4ca} = 2$	number of control volumes in pipe section 4ca (highest heat exchanger)
$D_{4ca} = 0.032\ m$	inside diameter
$L_{4ca} = 0.5\ m$	length of pipe section
$N_{4b} = 7$	number of control volumes in pipe section 4b (section between heat exchanger and elbow)
$D_{4b} = 0.032\ m$	inside diameter
$L_{4b} = 6.025\ m$	length of pipe section
$N_{5a} = 2$	number of control volumes in pipe section 5a (expansion tank pipe)
$D_{5a} = 0.016\ m$	inside diameter
$L_{5a} = 10\ m$	length of pipe section
$N_{5b} = 2$	number of control volumes in expansion tank
$D_{5b} = 0.3\ m$	width of control volume

$L_{5b} = 0.3\ m$ length of control volume
$N = 40$ total number of control volumes

Liquid only pressure loss coefficients at elbows
$P_{Lklo}(1) = P_{Lklo}(11) = P_{Lklo}(21) = P_{Lklo}(31) = 0.15$

$A_x = \frac{\pi D^2}{4}$ cross-sectional area of control volume
$V_x = L\ A_x$ volume of control volume
$A_z = \pi D\ L$ surface area of control volume
Table C-9 shows the length, diameter, cross sectional area, surface area and volume of each control volume.

Step 3: Apply initial conditions
$T_{tank} = 12.82\ °C$ initial expansion tank temperature
$P_1 = P_{atm} + \rho_{tank} g\ Z_{pipe}$ initial pressure in CV 1
$P_{atm} = 100700\ Pa$
$\rho_{tank} = (1.49343 \times 10^{-3} - 3.7164 \times 10^{-6} T_{tank} + 7.09782 \times 10^{-9} {T_{tank}}^2$
$-0.9032 \times 10^{-20} {T_{tank}}^6)^{-1} = 999.437\ kg/m^3$
$\therefore P_1 = 100700 + 999.437 * 9.81 \times 10 = 110694.4\ Pa$

Step 3.a: Initial temperature and mass fraction
Assume there is initially only liquid in the cells (i.e. x(k)=0) and all the control volumes are at temperature T(k)=12.82 °C

Step 3b: Initial density and mass
$\alpha = \frac{1}{1+\frac{1-x}{x}\frac{\rho_v}{\rho_l}}$ void fraction (initially zero)
$\rho = \alpha\rho_v + (1-\alpha)\rho_l$ mixture density
$\rho_v = \frac{P_B}{461(T+273.15)}$ vapour density
$\rho_l = (1.49343 \times 10^{-3} - 3.7164 \times 10^{-6} T_l + 7.09782 \times 10^{-9} {T_l}^2$
$-1.9032 \times 10^{-20} {T_l}^6)^{-1}$ liquid density

Because $\alpha = 0$ initially and it is assumed that the liquid inside the loop as at a constant temperature, the mixture density is exactly equal to the liquid phase density calculated earlier.
$M = \rho\ V_x$ control volume mass
The initial control volume masses, M, are given in table C-9.

Step 3c: Initial interface pressures
In leg 1, the pressure is constant and equal to P_1. In leg 2, the pressure can be calculated as follows:
$P(k) = P(k-1) - \rho_l g\ sin\theta(\pi)$
For example: The pressure in CV 10 is 110694.4 Pa. The Pressure in CV 11 is thus: $P(11) = P(10) - \rho_l g\ sin\theta(10) L(10)$
$\rho_l = (1.49343 \times 10^{-3} - 3.7164 \times 10^{-6} T_l + 7.09782 \times 10^{-9} {T_l}^2$

$-1.9032 \times 10^{-20} T_l^{\,6})^{-1} = 999.437\ kg/m^3$

$\therefore P(11) = 110694.4 - 999.437 \times 9.81 \times \sin(\pi) \times 0.8 = 110694.4\ Pa$

In leg 3, the pressure is constant and equal to $P(20)$. In leg 4, the pressure can be calculates using the same equation as in leg 2. See table C-9 for the initial cell interface pressures.

Table C-9: Initial conditions

CV no	L (in m)	θ (in rad)	D (in m)	A_x (in m^2)	V_x (in m^3)	A_z (in m^2)	P (in kPa)	P_B (in kPa)	$T_{sat,P}$ (in °C)	M (in kg)
1	0.8	3.142	0.032	0.0008	0.0006	0.080	110.69	109.91	102.39	0.64
2	0.8	3.142	0.032	0.0008	0.0006	0.080	110.69	110.69	102.60	0.64
3	0.8	3.142	0.032	0.0008	0.0006	0.080	110.69	110.69	102.60	0.64
4	0.8	3.142	0.032	0.0008	0.0006	0.080	110.69	110.69	102.60	0.64
5	0.8	3.142	0.032	0.0008	0.0006	0.080	110.69	110.69	102.60	0.64
6	0.8	3.142	0.032	0.0008	0.0006	0.080	110.69	110.69	102.60	0.64
7	0.8	3.142	0.032	0.0008	0.0006	0.080	110.69	110.69	102.60	0.64
8	0.8	3.142	0.032	0.0008	0.0006	0.080	110.69	110.69	102.60	0.64
9	0.8	3.142	0.032	0.0008	0.0006	0.080	110.69	110.69	102.60	0.64
10	0.8	3.142	0.032	0.0008	0.0006	0.080	110.69	110.69	102.60	0.64
11	0.225	1.571	0.032	0.0008	0.0002	0.023	110.69	110.69	102.60	0.18
12	0.95	1.571	0.032	0.0008	0.0008	0.096	110.47	110.58	102.57	0.76
13	0.95	1.571	0.032	0.0008	0.0008	0.096	109.52	109.99	102.41	0.76
14	0.95	1.571	0.032	0.0008	0.0008	0.096	108.57	109.05	102.17	0.76
15	0.95	1.571	0.032	0.0008	0.0008	0.096	107.62	108.10	101.91	0.76
16	0.95	1.571	0.032	0.0008	0.0008	0.096	106.67	107.15	101.66	0.76
17	0.95	1.571	0.032	0.0008	0.0008	0.096	105.72	106.20	101.41	0.76
18	0.95	1.571	0.032	0.0008	0.0008	0.096	104.77	105.25	101.15	0.76
19	0.95	1.571	0.032	0.0008	0.0008	0.096	103.82	104.30	100.89	0.76
20	0.225	1.571	0.032	0.0008	0.0002	0.023	102.87	103.35	100.63	0.18
21	0.8	0	0.032	0.0008	0.0006	0.080	102.87	102.87	100.50	0.64
22	0.8	0	0.032	0.0008	0.0006	0.080	102.87	102.87	100.50	0.64
23	0.8	0	0.032	0.0008	0.0006	0.080	102.87	102.87	100.50	0.64
24	0.8	0	0.032	0.0008	0.0006	0.080	102.87	102.87	100.50	0.64
25	0.8	0	0.032	0.0008	0.0006	0.080	102.87	102.87	100.50	0.64
26	0.8	0	0.032	0.0008	0.0006	0.080	102.87	102.87	100.50	0.64
27	0.8	0	0.032	0.0008	0.0006	0.080	102.87	102.87	100.50	0.64
28	0.8	0	0.032	0.0008	0.0006	0.080	102.87	102.87	100.50	0.64
29	0.8	0	0.032	0.0008	0.0006	0.080	102.87	102.87	100.50	0.64
30	0.8	0	0.032	0.0008	0.0006	0.080	102.87	102.87	100.50	0.64
31	0.475	-1.57	0.032	0.0008	0.0004	0.048	102.87	102.87	100.50	0.38
32	0.25	-1.57	0.032	0.0008	0.0004	0.050	103.35	103.11	100.56	0.40
33	0.25	-1.57	0.032	0.0008	0.0006	0.076	103.85	103.60	100.70	0.61
34	0.753	-1.57	0.032	0.0008	0.0006	0.076	104.60	104.22	100.87	0.61
35	0.753	-1.57	0.032	0.0008	0.0006	0.076	105.35	104.98	101.08	0.61
36	0.753	-1.57	0.032	0.0008	0.0006	0.076	106.12	105.73	101.28	0.61
37	0.753	-1.57	0.032	0.0008	0.0006	0.076	106.86	106.48	101.48	0.61
38	0.753	-1.57	0.032	0.0008	0.0006	0.076	107.61	107.24	101.68	0.61
39	0.753	-1.57	0.032	0.0008	0.0006	0.076	108.36	107.99	101.88	0.61
40	0.753	-1.57	0.032	0.0008	0.0006	0.076	109.12	108.74	102.08	0.61

Step 3d: Initial average pressure and saturation temperature

The average control volume pressure (i.e. central pressure) is calculated as follows:

$P_B = \frac{P(k)+P(k-1)}{2}$

The saturation temperature in each control volume is calculated using the following equation:

$$T_{sat,P} = \frac{\left(a_1+a_2\frac{P}{1000}+a_3\left(\frac{P}{1000}\right)^2+a_4\left(\frac{P}{1000}\right)^3+a_5\left(\frac{P}{1000}\right)^4+a_6\left(\frac{P}{1000}\right)^5\right)}{\left(1+a_7\frac{P}{1000}+a_8\left(\frac{P}{1000}\right)^2+a_9\left(\frac{P}{1000}\right)^3+a_{10}\left(\frac{P}{1000}\right)^4+a_{11}\left(\frac{P}{1000}\right)^5\right)}$$

Where: $a_1 = -14.40652$; $a_2 = 23.219627$; $a_3 = 3.0467342$;
$a_4 = 0.024755717$; $a_5 = -0.00014083304$; $a_6 = -0.00000023233413$;
$a_7 = 0.70908783$; $a_8 = 0.037347598$; $a_9 = 9.642729 \times 10^{-5}$;
$a_{10} = -0.0000012046366$; $a_{11} = -8.85599106 \times 10^{-10}$

The initial average pressures and saturation temperatures for each control volume are given in table C-9.

Step 3e: Initial cooling water temperatures and masses

$T_{cw} = 12.82℃$ initial cooling water temperature for both CVs

$M_{cw} = \rho_{cw}\, A_{x,c} L$ cooling water control volume mass

$$\rho_{cw} = \left(1.49343 \times 10^{-3} - 3.7164 \times 10^{-6} T_{cw} + 7.09782 \times 10^{-9} {T_{cw}}^2 - 1.9032 \times 10^{-20} {T_{cw}}^6\right)^{-1}$$

$$= 999.437\ kg/m^3$$

$$\therefore M_{cw} = 999.437 \times 0.001328 \times 0.5 = 0.66363\ kg$$

Step 3.f: Initial expansion tank mass

$$M_{tank} = \rho_{tank}\left(L_{tank} B_{tank} Z_{tank} + \frac{\pi {D_{pipe}}^2}{4} L_{pipe}\right)$$

$$= 999.437\left(0.3 \times 0.3 \times 0.05 + \frac{10\pi(0.016)^2}{4}\right) = 6.5070\ kg$$

Step 4: Calculate net heat transfer to control volume

Assume environmental losses are negligible and perfect conduction through the copper fins.

Table C-10: Heating section control volumes and corresponding heat input

CV	$\dot{S}(k)$ (in W)	$\dot{S}(k)$ (in W)	$\dot{S}(k)$ (in W)	$\dot{S}(k)$ (in W)
	t = 0	t = 3700	t = 7950	t = 12210
12 (HE1)	210.1	617.4	1001.8	1411.3
13 (HE1)	210.1	617.4	1001.8	1411.3
14 (HE2)	218.75	588.35	1001.8	1389.15
15 (HE2)	218.75	588.35	1001.8	1389.15
16 (HE3)	113.4	505.4	983.15	1456.1
17 (HE3)	113.4	505.4	983.15	1456.1
18 (HE4)	59.05	191.35	359.35	485.35
19 (HE4)	59.05	191.35	359.35	485.35

For the evaporator section the net heat flow to each cell is equal to the electrical power measured during experimentation divided by the number of control volumes in each section.

Table C-10 shows the heating section control volumes and their corresponding initial heat input.

The net cooling water heat transfer is calculated using:

$S_{cw} = h_c A_z (T_l - T_{cw})$

$h_c = \left(\frac{1}{h_{c,i}} + \frac{1}{h_{c,wall}} + \frac{1}{h_{c,o}}\right)^{-1}$ overall heat transfer coefficient

$h_{c,i} = \left((1-x)^{0.8} + \frac{3.8 \cdot x^{0.76} \cdot (1-x)^{0.04}}{P_r^{0.38}}\right) h_{lo}$ Shah's correlation

$h_{lo} = 0.023 \cdot \left(\frac{k_{lo}}{D}\right) \cdot Re_{lo}^{0.8} \cdot Pr_{lo}^{0.4}$ Dittus Boelter equation

$Re_{lo} = \frac{4\dot{m}}{\pi \mu_l D} = 0$ liquid only Reynolds number

$\mu_l = 2.414 \times 10^{-5} \times 10^{247.8/(273.15+T_l-140)}$ dynamic viscosity of liquid

$\therefore \mu_l = 2.414 \times 10^{-5} \times 10^{247.8/(273.15+12.82-140)} = 0.001208\ Ns/m^2$

$Pr_{lo} = \frac{c_{p,l}\,\mu_l}{k_l}$ liquid only Prandtl number

$k_l = 0.56673879 + 0.0019544929 T_l - 0.0000080770262 T_l^{\,2}$

$\therefore k_l = 0.56673879 + 0.0019544929(12.82) - 0.0000080770262(12.82)^2 = 0.5905$

$\therefore Pr_{lo} = \frac{4174 \times 0.001208}{0.5905} = 8.5389$

$\therefore h_{lo} = 0.023 \cdot \left(\frac{0.5905}{0.032}\right) \cdot 0 \cdot (8.5389)^{0.4} = 0 \qquad \therefore h_{c,i} = 0$

$h_{c,wall} = \frac{k_{wall}}{T_{wall}} = \frac{386}{0.0015} = 257333.33\ W/m^2K$

$h_{c,o} = \frac{Nu_{cw} k_{l,cw}}{D_{eq,cw}}$

$Nu_{cw} = \begin{cases} 4.861 & if\ Re_{cw} < 1181 \\ \frac{(f_{cw}/8) \cdot (Re_{cw} - 1000) \cdot Pr_{cw}}{1 + 12.7 \cdot (f_{cw}/8)^{0.5} \cdot (Pr_{cw}^{\,2/3} - 1)} & if\ Re_{cw} \geq 1181 \end{cases}$ Nusselt number

$f_{cw} = (0.79 \ln(Re_{cw}) - 1.64)^{-2}$ cooling water friction coefficient

$Re_{cw} = \frac{4\dot{m}_{cw}}{\pi \mu_{cw} D_{eq,cw}} = \frac{4 \times 0.1915}{\pi \times 0.001208 \times 0.019} = 10623.27 > 1181$ Reynolds number

$\therefore f_{cw} = (0.79 \ln(10623.27) - 1.64)^{-2} = 0.030953$

$Pr_{cw} = \frac{c_{p,cw}\,\mu_{cw}}{k_{cw}} = \frac{4174 \times 0.001208}{0.5903} = 8.5389$ cooling water Prandtl number

$$\therefore Nu_{cw} = \frac{(f_{cw}/8) \cdot (Re_{cw} - 1000) \cdot Pr_{cw}}{1 + 12.7 \cdot (f_{cw}/8)^{0.5} \cdot (Pr_{cw}^{\,2/3} - 1)}$$

$$= \frac{(0.030953/8) \cdot (10623.27 - 1000) \cdot 8.5389}{1 + 12.7 \cdot (0.030953/8)^{0.5} \cdot (8.5389^{2/3} - 1)}$$

$$= 90.57273$$

$\therefore h_{c,o} = \frac{Nu_{cw} k_{l,cw}}{D_{eq,cw}} = \frac{90.57273 \times 0.5903}{0.019} = 2813.952\ W/m^2\ K$

$\therefore h_c = \left(0 + \frac{1}{257333.33} + \frac{1}{2813.952}\right)^{-1} = 2783.514\ W/m^2\ K$

$\therefore S_{cw} = 2783.514 \times A_z(0) = 0$

MAIN LOOP

Step 5: Calculate net heat transfer

The net heat transfer calculation steps as detailed in step 4 are repeated inside the main loop.

Step 6: Calculate new temperature

The new control volume temperature is calculated from the finite difference integration scheme developed in section 3.2.1:

$$T_{new}(k) = T(k) + \frac{\Delta t \dot{S}(k)}{2m_m(k)C_{v,m}(k)} - \frac{\Delta t \dot{m}_m(k)}{2m_m(k)C_{v,m}(k)}(h_m(k-1) - h_m(k)) - \Delta t \frac{\Delta m_m}{\Delta t}\left(\frac{T_m(k)}{m_m(k)}\right)$$

All properties used in this equation refer to values determined at the previous time step.

$h_m = c_{p,l}T + x\, h_{fg}$ mixture enthalpy

In this case, because it is assumed that the temperature profile of the working fluid across any cross-section is constant 1-dimensional flow, the mixture enthalpy will also be consistent (Mills, 1998).

$\therefore h_m = 4174(12.82 + 273.15) + 0 = 1193639\, J/kg$

The new control volume temperatures are shown in table C-11.

Step 7: Calculate new void fraction

$$\alpha_{new} = \frac{1}{1+\frac{1-x_{new}}{x_{new}}\frac{\rho_v}{\rho_l}} = 0$$

Step 8: Calculate new mass fraction

If $T_{new} < T_{sat,P}$ then $u_{m,new} = C_{v,m}T_{new}$ mixture internal energy
and $x_{new} = 0$

If $T_{new} > T_{sat,P}$ then $T_{new} = T_{sat,P}$, $u_{m,new} = C_{v,m}T_{new}$ and $x_{new} = \frac{u_{m,new} - u_{f,new}}{u_{fg,new}}$

Step 9: Calculate new mixture density and mass

$\rho_{new} = \alpha_{new}\rho_v + (1 - \alpha_{new})\rho_l$

As the void fraction does not change, the mixture density remains the same.

$M_{new} = \rho_{new}\, V_x$

As the mixture density does not change, the mixture mass remains the same

Step 10: Calculate the two-phase multiplier

$\phi_L^2 = \left(1 + \frac{20}{X_{tt}} + \frac{1}{X_{tt}^2}\right)^{0.5}$ two-phase multiplier

$X_{tt} = \left(\frac{1-x}{x}\right)^{0.9}\left(\frac{\rho_v}{\rho_l}\right)^{0.5}\left(\frac{\mu_l}{\mu_v}\right)^{0.1}$ Martinelli parameter

$X_{tt} = 0 \qquad \therefore \phi_L^2 = 1$

Step 11: Calculate new cooling water temperatures

$$T_{cw,new}(k) = T_{cw}(k) + \frac{\Delta t(h_{cw,i}(k) - h_{cw,e}(k) + S_{cw}(k))}{M_{cw}c_{v,cw}}$$

$h_{cw,i} = \dot{m}_{cw}c_{p,cw}T_{cw}(k+1) = 0.1915 \times 4174 \times (12.82 + 273.15) = 228581.8\, J/kg$

$h_{cw,e} = \dot{m}_{cw}c_{p,cw}T_{cw}(k) = 0.1915 \times 4174 \times (12.82 + 273.15) = 228581.8\, J/kg$

$T_{cw,new}(k) = 12.82$ ℃

Step 12: Calculate new expansion tank temperature

$V_g = 0$ generated volume

For each control volume, the expanded/contracted volume must be calculated and the results added together to calculate the volume added to/subtracted from the expansion tank volume.

$V_{g,new}(k) = \alpha_{new}(k)V(k)$ $V_{g,total} = \sum V_{g,new}(k)$

In this instance, the new void fraction is zero in all control volumes, thus the volume remains constant. Heat is transferred between the tank and the surrounding air in the form of natural convection and radiation:

$S_{tank} = h_{tank}A_{s,tank}(T_{tank} - T_a)\Delta t + 0.05A_{s,tank} \times 5.669 \times 10^{-8}({T_{tank}}^4 - {T_a}^4)\Delta t$

$h_{tank} = 1.9|T_{tank} - T_a|^{1/3} = 1.9|12.82 - 13.1|^{1/3} = 1.243\ W/m^2K$

$\therefore S_{tank} = 1.243 \times 0.653(12.82 - 13.1) \times 0.01 + 0.05 \times 0.653 \times 5.669 \times 10^{-8}((12.82)^4 - (13.1)^4) \times 0.01$=-0.00227 W

$T_{tank,new} = T_{tank} - \frac{S_{tank}}{M_{tank}c_{v,l}} = 12.82 + \frac{0.00227}{6.507 \times 4174} = 12.8200$ ℃

If $V_{g,new} > V_g$ (i.e. volume has expanded) then

$\Delta M_{tank} = \rho_l(1)(V_{g,new} - V_g)$ change in expansion tank mass

$M_{tank,new} = M_{tank} + \Delta M_{tank}$ new expansion tank mass

$Z_{tank,new} = Z_{tank} + \frac{\Delta M_{tank}}{\rho_l P_{tank}}$ new water level in tank

If $V_{g,new} < V_g$ (i.e. volume has contracted) then

$\Delta M_{tank} = \rho_l(1)(V_g - V_{g,new})$ change in expansion tank mass

$M_{tank,new} = M_{tank} - \Delta M_{tank}$ new expansion tank mass

$Z_{tank,new} = Z_{tank} - \frac{\Delta M_{tank}}{\rho_l P_{tank}}$ new water level in tank

Step 13: Calculate new mixture velocity

$v_{m,new} = v_m + \Delta t\left(-\sum\left(\frac{f}{4} + k\right)\frac{\dot{m}^2 A_z}{2\bar{\rho}^2 {A_x}^3 L} - \sum g sin\theta\ - \frac{\bar{\rho}_{old} - \bar{\rho}_{older}}{\Delta t}\sum\frac{\dot{m}}{\bar{\rho}^2 A_x L}\right)$

If $Re_h = \frac{4|\dot{m}|}{\pi\mu D_{eq}} \leq 1$ then $f = 16$

If $Re_h > 1$ and $Re_h \leq 2300$ then $f = \frac{16}{Re_h}$

If $Re_h > 2300$ then $f = 0.079\ {Re_h}^{-0.25}$

In this case $Re_h = 0$ thus $f = 16$

In order to calculate the new mixture velocity, the terms $\left(\frac{f}{4} + k\right)\frac{\dot{m}^2 A_z}{2\bar{\rho}^2 {A_x}^3 L}$, $g sin\theta$ and $\frac{\dot{m}}{\bar{\rho}^2 A_x L}$ must be evaluated for each control volume and the results must be added.

$\therefore v_{m,new} = 0 + 0.01(-0 - 0\ - 0) = 0$

Step 14: Calculate new loop mass flow rate

$\dot{m}_{new} = \rho_{new} v_{m,new} A_x = 0$

Step 15: Calculate interface and average pressures

$P_{1,new} = P_{atm} + \rho_{tank,new} g Z_{pipe} = 110694.4\ Pa$

If $\dot{m} \geq 0$ (i.e. flow occurs in the positive direction) then

$P_i = P_{1,new}$

$dP_F = \frac{2L}{D} + \frac{P_{Lklo}}{2}$ frictional pressure drop

$dP_G = -\rho L g sin\theta$ gravitational pressure drop

$dP_M = \left(\frac{\dot{m}}{A_x}\right)^2 \left(\frac{1}{\rho_e} - \frac{1}{\rho_i}\right) + L\frac{\dot{m}_{new} - \dot{m}}{A_x \Delta t}$ momentum pressure drop

$\rho_e = \rho(k-1)$ $\rho_i = \rho(k)$

For this scenario, the mass flow rate is zero, thus the acceleration term falls away.

$dP = -dP_F - dP_G - dP_M$ total pressure gradient

$P_e = P_i - dP$ $P_i(k+1) = P_e(k)$ $P_B = \frac{P_i + P_e}{2}$ (see table C-11)

If $\dot{m} < 0$ (i.e. flow occurs in the negative direction) then

$P_e = P_{1,new}$

$\rho_e = \rho(k+1)$ $\rho_i = \rho(k)$

$dP = dP_F - dP_G + dP_M$ total pressure gradient

$P_i = P_e - dP$ $P_e(k+1) = P_i(k)$

Step 16: Calculate new saturation temperature

$$T_{sat,P} = \frac{\left(a_1 + a_2\frac{P}{1000} + a_3\left(\frac{P}{1000}\right)^2 + a_4\left(\frac{P}{1000}\right)^3 + a_5\left(\frac{P}{1000}\right)^4 + a_6\left(\frac{P}{1000}\right)^5\right)}{\left(1 + a_7\frac{P}{1000} + a_8\left(\frac{P}{1000}\right)^2 + a_9\left(\frac{P}{1000}\right)^3 + a_{10}\left(\frac{P}{1000}\right)^4 + a_{11}\left(\frac{P}{1000}\right)^5\right)}$$ (see table C-11)

Step 17: Replace old values with new values

Steps 5 to 17 are repeated until the desired time step is reached.

Table C-11: New conditions

CV no	$\dot{S}$ (in W)	T_{new} (in °C)	$u_{m,new}$ (in J/kg)	dP_F	dP_G	dP	P_e (in Pa)	P_i (in Pa)	P_B (in Pa)	T_{sat} (in °C)
1	0	12.82000000	53510.68	50	0	-50	110744	110694	110719	102.60
2	0	12.82000000	53510.68	50	0	-50	110794	110744	110769	102.62
3	0	12.82000000	53510.68	50	0	-50	110844	110794	110819	102.63
4	0	12.82000000	53510.68	50	0	-50	110894	110844	110869	102.64
5	0	12.82000000	53510.68	50	0	-50	110944	110894	110919	102.66
6	0	12.82000000	53510.68	50	0	-50	110994	110944	110969	102.67
7	0	12.82000000	53510.68	50	0	-50	111044	110994	111019	102.68
8	0	12.82000000	53510.68	50	0	-50	111094	111044	111069	102.70
9	0	12.82000000	53510.68	50	0	-50	111144	111094	111119	102.71
10	0	12.82000000	53510.68	50	0	-50	111194	111144	111169	102.72
11	0	12.82000000	53510.68	14.1	-2206.	2191.9	109003	111194	110098	102.44
12	210.1	12.82033115	53512.06	59.4	-9314.3	9254.9	99748	109003	104375	100.91
13	210.1	12.82033115	53512.06	59.4	-9314.3	9254.9	90493	99748	95120	98.29
14	218.8	12.82034479	53512.12	59.4	-9314.3	9254.9	81238	90493	85865	95.46
15	218.8	12.82034479	53512.12	59.4	-9314.3	9254.9	71983	81238	76610	92.37
16	113.4	12.82017874	53511.43	59.4	-9314.3	9254.9	62728	71983	67356	88.95
17	113.4	12.82017874	53511.43	59.4	-9314.3	9254.9	53473	62728	58101	85.13
18	59.05	12.82009307	53511.07	59.4	-9314.3	9254.9	44218	53473	48846	80.76
19	59.05	12.82009307	53511.07	59.4	-9314.3	9254.9	34964	44218	39591	75.63
20	0	12.82000000	53510.68	14.0	-2206.	2192	32772	34964	33868	71.92
21	0	12.82000000	53510.68	50.1	0	-50.08	32822	32772	32797	71.17
22	0	12.82000000	53510.68	50	0	-50	32872	32822	32847	71.21
23	0	12.82000000	53510.68	50	0	-50	32922	32872	32897	71.24
24	0	12.82000000	53510.68	50	0	-50	32972	32922	32947	71.28
25	0	12.82000000	53510.68	50	0	-50	33022	32972	32997	71.31
26	0	12.82000000	53510.68	50	0	-50	33072	33022	33047	71.35
27	0	12.82000000	53510.68	50	0	-50	33122	33072	33097	71.38
28	0	12.82000000	53510.68	50	0	-50	33172	33122	33147	71.42
29	0	12.82000000	53510.68	50	0	-50	33222	33172	33197	71.45
30	0	12.82000000	53510.68	50	0	-50	33272	33222	33247	71.49
31	0	12.82000000	53510.68	29.8	4657.1	-4686.9	37959	33272	35615	73.11
32	0	12.82000000	53510.68	31.3	4902.2	-4933.5	42892	37959	40425	76.13
33	0	12.82000000	53510.68	47.1	7384	-7431.1	50323	42892	46608	79.60
34	0	12.82000000	53510.68	47.1	7384	-7431.1	57754	50323	54039	83.29
35	0	12.82000000	53510.68	47.1	7384	-7431.1	65185	57754	61470	86.58
36	0	12.82000000	53510.68	47.1	7384	-7431.1	72616	65185	68901	89.55
37	0	12.82000000	53510.68	47.1	7384	-7431.1	80047	72616	76332	92.27
38	0	12.82000000	53510.68	47.1	7384	-7431.1	87478	80047	83763	94.78
39	0	12.82000000	53510.68	47.1	7384	-7431.1	94909	87478	91194	97.12
40	0	12.82000000	53510.68	47.1	7384	-7431.1	102341	94909	98625	99.31

APPENDIX D: DESIGN SPECIFICATIONS

The concept is divided into systems and subsystems to generate functional specifications.

System 1: Frame

The frame must hold the thermosyphon in position in the laboratory as well as allow operator to visually inspect and access all components. The available spatial envelope is 7.6 x 8.6 m . The frame must be designed in manageable sections not exceeding 2m in height/length for ease of assembly.

1.1 Ladder - A ladder must be incorporated into each upright section of the frame to allow access to all components. The ladder rung spacing cannot be greater than 70 cm.

1.2 Cage -A fall cage must surround the ladders in the frame to prevent operator falling.

1.3 Vertical support bracket - The loop must be supported by vertical support brackets. The brackets must be height adjustable to allow for compression of seals as well as variation in component length due to thermal expansion.

1.4 Horizontal support clamp - The loop must be supported by horizontal pipe retaining clamps. The clamps must not affect thermal distribution in the horizontal sections. Material must be able to withstand temperatures up to 150 °C.

1.5 Fasteners - The frame sections must be securely fastened to each other. The assembly must then be securely fastened to the floor and ceiling of the laboratory to limit component vibration.

System 2: Loop

The loop must be a scale model of the current RCCS design as proposed by Dobson (2006). The basic functional specifications of the loop are:

- Single closed loop thermosyphon
- 1/3 height scale model of RCCS (i.e. 7 m high)
- Must be less than 8.6 m wide
- Constant diameter circular profile piping
- Simulate heat source and sink
- Maintain evaporator working fluid inlet temperature below 65 °C
- Allow for single and single to two-phase operation
- One vertical leg must be slightly raised to provide a high point for air expulsion

Subsystem 2.1: Leg 1

The legs of the thermosyphon are numbered from 1-4 clockwise, starting with the bottom horizontal leg. Leg 1 must allow for the filling and draining of the loop as well as working fluid thermal expansion. Because the working fluid in this leg will be in the liquid phase at all times, mass flow rate measurement must occur in this leg.

2.1.1 Pipe - Material used for the pipe section must have a high thermal conductivity and well known heat transfer characteristics. Pipe ends must be welded to flanges to allow for assembly.
2.1.2 Orifice Plate - Mass flow rate must be measured by an orifice plate as it allows for bidirectional flow measurement. The orifice plate must adhere to BS 1042: Section 1.1:1981 standards.
2.1.3 Pressure tappings - Pressure trappings must adhere to BS 1042: Section 1.1:1981 standards.
2.1.4 Drain valve - The drain valve must allow for filling and draining of the loop. The valve must include a pipe fitting to allow it to be attached to the outlet pipe of the expansion tank.
2.1.5 Sight glass - A large sight glass (100 mm in length) must be included near the condenser section outlet to allow the operator to visually ensure that working fluid is in the liquid phase at all times. The material must be transparent and capable of withstanding temperatures up to 140 °C
2.1.6 Flanges - All flanges must adhere to ISO 7005-3:1988 standards. Flanges must be welded to pipe sections.
2.1.7 Seals - Silicon seals no thinner than 2 mm must be used to seal flanges. System must be completely water tight.
2.1.8 Fasteners - Flanges must be securely fastened to ensure no leaks occur

Subsystem 2.2: Leg 2
Leg 2 must allow for heat to be added to the system. To allow for ease of assembly, this leg must be manufactured in separate sections not exceeding 2 m in length.
Subsystem 2.2.1: Evaporator section
The evaporator section must be capable of adding 10 kW of heat to the working fluid. Each heating section must consist of a finned pipe and two heating elements which are thermally insulated and covered to protect wiring from possible water damage.
2.2.1.1 Finned pipe - The pipe fins must be wide enough to accommodate heating elements bolted to the fin. The fin material must have a high thermal conductivity to allow the maximum heat to be transferred to the working fluid. Fin thickness cannot be less than 10 mm to allow for holes to be drilled to insert thermocouples for temperature distribution measurement. Fins must allow a 20 mm gap on each side of the pipe length to allow for fastener access.
2.2.1.2 Heating elements - Two flat heating elements must be attached to each finned pipe. The elements must have an evenly distributed flux to accurately represent the RCCS heat source. Heating elements must have a thermal cut off to prevent burn out. It must be possible to vary the heat input as well as control which heating sections are active. Heating elements must be securely fastened to the finned pipes ensuring a large contact area for thermal conduction.
2.2.1.3 Cladding material - The cladding material must be able to thermally insolate the heating elements at operating temperatures up to 300 °C.
2.2.1.4 Covers - The heating section assemblies must be covered by a well fitting cover to prevent possible water damage.

2.2.2 Sight glass - The sight glass in this leg must allow for visual identification of when boiling occurs. The sight glass must thus be positioned at the end of the evaporator section. The material must be transparent and capable of withstanding temperatures up to 140 °C
2.2.3 Flanges - All flanges must adhere to ISO 7005-3:1988 standards. Flanges must be welded to pipe sections.
2.2.4 Seals - Silicon seals no thinner than 2 mm must be used to seal flanges. System must be completely water tight.
2.2.5 Fasteners - Flanges must be securely fastened to ensure no leaks occur
2.2.6 Pipe - Material used for the pipe section must have a high thermal conductivity and well known heat transfer characteristics. Pipe ends must be welded to flanges to allow for assembly. The pipe diameter must be large enough to prevent dry out but small enough to allow blasting to occur to ensure full development of two-phase flow.

Subsystem 2.3: Leg 3
Leg 3 must incorporate an air release valve and a sight glass.
2.3.1 Air release valve - The valve must be placed at the highest point of the loop to allow all air to be manually purged from the system. The valve must be water and air tight.
2.3.2 Sight glass - The sight glass must allow for visual identification of horizontal 2-phase flow regimes. The material must be transparent and capable of withstanding temperatures up to 140 °C
2.3.4 Pipe - Material used for the pipe section must have a high thermal conductivity and well known heat transfer characteristics. Pipe ends must be welded to flanges to allow for assembly. The pipe length must be long enough to ensure fully separated flow enters the condenser section (i.e. > 3 m).
2.3.5 Flanges - All flanges must adhere to ISO 7005-3:1988 standards. Flanges must be welded to pipe sections.
2.3.6 Seals - Silicon seals no thinner than 2 mm must be used to seal flanges. System must be completely water tight.
2.3.7 Fasteners - Flanges must be securely fastened to ensure no leaks occur

Subsystem 2.4: Leg 4
Leg 4 must allow for heat to be removed from the system. To allow for ease of assembly, this leg must be manufactured in separate sections not exceeding 2 m in length.

Subsystem 2.4.1: Condenser section
The condenser section must be capable of removing 10 kW of heat from the system. The heat exchangers must be pipe-within-pipe heat exchangers due to spatial constraints.
2.4.1.1 Inside pipe - Material used for the pipe section must have a high thermal conductivity and well known heat transfer characteristics. Pipe ends must be welded to flanges to allow for assembly.

2.4.1.2 Outside pipe - The outer pipe must be transparent to allow for visual identification of voids. The inlet pipe must be angled so that the cooling water is forced to spiral around the inside pipe. The space between the inlet/outlet and rim of the outer pipe cannot be less than 20 mm to allow for the connecting bush. The outer pipe must be easily removable for cleaning and repair whilst forming a water tight seal with the inside pipe. The inlet/outlet pipes must have a diameter consistent with available transparent pvc tubing. The diameter of the outside pipe is determined as follows:

$$\dot{Q}_{cw} = \dot{m}_{cw} c_{p,cw} \Delta T \quad \text{(E-1)}$$

$c_{p,cw}$ is taken as 418 kJ/kg K and ΔT_{min} = 1.5 K. The maximum length of a heat exchanger is 2 m thus the minimum heat removal capacity required of one section is approximately 3000 W.

$$\therefore \dot{m}_{cw} = \frac{\dot{Q}_{cw}}{c_{p,cw}\Delta T} = \frac{3000}{4180(1.5)} = 0.478\ kg/s$$

From the definition of the Reynolds number (Incropera and De Witt, 2002):

$$Re_D = \frac{4\dot{m}_{cw}}{\pi D_h \mu_{cw}} \quad \text{(E-2)}$$

μ_{cw} is taken as 725 x 10^{-6} Ns/m^2. For optimal heat transfer, the cooling water flow must be turbulent, i.e. Re > 2000. The hydraulic diameter can now be determined.

$$D_h = \frac{4\dot{m}_{cw}}{Re_D \pi \mu_{cw}} < \frac{4(0.478)}{2000\pi(725x10^{-10})} < 0.420\ m$$

This very large diameter results in outside pipe diameter selection being solely dependent on standard material pipe size, availability and related costs.

2.4.1.3 Connecting bush - The connecting bush must securely, but not permanently, connect the inner and outer pipes. The seal formed between the two pipes must be completely water tight. The material must be such that the thermal expansion will not break the seal between the two pipes. The connecting bush must allow for movement along the length of the inside pipe for ease of assembly, cleaning and repairing. O-ring grooves in the connecting bush must allow for the use of industry standard (off the shelf) o-rings.

2.4.1.4 O-rings - O-rings used in the connecting bush must adhere to industry standards.

2.4.1.5 Transparent Piping - Transparent piping must be used to connect the outlet of each condenser section to the drain. This is to visually ensure no bubbles are formed at the thermocouple holes and to verify cooling water flow. Each pipe must have a hole punctured as close as possible to the heat exchanger outlet for temperature measurement. A ball valve must be positioned at the end of each pipe section to control cooling water flow rate and allow for flow rate measurement.

2.4.1.6 Constant header tank - A constant header tank is required to ensure that cooling water is fed at a constant pressure. One is available for use in the heat transfer laboratory. The constant header tank must be position higher than the inlet of the top most heat exchanger and close to the water source. The tank must be connected with durable pvc piping to the inlets of the heat exchangers.

2.4.1.7 PVC piping - The piping connecting the constant header tank to the heat exchangers must be of large enough diameter to ensure constant cooling water

flow. The pipe is exposed to the elements as it is fed from the sunroof to the laboratory and must thus be durable.
2.4.1.8 Pipe clamps - Pipe clamps must be used to connect the pvc piping to the heat exchangers as well as to any reducers, expanders and tap fittings used to prevent high pressure slippage.
2.4.2 Sight glass - The sight glass in this leg must allow for visual identification of vertical two-phase flow regimes. The sight glass must thus be positioned before the condenser section. The material must be transparent and capable of withstanding temperatures up to 140 °C
2.4.3 Flanges - All flanges must adhere to ISO 7005-3:1988 standards. Flanges must be welded to pipe sections.
2.4.4 Seals - Silicon seals no thinner than 2 mm must be used to seal flanges. System must be completely water tight.
2.4.5 Fasteners - Flanges must be securely fastened to ensure no leaks occur
2.2.6 Pipe - Material used for the pipe section must have a high thermal conductivity and well known heat transfer characteristics. Pipe ends must be welded to flanges to allow for assembly.
2.3 Elbows - 90° elbows must be used to connect the four legs of the loop to limit frictional losses in the corners. Each elbow must have a thermocouple fitting attached to allow working fluid temperature measurement at each leg inlet and outlet. Flanges must be welded to the elbows for ease of assembly.
2.4 Expansion tank - The expansion tank must allow for a volume increase of at least 100 %. This will also allow the loop to be filled by means of the expansion tank. The tank must be open to atmospheric pressure and be positioned sufficiently high above the loop inlet to prevent backwash. The tank must have a lid to prevent rain/detritus from entering the loop. A water measure must be incorporated to allow the operator to measure how much water is in the loop. The expansion tank must be connected to the inlet of the loop by means of durable pvc piping.

System 3: Data logging System
The data logging system must be capable of logging all temperatures and pressures during operation at a sampling rate dictated by the operator. The system must be positioned near the loop to minimize the length (and thus electronic noise) of the required wires.
3.1 Computer - The computer must have a usb port to allow for connection to the data logging unit and an operating system of Windows 2007 or newer to run the data logging software.
3.2 Data logging unit - The data logging unit must be able to monitor multiple signals (temperature, current, voltage) over extended periods of time.
3.3 Thermocouples - Thermocouples must be selected for cost as well as sensitivity. The system operates at temperatures up to 150 °C. Thermocouples used to measure working and cooling fluid temperatures must be electrically insulated and sheathed.

3.4 Pressure transducer - A differential pressure transducer is required to measure the pressure difference across the orifice plate. A suitable transducer is available in the heat transfer laboratory.

System 4: Control Box

The control box must connect the 3-phase power supply to the heating elements. It must have individual power switches for each heating section. The control box must allow for variation of power to the individual heating sections. A display of the power/current of each section must be included. The control box must be water proof. The control system must incorporate an alarm that sounds when maximum heating element operating temperature has been exceeded as well as notify the user of element failure. The control box must be position in such a way that it is easily accessible to the operator.

Due to the limited space allocated to Masters' theses, only the bill of materials for the closed loop thermosyphon (system 2) is given in table E-1.

Table D-1: Bill of materials for closed loop thermosyphon

Assembly No	Spec No	Part No	Item		Description	Quantity per assembly	Total
1	2.3		Bend			4	4
		1.10		90° elbow	ID 35 mm	1	4
		1.20		Flange		2	8
		1.30		Copper pipe	OD 35 mm x 100 mm	200 mm	800 mm
2	2.4.1		640 mm pipe-in-pipe heat exchanger			1	1
	2.4.1.2	2.10		glass pipe		1	1
	2.4.1.3	2.20		heat exchanger connector		2	2
	2.4.1.1	2.30		Copper pipe	OD 35 mm x 650 mm	650 mm	650 mm
	2.3.5	1.20		Flange		2	2
3	2.4.1		2000 mm pipe-in-pipe heat exchanger			3	3
	2.4.1.1	3.10		Copper pipe	OD 35 mm x 2000 mm	2000 mm	6000 mm
	2.3.5	1.20		Flange		2	6
	2.4.1.2	3.30		glass pipe 3		1	3
	2.4.1.3	2.20		heat exchanger connector		2	6
4	2.3		Upper pipe			1	1
	2.3.4	4.10		Copper pipe	OD 35 mm x 7650 mm	7650 mm	7650 mm
	2.3.5	1.20		Flange		2	2

5	2.2		2000 mm heater			3	3
	2.2.6	5.10		Copper pipe	OD 35 mm x 2000 mm	2000 mm	6000 mm
	2.2.1.1	5.20		Fin	10 mm x 50 mm x 1900 mm	2	6
	2.2.3	1.20		Flange		2	6
6	2.2		650 mm heater			1	1
	2.2.6	6.10		Copper pipe	OD 35 mm x 650 mm	650 mm	650 mm
	2.2.1.1	6.20		Fin	10 mm x 50 mm x 550 mm	2	2
	2.2.3	1.20		Flange		2	2
7	2.1.5, 2.2.2, 2.3.2		Sight glass			3	3
8	2.1		Bottom left pipe			1	1
	2.1.1	8.10		Copper pipe	OD 35 mm x 4000 mm	4000 mm	4000 mm
	2.1.6	1.20		Flange		2	2
9	2.1.2, 2.1.3		Orifice Plate			1	1
	2.1.2	9.10		Orifice Plate		1	1
	2.1.6	1.20		Flange		2	2
10	2.1		Bottom right pipe			1	1
	2.1.1	10.10		Copper pipe	OD 35 mm x 3363.96 mm	3363.96 mm	3363.96 mm
	2.1.6	1.20		Flange		2	2
11	2.4.2		Sight glass bottom			1	1

APPENDIX E: EXPERIMENTAL PROCEDURE

Normal Operating Conditions

To ensure each experiment is executed in a safe manner, the procedures laid out below must be followed.

Start-up procedure:

- Wear safety shoes
- Switch off main power supply, power switch at the electrical box, all element switches and set all power variation dials to zero
- Mop up any water on the laboratory floor
- Close electrical ducting to prevent possible water damage
- Close and lock the electrical box with the key provided
- Open expansion tank valve (bottom right hand corner of loop)
- Make sure the natural circulation loop is filled with water. Air bubbles in the system can be removed through the air relief valve located on the upper left hand elbow
- Close all heat exchanger outlet valves and visually verify no large air pockets or blockages exist in the glass sections or plastic piping. Place outlet pipes properly in the drain to prevent water spillage
- Push data cards fully into data logger slots and plug in the power cable
- Switch on power at wall plug. This will switch on power to computer, Agilent Data Acquisition Unit and pressure transducers.
- Switch on data logger by pressing the power button on the front screen (if unit is not already on)
- Open Benchlink Data Logger 3 program on the computer and run Test configuration. This automatically configures channels to be measured and data can be logged by pressing the play button under the scan and log data tab. Run brief scan to ensure all channels are reading (a zero reading indicates improper connection to data card)
- Visually inspect copper pipes and seals for leaks
- Clear away any loose equipment or tools lying on the walkway
- On the sunroof, connect the feedwater supply to the constant header tank and open the feedwater tap. Wait until a constant head is attained (i.e. when water starts flowing out the overflow pipe) before opening heat exchanger outlet valves. Note level in the expansion tank.
- Open outlet valves of desired heat exchangers
- Measure coolant water flow rate for each individual section using a stopwatch and scale and adjust valve until desired flow rate is attained (note that flow rates of all sections should preferably be equal)
- Switch on main supply to DB-LAB
- Start logging data
- Turn on switch Q1 on the electrical box (this switches on the electrical box)

- Turn power switch for desired element pairs (1 to 4) from zero to one, note that the ammeters for corresponding element pairs 1 to 4 should now be on and read zero.
- Adjust desired power output level (0 to 100%), note that green light for each element should be on and ammeter measurement should increase corresponding to increased power output level (maximum 13 A)
- Wait until steady state is attained

Shut down procedure:

- Stop scan/log data
- Adjust power output level of each element pair to zero
- Turn power switch for element pairs from one to zero
- Turn off switch Q1 on electrical box
- Turn off main power supply to DB-LAB
- Wait until boiling ceases then close heat exchanger outlet valves
- Close feedwater supply tap on sunroof
- Switch off all wall sockets

Malfunction Conditions

Fault	Indicators	Possible causes	Result	Corrective Actions
Loss of coolant	• Large air bubble or no fluid in glass pipes • Steep rise in working fluid temperature	• Loss of feedwater • Cracked or broken glass pipe • Worn or perished O-rings • Pipe clamp leakage • Perished/damaged/ blocked feed pipes	• Water seepage into lab could damage equipment and increase the risk of electrical shock or electrical short circuitry • Increased working fluid temperature leading to excessive boiling and large vapour plugs forming which could result in burnout of the heating elements	• Switch off main power supply to DB LAB • Stop scanning • Switch off all wall sockets • Turn off feedwater supply tap on sunroof • Mop up excess water in the laboratory • Check extent of water damage to electrical equipment • Identify cause of loss of coolant and repair
Temperature measurement malfunction:.	• Zero reading on data logging software • Unexpected or unrealistic results in data processing	• Damaged/bent thermocouple wires • Loose/improper connection to data logger • Loose/improper connection to heat source • Data logger/card malfunction	• Inaccurate experimental results	• As this condition is generally only identified during the data processing stage, the cause of thermocouple malfunction must be identified and repaired prior to the next test.
Element malfunction:	• Zero or erratic reading on ammeter • Sudden drop in measured fin temperature	• Water damage to electrical wiring • Overheating of wiring • Loose wiring • Power failure	• Inaccurate experimental results	• Switch off main power supply to DB LAB • Stop scanning • Close heat exchanger outlet valves • Turn off feedwater supply tap on sunroof • Identify cause of element malfunction and repair